UNIVERSITY OF OKLAHOMA

GRADUATE COLLEGE

AN EXPERIMENTAL INVESTIGATION ON CREEP BEHAVIOR OF SHALE

ROCKS: WITH EMPHASIS ON THE INFLUENCE OF TEMPERATURE AND

ANISOTROPY

A THESIS

SUBMITTED TO THE GRADUATE FACULTY

in partial fulfillment of the requirements for the

Degree of

MASTER OF SCIENCE

By

ELAHE KHOSRAVI
Norman, Oklahoma
2017

AN EXPERIMENTAL INVESTIGATION ON CREEP BEHAVIOR OF SHALE
ROCKS: WITH EMPHASIS ON THE INFLUENCE OF TEMPERATURE AND
ANISOTROPY

A THESIS APPROVED FOR THE
MEWBOURNE SCHOOL OF PETROLEUM AND GEOLOGICAL ENGINEERING

BY

_____
Dr. Ahmad Ghassemi, Chair

_____
Dr. Mashhad Fahs

_____
Dr. Xingru Wu

to

My beloved husband, Hessam

Acknowledgments

I would like to thank and commend everyone who has contributed to this thesis. I wish to express my appreciation to them.

To my advisor, Professor Ahmad Ghassemi, for your confidence in me and giving me the opportunity to work with you, for your unwavering support all throughout my Master's study, and for your guidance and motivation that greatly inspired me to do my best.

To my committee members, Dr. Wu and Dr. Fahs, for your willingness to serve and for your insightful and articulate comments.

To Mr. Stephen Dwyer for sharing your immense technical skills and all the assistance you gave for my tests.

To my colleagues, especially Dr. Yawei Li and Rohit Bakshi, for their assistance and insight in doing my experiments.

To my friends Ali Parvizinia, Ankita Sinha, Jiwon Jeon, Mohammad Hadikhan Tehrani, Atefe Hejri, Sattar Atash Bahar, Shadi Salahshoor, Nooshin Nassr and Saeid Hosseinipoor. Thank you for making the OU years fun ones.

To our caring host family, Kevin and Becca Bradford and their children, for your support and help. I feel very lucky to be associated with you.

My sincerest and deepest gratitude to my family for your unfaltering love and support all throughout the different stages I have gone through in my life. I want you to know that the distance and time you have endured is worth every drop of sweat and blood I poured

Table of Contents

List of Tables

xi

List of Figures

xiii

xvi

Abstract

Deformation of materials under constant load over time is known as creep. The conductivity of fractures produced by hydraulic fracturing decreases over time as a result of this time-dependent phenomenon that requires to be studied thoroughly to predict the production loss.

Creep deformation happens under different environmental conditions including confining pressure, temperature, and anisotropy, among others. In order to accurately predict the creep deformation of formation rocks, the creep test requires to be conducted under similar condition as reservoir.

In this thesis the creep behavior of five different shale rocks have been studied: Eagle Ford, Mancos, Barnett, Pierre and Haynesville shale. Most of tests were conducted under ambient temperature and high temperature. To study the influence of anisotropy the creep tests were performed on two samples of Mancos, Barnett, Pierre and Haynesville shale perpendicular and parallel to the bedding.

The result indicated the temperature and anisotropy have a significant influence on the creep behavior of shale rocks. Increasing the temperature resulted in higher strain rate. It was observed that the parallel samples experienced lower instantaneous and creep deformation compared to the samples cored parallel to the bedding.

Chapter 1: Introduction

1.1.Unconventional shale reservoir

Energy demand is expected to increasingly continue in the coming years as the result of population growth and economic development. In recent decades, unconventional reservoirs have been considered as a reliable source of energy to help meet this demand. As the name implies, the production from these reservoirs is not feasible through conventional methods, and it is essential to use stimulation and advanced recovery technologies to produce from these reservoirs. Shale and tight reservoirs are two types of unconventional reservoirs, which are characterized by high porosity and low permeability in the nano-Darcy scale. The importance of shale and tight reservoirs contribution in oil and gas production is significantly noticeable in North America (Figure 1). According to Figure 2, the production from shale gas reservoirs has been increased dramatically to more than 25 billion cubic feet per day from 2000 to 2013, corroborating the growing rise in exploitation from these reservoirs (Geologists and Division, 2015). Shale reservoirs are expected to roughly provide 50% of domestic energy by 2040, especially in North America. Production from these reservoirs can be implemented by means of a stimulation method called hydraulic fracturing. It involves inducing fractures in rock through injecting a high-pressure fluid (usually water) into a wellbore that will in turn create sufficient paths for fluids to permeate the rock toward the wellbore. Fractures propagate when the induced pressure exceeds the fracture pressure and perpendicularly to the direction of the minimum principal stress. This type of fracture is called "planner tensile fracture."

Figure 1. Shale and tight oil locations in North America (From EIA, 2011)
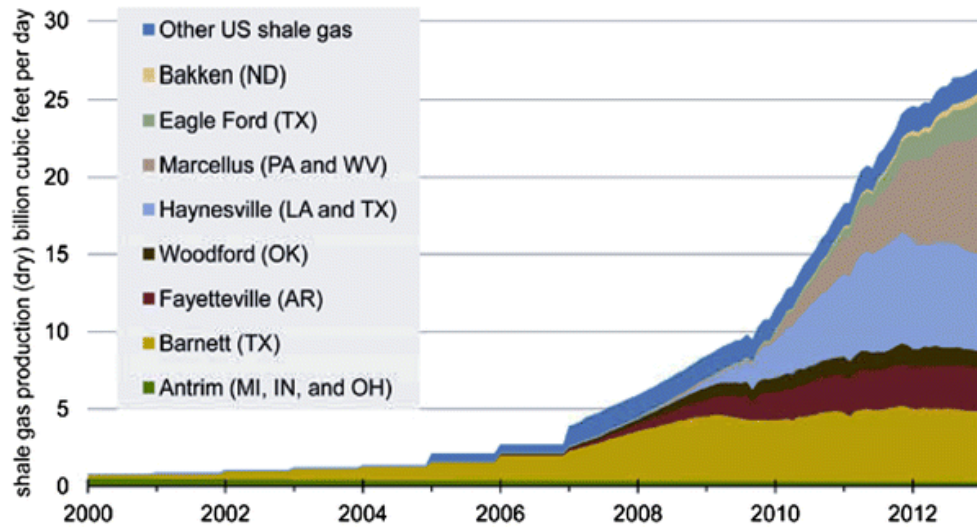
Figure 2. The production of all the shale reservoirs in North America from 2000 to 2013 (From EIA, 2014)

Besides these large fractures, hydraulic fracturing can result in numerous small shear fractures in the formation rock. After the fractures are generated, some particles are injected to them so as to maintain them open. The particles material is specific to the lithology of the formation rock. Proppant sands or artificial engineered particles such as ceramic proppant are used for shale reservoirs (Hoeksema, 2013).

1.2. Influence of creep deformation on hydraulic fracturing

Hydraulic fracturing is a complicated process, although not geomechanically well understood, that has increasingly been used in the recent decades. Hydraulic fracturing is remarkably popular for production from conventional reservoirs, but for unconventional reservoirs a variety of issues are expected to arise, including fracture surface area and conductivity reduction, among others (Li and Ghassemi, 2012). Conductivity reduction could occur due to various mechanisms such as fracture closure and proppant embedment (Alramahi and Sundberg, 2012 and Guo and Liu, 2012). Over time, these issues result in a production loss and a reduction in oil/gas recovery. Fracture closure and proppant embedment could occur under a constant closure stress. This visco-plastic phenomenon, which will be thoroughly discussed in the next section, is referred to as creep deformation and has an adverse influence on production and therefore requires to be thoroughly studied. However, these issues are initiated immediately upon production commencement where the rock undergoes elastic deformations due to an increase in the effective horizontal stress caused by the pore fluid pressure dissipation. Addressing this deformation-induced production loss requires studying all the elastic, viscos, and plastic deformations of the shale rock. In addition, it has been shown that the hydraulic fracture

conductivity losses escalate rapidly under high temperatures as well as in exposure to the fluid used to fracture the formation rock (Li and Ghassemi, 2012).

1.3. Creep deformation

Creep is the increasing deformation of rock under a constant load and comprises three stages as (Figure 3):

Transient or primary creep

Steady state or secondary creep

Accelerating or tertiary creep

The main characteristic of the first stage of creep deformation is that the strain rate decrease by time. During this stage, the rock experiences visco-elastic deformations that can be fully recovered upon unloading the rock. After unloading, the instantaneous elastic deformation of rock is first recovered followed the gradual recovery of viscous deformations. The same mechanism is responsible for stress relaxation, which is the observed reduction in stress generated in response to a sustained strain.

Unlike the first stage, the second stage of creep deformation involves a constant strain rate. The rock exhibits visco-elasto-plastic behavior in this stage. As shown in Figure 3, the rock cannot recover all the deformation after unloading and experiences a permanent deformation due to plastic strains. However, similar to the first stage, the elastic instantaneous and elastic viscos deformations of the rock in the second stage are removed upon unloading (Bell, 2013).

The third stage is distinguished from the first and second stages by its increasing strain rate that eventually leads to mechanical failure of the rock. The time required to

4

reach this stage depends on the stress state applied to the rock. It is assumed that the induced unstable fractures are responsible for the rock failure at the end of this stage (Fjar et al., 2008).
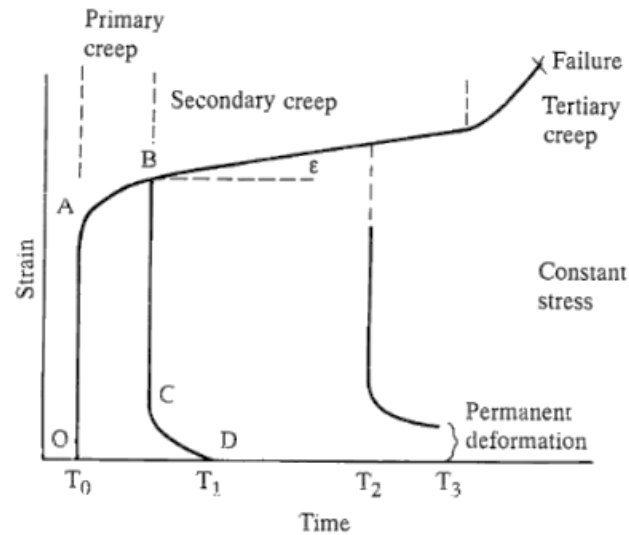
Figure 3. General creep behavior, stress vs. time (Bell, 2013)

1.4. Objectives

The goal of this thesis is to study the time-dependent behavior of some shale rocks under different conditions. The emphasis of this study is on the influence of temperature and anisotropy. The main objectives of this study are as follows:

- Development of a generalized procedure for all the shale rocks
- Conducting a two-stage hydrostatic creep test under the confining pressure close to in-situ confining pressure
- Conducting 2-3 stages of deviatoric creep test under room temperature
- Conducting 2-3 stages of deviatoric creep test under elevated temperature

- Performing all of the above stages on two samples of each rock, one cored parallel to the bedding and another cored perpendicular to the bedding

Chapter 2: Literature review

This chapter reviews the state of the art or state of the practice related to the creep of shale rock formations. This survey is not intended to be comprehensive, and only the most salient studies are summarized, evaluated, and compared.

2.1. Viscoelastic behavior of rocks

The general behavior of rocks is viscoelastic. It means that rocks show the elastic deformation initially upon loading followed by viscos deformation. The viscous deformation of rock is related to the fact that strain rate of rocks is corresponding to the stress subjected to the rock body (Figure 4).
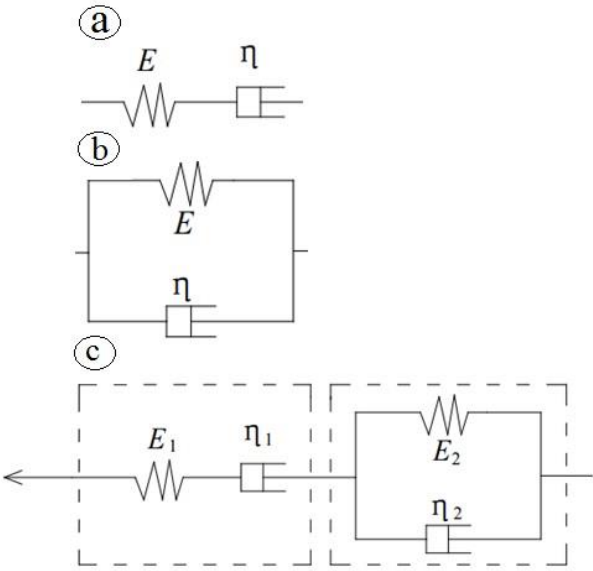
Figure 4. Maxwell model b) Kelvin model, e) Burger's model

The elastic and viscos response of the rock body is represented by a spring and dashpot, respectively (Jaeger et al., 2007). Different viscoelastic models have been

proposed as shown in Figure 4. Each of presented models has different response: Maxwell model represents a liquid which flows at a constant rate upon a sudden shear load applied and held constant; the strain by this model can be obtained by:

<div align="right">**Equation 1**</div>

$$\varepsilon = \frac{\sigma}{E} + \frac{\sigma}{\eta}\,t$$

where, ε is strain, σ is the applied stress, E is the linear spring constant or Young's modulus and η is the viscosity coefficient. The shear strain rate of a solid material, which is represented by Kelvin model, decreases with exponential trend; this model defines the strain by the following equation:

<div align="right">**Equation 2**</div>

$$\varepsilon = \frac{\sigma}{E}(1 - e^{-\frac{Et}{\eta}})$$

Model c is Maxwell and Kelvin model in series, representing a material which exhibits an instantaneous strain that becomes asymptotic to a line (Goodman, 1989).

<div align="right">**Equation 3**</div>

$$\varepsilon = \frac{\sigma}{E_1} + \frac{\sigma}{\eta_1}\,t + \frac{\sigma}{E_2}(1 - e^{-\frac{E_2 t}{\eta_2}})$$

The first two terms on the right side of above equation refer to elastic and viscos deformation while the third one is related to the retarded elasticity of Kelvin model.

2.2. Creep mechanisms

Generally, different mechanisms can govern the creep behaviors of rocks which will be discussed briefly in this section. These mechanisms include dislocation, diffusion, grain boundary sliding and cataclasis.

Dislocation mechanism is the result of distortion of lattice or net which in turn generates force applied to bonds that could propagate the dislocation imperfections through climbing, cross-slipping and gliding when exceeds the bond strength. This mechanism could carry on and results in new packing or grain boundary.

Diffusion mechanism occurs as a result of atoms or vacancies movement inside of a grain or on the grain boundaries. The direction of vacancies migration is opposite to the direction of creep strain. The linear creep deformation is dominate if only the governing creep mechanism is diffusion.

The shear stress between particles (grains) leads to the grain boundary sliding mechanism. Normally, dislocation or diffusion mechanism in one grain is followed by grain boundary sliding mechanism, which deforms the shape of adjacent grains. This mechanism is important in high porosity rocks.

Cataclasis is another form of mechanism that could occur when the applied force exceed the frictional strength, grain or pore structure strength. This brittle mechanism takes place at the grain boundary. To study the creep behavior of shale rocks and assure about the governing creep law, it is essential to study the creep mechanism of this type of rocks (Weijermars, 1997).

The above mentioned includes all creep mechanisms could occur in all types of rocks. However, dislocation and diffusion are more probable in rock salts. As all the deviatoric creep tests were conducted under low deviatoric stress (less than half of peak stress) the cataclasis mechanism could not be the dominant mechanism. Under low stress and low temperature as the case of all the tests of this study, grain boundary sliding is more probable compared to other mechanisms. Grain boundary sliding is facilitated by

higher confining pressure. The creep mechanism of shale rocks used in this study will be discussed in chapter 5.

2.3. Linear creep

Linear creep is occurred when the strain rate is proportional to the applied stress similar to the Newtonian viscous fluid. Dynamic viscosity is the ratio of shear stress and strain rate. The viscosity of material varies with temperature this is the reason why increasing the temperature has a great influence in increasing strain rate. The influence of temperature in reduction of viscosity for Newtonian viscos material can be correlated by Arrhenius relationship (Weijermars, 1997):

Equation 4

$$\eta = A \exp(\frac{B}{T})$$

where A and B are constant and T is absolute temperature. The linear creep occurs in the case of diffusion creep mechanism (Weijermars, 1997).

2.4. Nonlinear Creep

It occurs when the applied stress and strain rate can be correlated by power low as follows:

Equation 5

$$\tau^n = A\dot{\gamma}$$

where, A is constant and $\dot{\gamma}$ is shear strain rate. It should be mentioned that the n, the power low exponent is equal to unity for Newtonian viscos materials (Jaeger et al., 2007).

2.5. Creep behavior of shale rocks

In this section, some significant published studies on the general creep behavior of rocks with a focus on shale rocks are presented and summarized.

The investigation carried out by Griggs (1939) is recognized as the pioneer study on the creep behavior of rocks. Griggs, 1939 obtained an empirical equation through curve-fitting the results of laboratory tests on the creep deformation of different types of rock including shale:

Equation 6

$$S = A + B \log t + Ct$$

where,S is the fractional deformation, t is time, A is the elastic strain, and B and C are constants. Figure 5 shows one of the first uniaxial creep tests that was carried out on shale rock sealed with paraffin.

Creep models are categorized in three main classes:

1. Burger's model (Figure 6).

2. Poynting-Tomson (Figure 6)

3. Power law
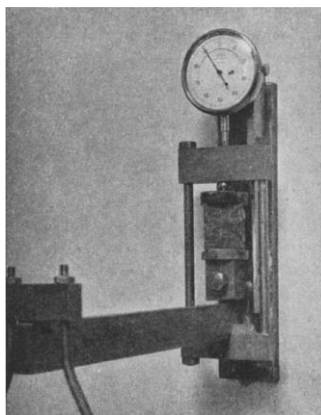
Figure 5. Uniaxial creep test on shale sample, appropriate amount of weight is hung of a lever to apply load to sample (Griggs, 1939)

11
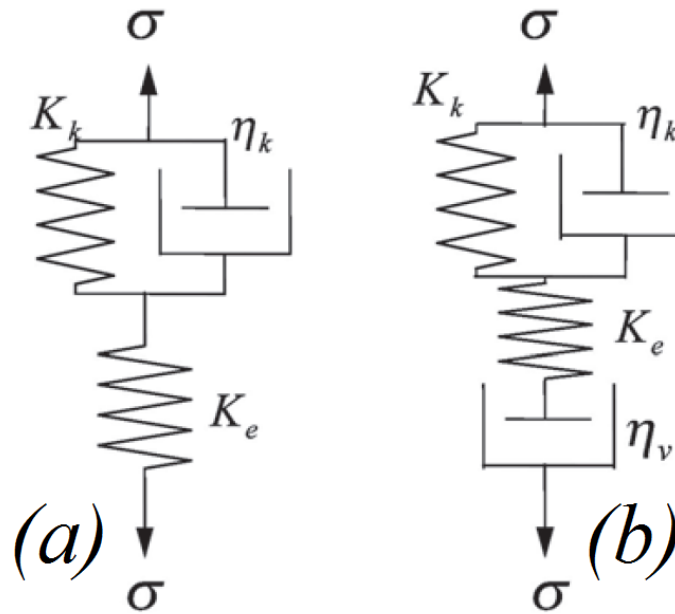
Figure 6. Two physical models: a) Poynting-Tomson b) Burger's model (Wu et al., 2009)

The Burger's model consists of four elements and the Poynting-Tomson model includes three elements, composed of the Kelvin and Maxwell models in series. The main deference between these two models is related to the secondary creep stage. The Burger's model can predict creep deformations when the strain rate decreases, while Poynting-Tomson model is more appropriate for increasing strain rates. However, the Power law model has widely been used in the literature, which can physically be associated to the Burger's model (Chin and Rogers, 1987).

Chin and Rogers (1987) conducted a series of creep tests on a variety of different rocks as well as shale rocks and demonstrated that the three-element model proposed by (Griggs, 1939) was not able to predict the creep behavior of rocks. It was shown that the

Burger's model can fit the experimental results better due to the dashpot representing the viscous behavior of rock compared to the Poynting-Tomson model.

Chang and Zoback (2009) conducted a series of creep tests under hydrostatic conditions as well as deviatoric loads. Their unconsolidated shale samples were taken from offshore Louisiana, the Gulf of Mexico. The results of hydrostatic tests indicated that increasing the confining pressure increases the creep volumetric strain. However, for confining pressures above 30 MPa, the volumetric strain remained fairly constant. A similar trend was observed for the deviatoric creep tests. A dramatic increase in the volumetric strain was also reported as σ_1 increased from 20.7 MPa to 25.4 MPa, but greater values of $\sigma 1$ resulted in slightly lower volumetric strains. The significant creep deformation of shale rock was ascribed to clay contents of it, according to the authors.

The results of a study carried out by Sone and Zoback (2011) indicated that the clay contents of Barnett, Haynesville, Fort St. John and Eagle Ford shale rocks significantly increased the creep strain. In contrast, confining pressure did not noticeably influence the creep strain, while deviatoric stress increased it slightly. The power low fitted well with a long-term data. However, a logarithm fit was found to be appropriate for three-hour creep data. It was shown that the creep deformation of samples is mostly visco-palstic, meaning that the creep deformation after unloading was not recoverable.

Li and Ghassemi (2012) reported the results of several uniaxial creep tests along with some triaxial creep tests on Marcellus, Barnett and Haynesville shale rocks which were obtained from different depths perpendicular to the bedding. The authors correlated the visco-elastic creep response with the clay content and elastic properties, characterized by elastic modulus, of the shale rocks. It was concluded that the stiffer shale with (high

13

quartz content) would demonstrate less creep deformation. Two models, power low and Burger's, were analyzed to fit the data and showed an acceptable match.

Almasoodi et al. (2014) reported the result of creep tests on Eagle Ford shale samples, which were dry, impregnated with water and impregnated with Decane. The results indicated that the sample impregnated with water showed the highest visco-elastic creep deformation, while creep deformation of dry samples was negligible. In this study, the Zener model was found satisfactory to predict the experimental results.
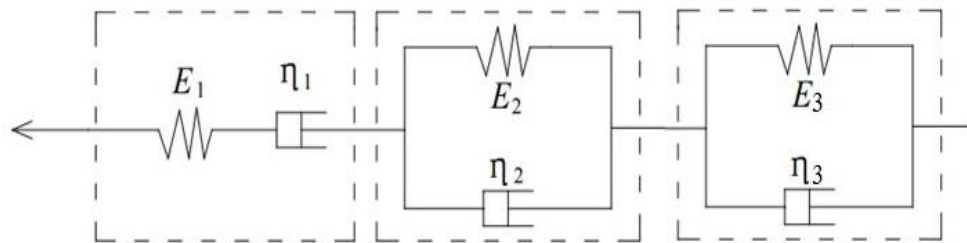
Figure 7. Zener model

2.6. Influence of anisotropy on the creep behavior of shale rocks

Clay and kerogen increase the mechanical anisotropy of rocks. Sone and Zoback (2013) found that the creep strain response of sample cored perpendicularly to the bedding was more than those cored along the bedding orientation. To explain such behavior, a simple model was referred, which consists of soft layers, representing kerogen and clay contents, and stiff layers, representing quartz and feldspar contents, according to Figure 8 when the load is applied perpendicular to the bedding the stress is equal for all the layers (iso-stress) and stiffness of the setting is the harmonic average of all layers. While, it is iso-strain condition in the case of parallel loading and the stiffness can be

obtained by arithmetic average of all the layers. Therefore, as expected, the stiffness of parallel loading is higher than the perpendicular one.

a) Iso-stress

Stiff
Soft
Stiff
Soft

$\sigma_{soft} = \sigma = \sigma_{stiff}$

$\varepsilon_{soft} > \varepsilon > \varepsilon_{stiff}$

b) Iso-strain

Stiff | Soft | Stiff | Soft

$\sigma_{soft} < \sigma < \sigma_{stiff}$

$\varepsilon_{soft} = \varepsilon = \varepsilon_{stiff}$
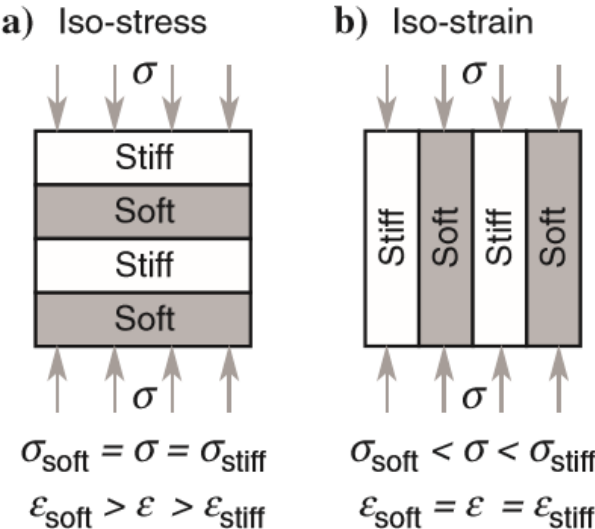
Figure 8. a) iso-stress condition (perpendicular loading), b) iso-strain condition (parallel loading)

Conducting uniaxial and triaxial tests, Masri et al. (2014) reported the results of an investigation on the mechanical behavior of a shale rock under elevated temperatures with the focus on the anisotropic response. Compared to the radial strains, greater axial strains were observed for the perpendicular samples, while dilatancy was greater in the parallel samples. The parallel samples exhibited the higher axial strength and Young's modulus in contrast to the perpendicular ones. However, Young's modulus of the parallel samples was more sensitive to the confining pressure.

2.7. Influence of temperature on the mechanical behavior of shale rocks

The influence of temperature on the mechanical properties of rocks has been the subject of numerous studies in the literature. These studies have consistently indicated that the temperature tends to reduce the strength of rocks.

Zhang et al. (2010) conducted a series of triaxial tests on one type of volcanic tuff rock called Ohya under isothermal condition. Their results showed the adverse influence of temperature on the peak strength of the rock while increasing its ductility (Figure 9).
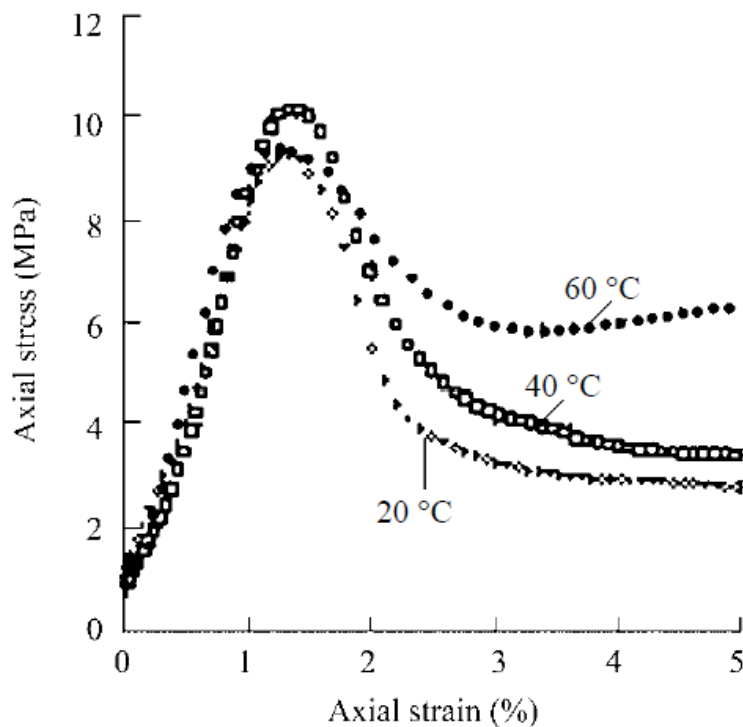
Figure 9. Axial stress vs. axial strain (Zhang et al., 2010)

Mohamadi et al. (2013) conducted triaxial compression tests on Westage Canada sedimentary shale under temperatures of 25, 85 and 135°C. Their results indicated that increasing the temperature results in a reduction in the peak and ultimate strengths and

the elastic modulus of the rock. Similar to the findings of Mohamadi et al. (2013), Masri et al. (2014) performed uniaxial and triaxial tests under high temperature from 20°C to 250°C to investigate the mechanical behavior of Toarcian shale rock samples in both orientations with respect to the bedding (i.e. parallel and perpendicular). Generally, it was observed that the rock exhibited more ductility as the temperature increased, while the peak compression strength of the rock decreased. Also, the Poisson's ratio showed a drastic reduction due to the increase in the temperature.

Oldakowski et al. (2016) conducted triaxial tests on two sets of shale samples cored from the Clearwater formation. The samples were allowed to achieve saturation and consolidation. Contrary to the findings of abovementioned studies, results of Oldakowski et al. (2016) indicated an increase in the Young's modulus and strength of samples due to elevating the temperature to 200°C. This unorthodox behavior of this particular shale rock is possibly due to thermal consolidation (Bois and Mainguy, 2011).

In geomechanics and geotechnics, thermal consolidation is a thermal-hydro-mechanical (THM) phenomenon that arises when temperature gradient and mass movement are coupled (e.g., in the heating released from buried nuclear waste, or from biological reactions in landfills). In a THM process, conduction and convection heat fluxes change the pore fluid velocity and the mechanical work of the volumetric strain. Simultaneously, the mechanical deformations rearrange the material constituents and in turn alter the pore fluid pressure. For rocks, thermal consolidation implication is usually a significant increase in cohesion and a reduction in friction angle (Zhang and Michalowski, 2015).

2.8. Influence of temperature on creep of rocks

Kranz et al. (1982) reported a series of static fatigue (creep) tests on Barre and Westerly granites at two temperatures of 24 and 200°C under dry and wet conditions. Results showed that temperature has a degrading effect on the strength of rock and reduced the time to failure by two orders of magnitude. Schutjens (1991) was the first to conduct uniaxial creep tests on rock at elevated temperatures. The tests were carried out on continental quartz sand sample drilled from the Bolderiaan formation. The Arrhenius equation was used to describe the creep phenomenon:

Equation 7

$$\beta^{\cdot} = A. \sigma_e^b. e_v^c . \exp(-\frac{\Delta H}{RT})$$

where, $\beta^{\cdot}$ is the strain rate, σ_e is the effective stress, e_v is the volumetric strain, ΔH is activation energy, R is the gas constant and T is temperature in Kelvins (Figure 10). The coefficients were obtained for both dry and saturated samples. Results showed a significant influence of saturation on creep deformations where a range of 11%–16% was obtained for the volumetric strain of saturated samples compared to negligible values for dry samples.

Conducting triaxial creep tests on sandstone at elevated temperatures, Heap et al. (2009) reported that increasing the temperature increases the creep strain rate for any deviatoric stress. The results showed that increasing the temperature from 25 ˚C to 75 ˚C results in three orders of magnitude increase in the creep strain rate. It was also shown that temperature adversely influences the strength through facilitating the continued growth of fractures.
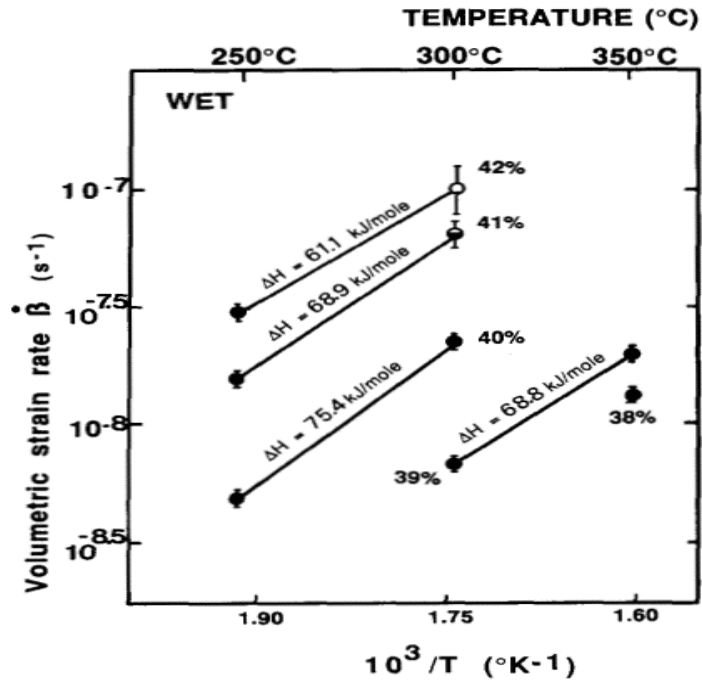
Figure 10. Arrhenius equation plot (volumetric strain vs. 1/T based on Equation 7) (Schutjens 1991)

Zhang et al. (2010), loaded Ohya rock, which is a volcanic tuff rock, at a constant rate to a desired strain followed by a constant load at 20 °C, 40 °C and 60 °C. An acceptable consistency was observed between the results of creep tests and a proposed thermo-mechanical model. It was shown that creep rupture was facilitated and accelerated by temperature.

Ghassemi, A and Suarez-Rivera (2012) reported the results of hydrostatic and deviatoric triaxial creep tests on Haynesville shale samples at three temperatures of 25 °C, 40 ˚C and 60 °C and another series of creep tests at 40 ˚C to 140 ˚C. Their results indicated an increase in the axial strain rate due to increasing temperature to the extent that the last stage of the test, conducted at 140 ˚C, followed to failure after a short steady-state creep.

19

Zhao et al. (2016) made a comparison between the strain rates of more than 180 creep tests. Although the significant influence of temperature on the creep strain rate was predictable, a slight increase in temperature from 65 ˚C to 75 ˚C led to several times increase in the strain rate. The power law was used to fit the data.

Chapter 3: Experimental procedure for creep tests on shale rocks

This chapter describes the procedure that was followed to study the time-dependent behavior of shale rocks with an emphasis on the influences of temperature and anisotropy.

3.1. Introduction

Five different types of shale rocks were selected for the laboratory investigation of the creep behavior of shale rock. These shale rocks included Eagle Ford, Mancos, Barnett, Pierre and Haynesville. The depth from which the samples were collected was known for the Barnett, Haynesville and Eagle Ford samples (the depth of 1692.36 m for Barnett and 3840 m for Eagle Ford). Expect for the Eagle Ford sample that was of 1.5 in (3.81 cm) diameter, the diameter of other samples was 1 in (2.54 cm).

The influence of anisotropy on the mechanical and creep behaviors of shale rock was studied. For the Mancos, Barnett, Haynesville and Pierre shale samples, one sample cored perpendicularly (denoted as PAB) and the other cored parallel to the bedding (denoted as PEB) were tested. The Eagle Ford samples, however, were perpendicular to bedding. Deviatoric creep tests were carried out at room temperature (i.e., 25 °C) and 50 °C to investigate the influence of temperate. Attempts to perform deviatoric creep tests on the Eagle Ford samples at high temperature yielded.

3.2. Hydrostatic creep test

Hydrostatic test is a simple mechanical test where a confining pressure is applied on the boundaries of a rock sample exposed to the confining fluid. In the hydrostatic test,

a rock sample is placed inside of a triaxial cell, which is filled with a fluid such as oil that supplies a uniform pressure on the sample. A pump with a pressure controller is required to regulate the desired pressure. Sample should be coated with an impermeable cover such as a heat shrink or a copper jacket to protect the sample against the confining fluid. Using this test, the volumetric strain of the sample can be calculated as (Eq. 3).

Equation 8

$$\varepsilon_v = \varepsilon_1 + \varepsilon_2 + \varepsilon_3$$

where, ε_v is the volumetric strain and $\varepsilon_{i\ (i=1,2,3)}$ is the strain in the direction of principle stresses. For the case of triaxial test where ε is equal in two directions, the volumetric strain can be obtained as:

Equation 9

$$\varepsilon_v = \varepsilon_l + 2\ \varepsilon_r$$

The bulk modulus can then be obtained through:

Equation 10

$$K = \frac{\sigma_m}{\varepsilon_v}$$

Where, K is the bulk modulus and σ_m is the mean stress, which is equal to confining pressure in the hydrostatic test. It is noteworthy to mention that the test allows the calculation of the sample bulk compressibility through changing the pore fluid pressure. However, bulk compressibility is beyond the scope of this research. The schema of the hydrostatic test system is outlined in Figure 11.

To study the creep behavior of rock under the hydrostatic condition, it is required to keep the confining pressure constant over a desired duration. Therefore, electronic controller requires to be programmed for this purpose (Jaeger et al., 2007)
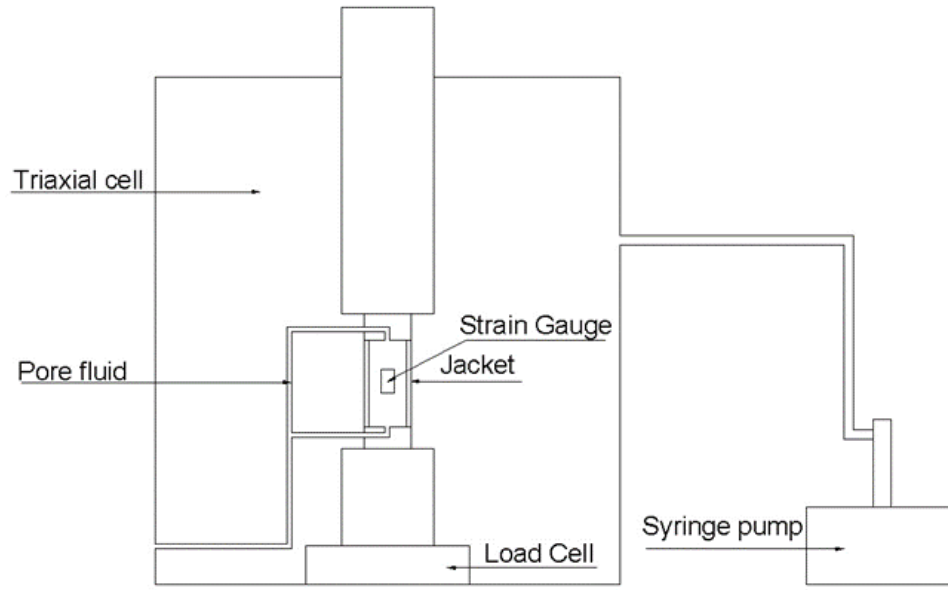
Figure 11. Schematic outline of the hydrostatic test system

3.3. Deviatoric creep test

Unlike the hydrostatic test where all stresses are equal in different directions, the triaxial test involves applying a different (usually greater) axial principle stress compared to the other two principle stresses, which are equal and applied by a pressurized fluid in the test cell. However, this is far from reality, as it is rarely the case in bedrock or in the wellbore vicinity.

Similar to the hydrostatic test, a cylindrical sample is used for this test. Therefore, strain in two directions, axial and radial, as well as the confining pressure need to be measured. Vertical stress in excess of the confining pressure (known as the deviatoric stress) is applied by means of a plunger (piston) and its value is recorded using a load cell (Figure 12).
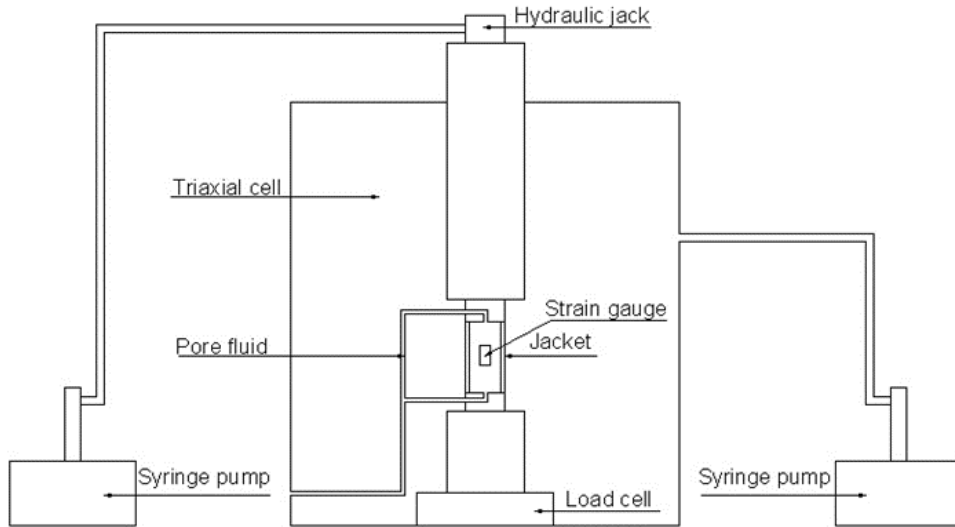
Figure 12. Schematic outline of the deviatoric test system

3.4.Experimental setup

The equipment used to perform the creep tests are described in the following sections. They include a compression machine, two syringe pumps, a hydraulic jack and strain gauges.

3.4.1. *Triaxial compression machine*

The Material Test System machine (MTS 816) located in the OU Reservoir Geomechanics Research Group Lab was used to carry out the creep tests. This compression servo-control machine consists of a servo-hydraulic load frame, a servo-hydraulic controller, an air compressor, a servo supercharger and a cell.

The frame of this test system comprises a fixed crosshead welded to four underpinning columns. An actuator in the apparatus was used to ensure that the sample was in contact with the piston. To this end, the samples would be raised slowly until they

were in contact with the piston. Subsequently, they were elevated until the actuator would show a value of 0.5 kN. Actuator is equipped with high pressure fluid to move up or down to generate or release the load. The load which is applied to the sample is resultant of effective hydraulic pressure. The deviatoric stress was applied using a syringe pump and a hydraulic jack (Figure 13).
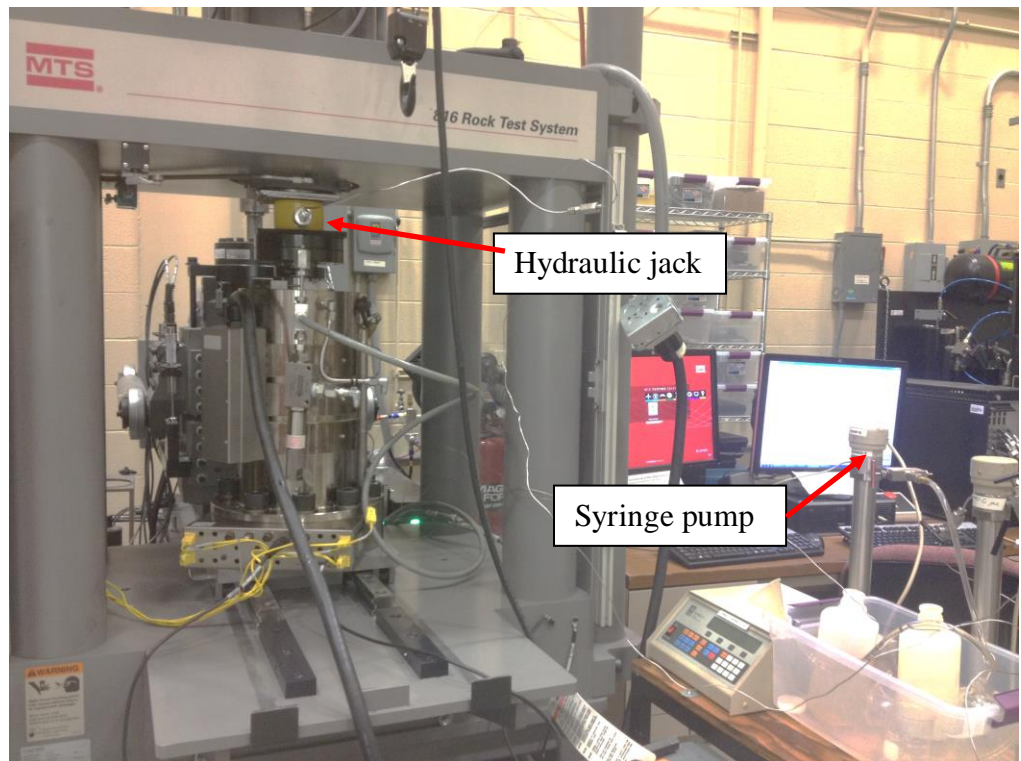
Figure 13 . Triaxial compressive creep testing setup

An accurate heating setup equips the test system. Two heating bands adhere to the cell providing the heat that would diffuse through the confining liquid to reach and raise the temperature of the sample. Five thermocouples were used to monitor and record the temperature (Figure 14). One of the thermocouples was placed on the exterior surface of the cell, while two thermocouples were situated in the close vicinity (in less than 4 mm

distance from sample) of the sample and two others at the bottom of the cell. A lower temperature was consistently observed for those located at the bottom of the cell. However, the heating process was controlled based on the temperatures recorded by the thermocouples close to the sample.
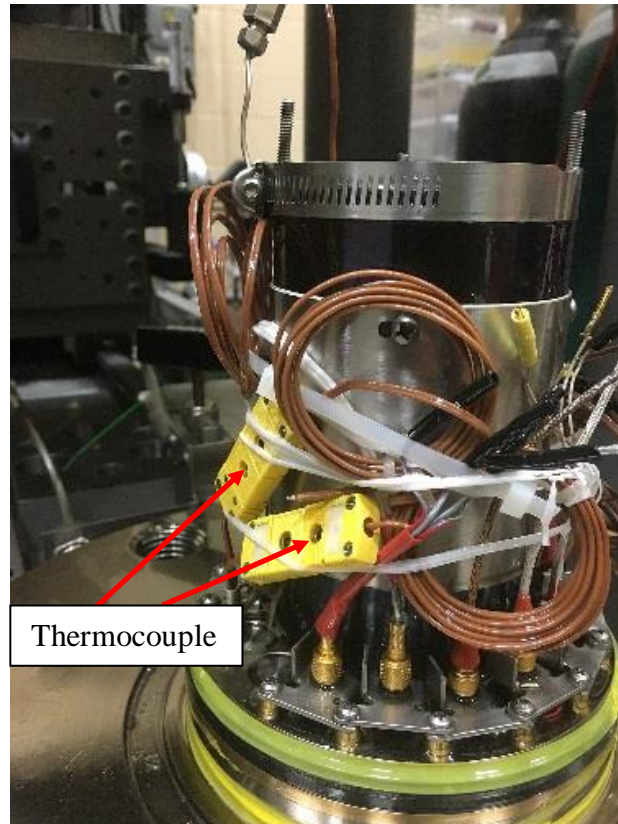
Figure 14. Load cell and thermocouples

3.4.2. *Strain gauges*

Proper strain gauges were adhered on the samples in two orientations of parallel and perpendicular to the bedding in order to measure axial and radial strains. Strain gauges consist of tiny wires made of specific alloys including constantan or nickel-chromium with a zigzag pattern providing an electrical resistance. The strain is measured

based on the fact that the electrical resistance of a material changes due to elongation. When a sample is compressed, strain gauges shorten, and their electrical resistance decreases. This change in the strain gauge resistance is characterized by a parameter known as gauge factor which is defined as:

$$GF = \frac{\Delta R / R}{\varepsilon}$$
Equation 11

where, ΔR is the resistance change, R is the strain gauge original resistance and ε is the strain (Sciammarella and Sciammarella, 2012).

It is of great importance to select appropriate strain gauges for specific environmental conditions. The influence of temperature on the creep behavior of rocks was one of main features of this study. Therefore, it was necessary to use self-temperature-compensated strain gauges. Strain gauges that were used in this study were product of Omega® and were of 120 ohm resistance and gauge factors of around 2. One of the strain gauges is shown in Figure 15.
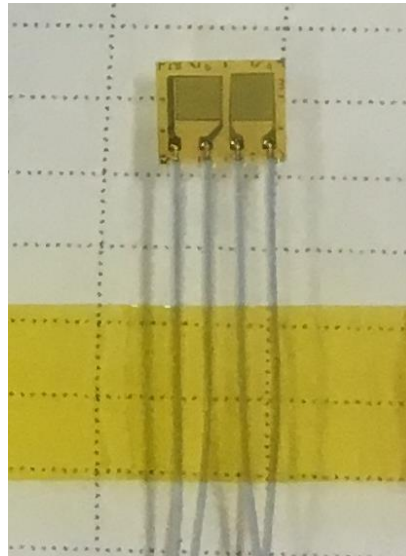
Figure 15. Strain gauge used in this study to measure axial and radial deformations of sample

Strain gauges are sensitive and are to be calibrated so as to ensure desired accuracy. To calibrate the strain gauges a resistance was shunted to the Wheatstone bridge as shown in Figure 16. As the shunt resistance results in a reduction in the resistance of Wheatstone bridge, it is representative of compressive strains. This stimulated strain is related to the shunt resistance by:

$$\varepsilon_S = -\frac{R_G}{F_G(R_G+R_C)}$$
                                                                    Equation 12

where, ε_S is the stimulated strain, R_G is the strain gauge resistance, R_C is the shunt resistance and F_G is the gauge factor. If the strain shown by strain gauge is reasonably close to what is obtained by the above equation, strain gauge is calibrated.
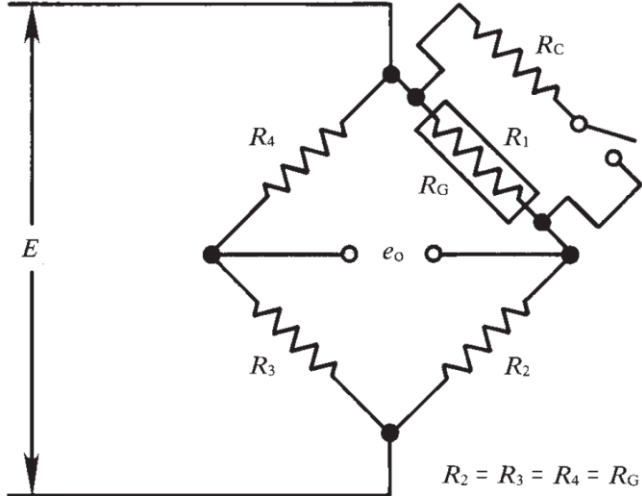
Figure 16. Shunt calibration (Vishay precision group, 2013)

3.4.3. Sample preparation

The American Society of Testing Material (ASTM) standards were followed for the preparation of all samples. Prior to preparation, samples were wrapped in plastic cover

and kept in a controlled condition in order to protect them from humidity, which can significantly influence rock properties.

Preparation of samples included three stages of coring, cutting and polishing. The first two stages of preparation had been already done for most of the samples prior to delivery to the Lab. Coring and cutting of untreated samples, however, were carried out in the Lab. Instead of water, air was used to cool down the blade in the cutting stage because shale rocks are sensitive to water. A length to diameter ratio of 2:1 was used for all samples. The samples were carefully flattened at ends by a grinder and a fine sand paper to an ASTM-specified acceptable tolerance of 0.001 inch in order to avert bending under a vertical load.

Prior to testing, samples were enclosed in a copper jacket using a heat gun (Figure 17 and Figure 18). For each sample, at least three strain gauges, two axial and one radial, were mounted on the jacket to measure deformations (on the middle of sample). The attachment of strain gauges to the samples was done very carefully to prevent inaccurate measurements resulting from the non-alignment of strain gauges with the sample longitudinal and radial axes. Scotch-weld epoxy was used to attach the sample to the platen and seal it (Figure 19). The curing time of this epoxy is recommended to be more than 6 hours.

Figure 17. Sample wrapped in copper jacket

Figure 18. Sample preparation

Figure 19. Strain gauges installation

The melting points of all the materials and instrumentation used in this study (e.g.,

wires) were ensured to be greater than the highest temperature applied through a trial test.

One of the issues in early stages of this research was temperature-induced loosening of

30

connections that would in turn result in inaccurate measurements. To circumvent such problem, all the connections were firmly covered with a Teflon tape prior to testing and a plastic zip tie was then used to make the connections even firmer.

3.5. Testing procedure

Two series of tests were devised to investigate the hydrostatic and deviatoric creep, testing procedures of both hydrostatic and deviatoric creep tests were designed stepwise in order to have a better understanding of the mechanical properties and creep behavior of rocks. In hydrostatic series of tests, a hydrostatic pressure was applied in a cumulative approach, while the axial load was incrementally increased in deviatoric creep tests. The deviatoric stress was ensured not to exceed half the peak stress so as to operate in the samples elastic regime and without approaching failure.

3.5.1. Hydrostatic creep test

The samples used in this study were of different properties and cored from different locations and depths. Among all the shale rocks studied in this research, the Pierre shale sample showed a significantly softer response to loading compared to other shale rocks. Therefore, it was quite impossible to design the same procedure for the Pierre shale sample as for other shale rocks. To put it into perspective, two stages of hydrostatic creep tests were designed for the Barnett, Mancos and Haynesville shale under 30 and 60 MPa confining pressure. The Pierre shale sample, however, showed a large strain of 1% under 30 MPa confining pressure. Thus, the second stage of hydrostatic creep on the Barnett shale was not feasible for the Pierre shale, as it would have resulted in

31

compression failure. Therefore, the two stages of hydrostatic creep tests on Pierre shale were carried out under two confining pressures of 10 MPa and 30 MPa. All the hydrostatic creep tests are summarized in Table 1.

Table 1. Hydrostatic creep test

Rock type	Confining Pressure (MPa)	Temperature (°C)	Condition	Zone and quality (Ghassemi, Suarez-Rivera, 2012)	Sample number (Ghassemi, Suarez-Rivera, 2012)
Eagle Ford	30	25	Moist/Drained	-	
Eagle Ford	40	25	Moist/Drained	-	
Eagle Ford	60	25	Moist /Drained	-	
Eagle Ford	70	25	Moist /Drained	-	
Mancos PAB	30	25	Dry/Drained	-	
Mancos PAB	60	25	Dry/Drained	-	
Mancos PEB	30	25	Dry/Drained	-	
Mancos PEB	60	25	Dry/Drained	-	
Barnett PAB	30	25	Dry/Drained	Olive, fair	3-27
Barnett PAB	60	25	Dry/Drained	Olive, fair	3-27
Barnett PEB	30	25	Dry/Drained	Olive, fair	3-24
Barnett PEB	60	25	Dry/Drained	Olive, fair	3-24
Pierre PAB	10	25	Dry/Drained		
Pierre PAB	30	25	Dry/Drained		
Pierre PEB	10	25	Dry/Drained		
Pierre PEB	30	25	Dry/Drained		
Haynesville PAB	30	25	Dry/Drained	Light blue, best	5-28
Haynesville PAB	60	25	Dry/Drained	Light blue, best	5-28
Haynesville PEB	30	25	Dry/Drained	Light blue, best	5-25
Haynesville PEB	60	25	Dry/Drained	Light blue, best	5-25

In the hydrostatic creep stages, the Mancos shale, Barnett and Haynesville shale samples were subjected to 30 and 60 MPa to compare their creep behavior under the same confining pressure. Their properties were more similar. Two Barnett samples were drilled from a depth of 5552.95 ft. (1.69 km), where a minimum principle stress of 30 MPa is estimated. This estimation was calculated based on the bulk density of Barnett shale rock and the depth from which the samples were drilled.

The procedure designed for Eagle Ford shale was slightly different from other shale samples. The hydrostatic creep stages consisted of four stages. The confining pressure applied to the sample included 30, 40, 60 and 70 MPa.

The bulk moduli of the studied shales were calculated under the same confining pressure of 30 MPa. The results are presented in the next chapter. It is noteworthy to mention that all the hydrostatic tests were carried out under room temperature and no attempt was made to study the influence of temperature on the hydrostatic creep behavior of shale rocks.

3.5.2. *Deviatoric creep test*

After hydrostatic creep tests, deviatoric creep ones were conducted on the same samples. Similar to the hydrostatic creep tests, procedures were designed differently for various shale rocks due to their diverse origins and properties. As mentioned, the Pierre shale is dramatically softer than other tested shale rocks. Therefore, it might have failed under the moderate deviatoric stress that was used for the Mancos, Barnett, Haynesville or Eagle Ford shales. All the loading stages were designed such that the samples would remain in their elastic regime, even at elevated temperatures. All deviatoric creeps test are summarized in Table 2.

The pore fluid connection was left open to the outside of the cell to let pore fluid expel, providing the drained condition. However, most of the samples used in this study were dry, and no attempt was made to saturate them. Therefore, it was not expected that significant amount of fluid to be drained out of the samples. As a result, no significant

porosity reduction (consolidation) was expected due to increasing the effective stresses over time.

Table 2. Deviatoric creep tests

Rock type	Confining Pressure (MPa)	Temperature (°C)	Condition	Deviatoric stress (MPa)	Zone and quality (Ghassemi, and Suarez-Rivera, 2012)	Zone and quality (Ghassemi, and Suarez-Rivera, 2012)
Eagle Ford	30	25	Moist/Drained	12		
Eagle Ford	30	25	Moist/Drained	20		
Eagle Ford	30	25	Moist /Drained	30		
Eagle Ford	30	25	Moist /Drained	45		
Mancos PAB	30	25 and 50	Dry/Drained	35		
Mancos PAB	30	25 and 50	Dry/Drained	72		
Mancos PEB	30	25 and 50	Dry/Drained	35		
Mancos PEB	30	25 and 50	Dry/Drained	72		
Barnett PAB	30	25 and 50	Dry/Drained	18	Olive, fair	3-27
Barnett PAB	30	25 and 50	Dry/Drained	35	Olive, fair	3-27
Barnett PAB	30	25 and 50	Dry/Drained	72	Olive, fair	3-27
Barnett PEB	30	25 and 50	Dry/Drained	18	Olive, fair	3-24
Barnett PEB	30	25 and 50	Dry/Drained	35	Olive, fair	3-24
Barnett PEB	30	25 and 50	Dry/Drained	72	Olive, fair	3-24
Pierre PAB	10	25 and 50	Dry/Drained	5.2		
Pierre PAB	10	25 and 50	Dry/Drained	11.4		
Pierre PEB	10	25 and 50	Dry/Drained	5.2		
Pierre PEB	10	25 and 50	Dry/Drained	11.4		
Haynesville PAB	30	25 and 50	Dry/Drained	18	Light blue, best	5-28
Haynesville PAB	30	25 and 50	Dry/Drained	35	Light blue, best	5-28
`	30	25 and 50	Dry/Drained	72	Light blue, best	5-28
Haynesville PEB	30	25 and 50	Dry/Drained	18	Light blue, best	5-25
Haynesville PEB	30	25 and 50	Dry/Drained	35	Light blue, best	5-25
Haynesville PEB	30	25 and 50	Dry/Drained	72	Light blue, best	5-25

The deviatoric creep procedures were performed under 25 °C and 50 °C (and 70 °C only for Mancos PAB and Barnett PEB). Temperature was increased gradually to prevent the rupture of jacket due to emitted gas. Prior to applying the deviatoric stress, the samples were heated for 4 hours to reach thermal equilibrium (Chu and Chang, 1980). In the course of heating, free expansion was allowed as described by Chu and Chang (1980).

Similar deviatoric creep procedures were followed for three shale rocks, Mancos, Barnett and Haynesville. Their comprehensive properties are presented in the next chapter. For this series of tests, a confining pressure of 30 MPa was considered. The deviatoric stresses applied to these three shale rocks included 18, 35 and 72 MPa for Barnett and Haynesville shale and 35 and 72 MPa for Mancos shale.

As described before, the confining pressure acts as the minimum and intermediate principal stresses σ_2 and σ_3 in the triaxial test setting. A confining pressure of 10 MPa was used for the Pierre shale; the deviatoric stresses applied in two stages to the Pierre shale were 5.2 MPa and 11.4 MPa, much lower than those applied to other shale samples in deviatoric creep tests.

Chapter 4: Results and discussion

This chapter describes the results of the creep tests, hydrostatic and deviatoric, that were carried out on Eagle Ford, Mancos, Barnett, and Pierre shale rocks.

Since the numbers of samples were limited, it was not possible to obtain the peak strength by testing samples to failure. Therefore, the peak strength of each rock type was estimated based on the literature, and deviatoric stresses applied in each stage were ensured to be smaller than half of the peak stresses to remain in the elastic regime.

4.1. Mancos sample

To investigate the hydrostatic and deviatoric creep, two series of tests were planned (Figure 20 and Figure 21). In the hydrostatic creep stages, Mancos shale samples were subjected to 30 and 60 MPa confing pressure. Deviatoric creep tests on Mancos shale were performed with confining pressure of 30 MPa. Deviatoric stresses of 35 and 72 MPa were applied to Mancos shale samples. It is worth mentioning that a study by Pe'rez et al. (2015) showed that Mancos shale samples subjected to 30 MPa confining pressure and cored perpendicularly to the bedding failed at a peak stress of 136.3 MPa, which is approximately twice as much the deviatoric stress applied during the second stage of the tests carried out in the current study (i.e. 72 MPa). Table 3 presents the mineralogy of Mancos shale. According to this table, the clay content of this shale rock is 36.62% and the dominant mineral of Mancos shale is Quartz.

Figure 20. Mancos PAB specimen before testing

Figure 21. Mancos PEB specimen before testing

Table 3. Mineralogy of Mancos shale

Quartz	Calcite	Dolomite	Illite	Smectite	Kaolinite
45.447	4.078	5.19	36.621	0	0
Chlorite	Pyrite	Orthoclase	Oglioclase	Mixed Clay	Albite
0	0	0	2.01	0	6.166
Anhydrite	Siderite	Apatite	Aragonite		
0	0	0.489	0		

4.1.1. Hydrostatic creep of Mancos PAB

The results of hydrostatic creep test on Mancos shale PAB are shown in Figure 22 under confining pressures of 30 and 60 MPa at 25 °C. The sample experienced more deformation in the first stage compared to the second stage (Figure 22). Each creep curve consists of three stages, the strain rate of creep curve ($\Delta\varepsilon/\Delta t$) decreases in the primary stage, the onset of steady-state stage is when the strain rate becomes constant. Steady-state strain rate is the main characteristic of creep curve which can be obtained by linear regression on secondary stage part of creep curve. The creep test duration should be long enough to calculate this value accurately. Therefore, the creep test under higher load, and higher temperatures were maintained for a longer time due to having longer primary creep stage to reach the steady-state. The linear regression analysis on the secondary stage of creep test were done on Figure 22 using least square method, which shows that the test reached steady-state.
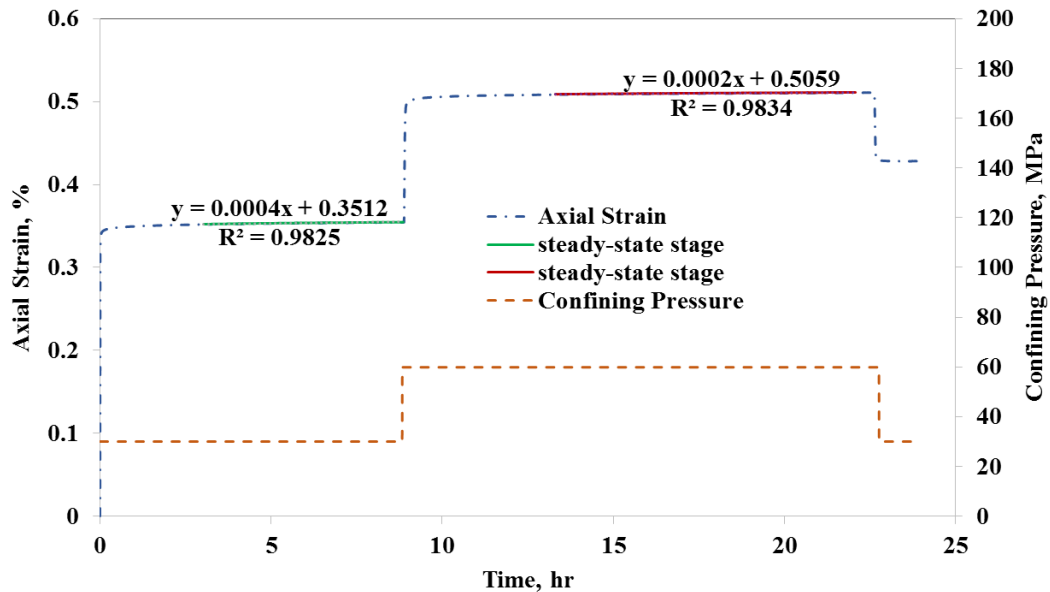
Figure 22. Hydrostatic creep of Mancos PAB

After unloading from 60 MPa to 30 MPa confining pressure, almost 50% of the rock deformation was immediately recovered, indicating high plastic deformation in this series of test. This observation suggests that the creep behavior of the Mancos shale under hydrostatic conditions was essentially more visco-elastoplastic. However, the sample deformation should have been recorded for a long enough period of time after unloading to determine the creep behavior of sample with certainty. Figure 23 shows the volumetric strain vs. time and the bulk modulus of sample was calculated using a linear regression on the instantaneous deformation parts as presented in Table 4. This table also shows the steady-state strain rate of creep test which is calculated by means of the linear regression analyses on secondary stages of Figure 22. The compressibility of the sample decreased in the second stage compared to the first one, unlike strain rate.
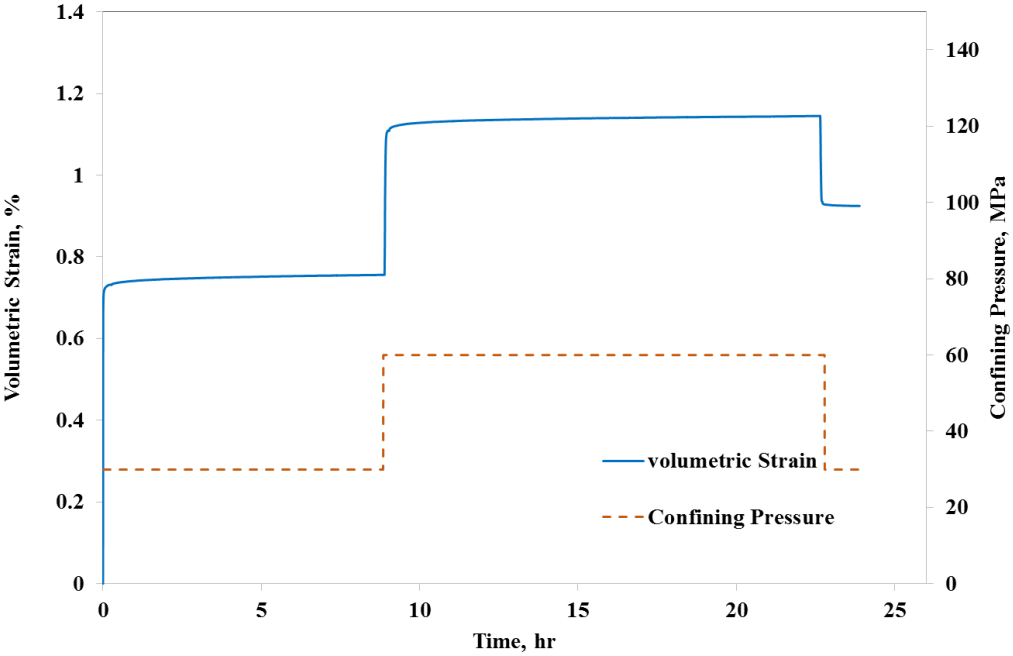
Figure 23. Volumetric strain vs. time of Mancos PAB

Table 4. Bulk modulus and strain rate of Mancos PAB

Confining Pressure (MPa)	K (GPa)	`Strain rate $\times 10^9$ (1/s)
30	4.36	1.11
60	6.44	0.55

4.1.2. *Hydrostatic creep of Mancos PEB*

The same procedure for hydrostatic creep on Mancos PEB was performed, under 30 and 60 MPa confining pressures. Results of the axial and volumetric strains are presented in Figure 24 and Figure 25, respectively. A similar behavior to the Mancos PAB is observed. However, more deformation recovered after unloading in contrast to the hydrostatic creep on the Mancos PAB, around 90%, indicating more elastic behavior of Mancos PEB.
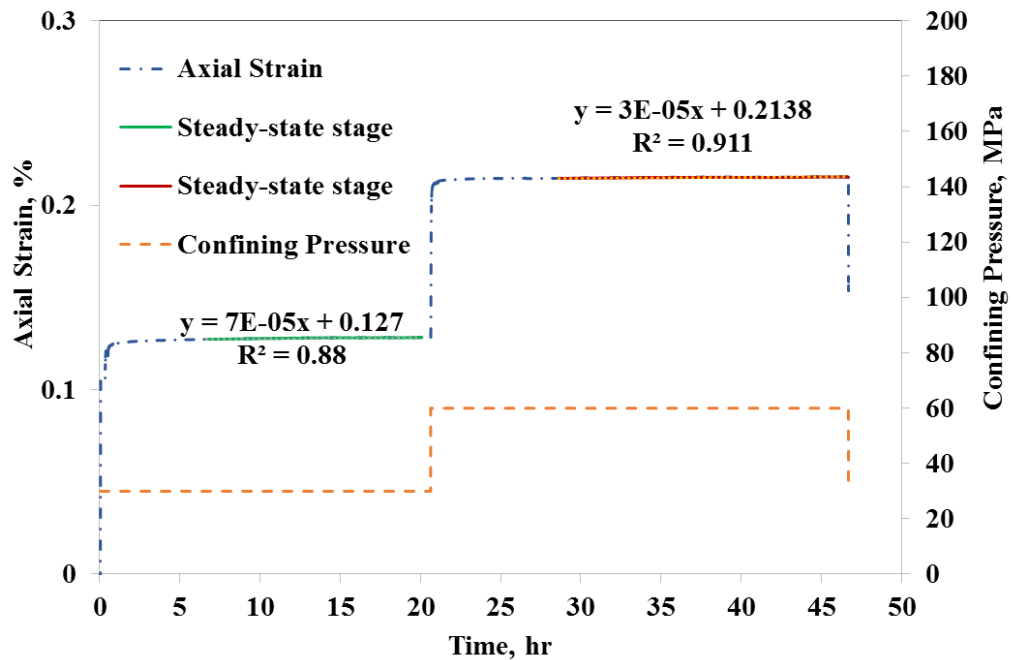
Figure 24. Hydrostatic creep of Mancos PEB

40
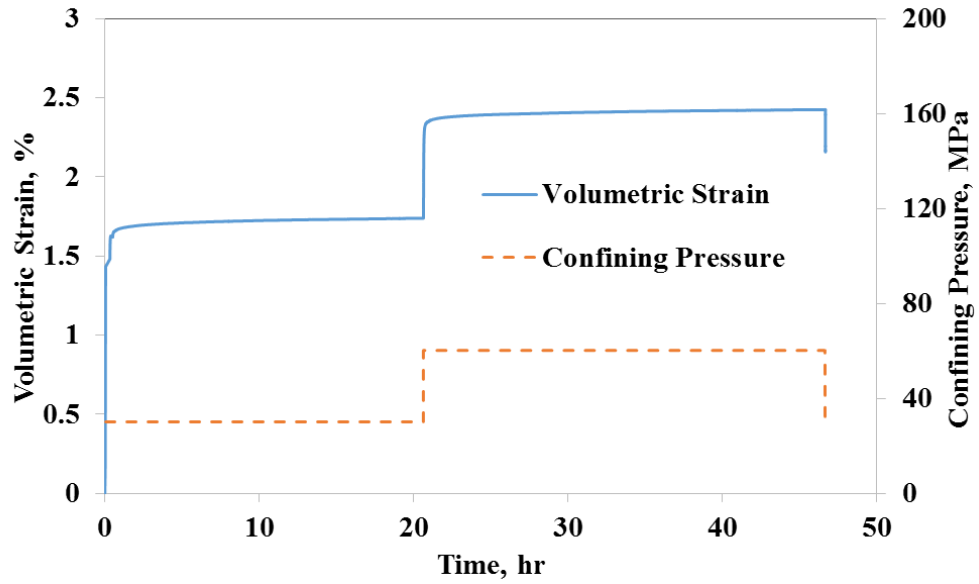
Figure 25. Volumetric strain vs. time of Mancos PEB

By comparing Figure 22 and Figure 24, we can conclude that the axial deformation of Mancos PAB under hydrostatic condition is greater than that of Mancos PEB. Unlike axial strain, the volumetric strain of the parallel sample is higher than that of the sample perpendicular to the bedding (Figure 23 and Figure 25). The strain rate of the sample cored perpendicular to the bedding was greater than that of the parallel one (almost one order of magnitude).

Table 5. Bulk modulus and strain rate of Mancos sample PEB

Confining pressure (MPa)	K (GPa)	Strain rate $\times 10^{10}$ (1/s)
30	1.82	1.94
60	3.08	0.83

4.1.3. Deviatoric creep on Mancos PAB

The deviatoric stresses of 35 MPa and 72 MPa at 25 °C and 70 °C were applied to Mancos PAB. Figure 26 and Figure 27 show the creep curve of the Mancos PAB vs.

41

time at 25 °C and 70 °C, respectively. More than 50 % of sample deformation due to deviatoric load was recovered, indicating that the creep behavior of Mancos PAB is probably visco-elastoplastic (Figure 26 and Figure 27).

Table 6 shows the elastic modulus of the sample under different conditions which were calculated by using linear regression on instantaneous deformation parts of Figure 26 and Figure 27. Table 7 shows the creep strain rate of the steady-state stages. As expected, the test carried out at a higher temperature and deviatoric stress has the highest strain rate, meaning deviatoric stress and temperature can facilitate failure (Table 7).
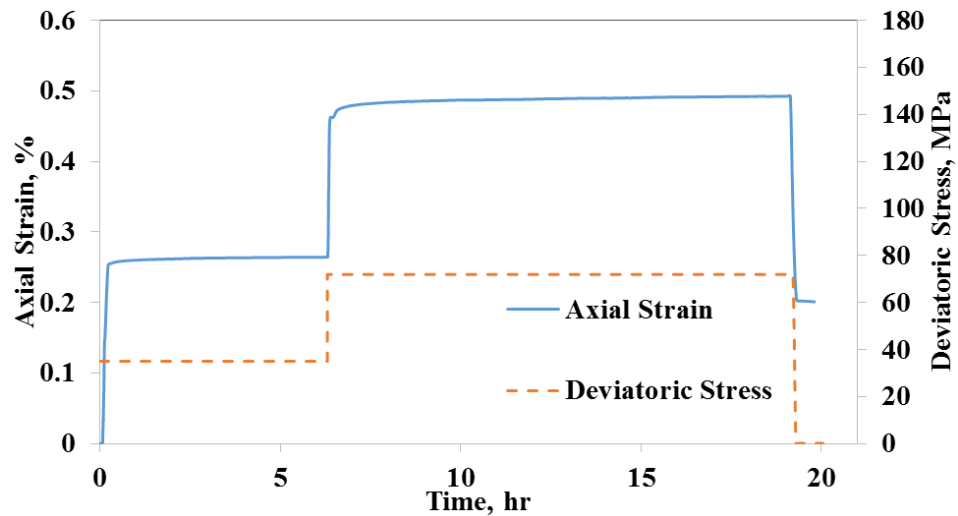
Figure 26. Deviatoric creep of Mancos PAB at 25° C

Table 6. Elastic modulus of Mancos PAB under different deviatoric stress and temperature (GPa)

	Deviatoric stress (MPa)	
Temperature (°C)	35	72
25	10.88	18.79
50	21.67	29.44

Table 7. Creep strain rate ×10⁹ of Mancos PAB under different deviatoric stresses and temperatures (1/s)

Temperature (°C)	Deviatoric stress (MPa)	
	35	72
25	1.13	1.82
50	2.38	2.94
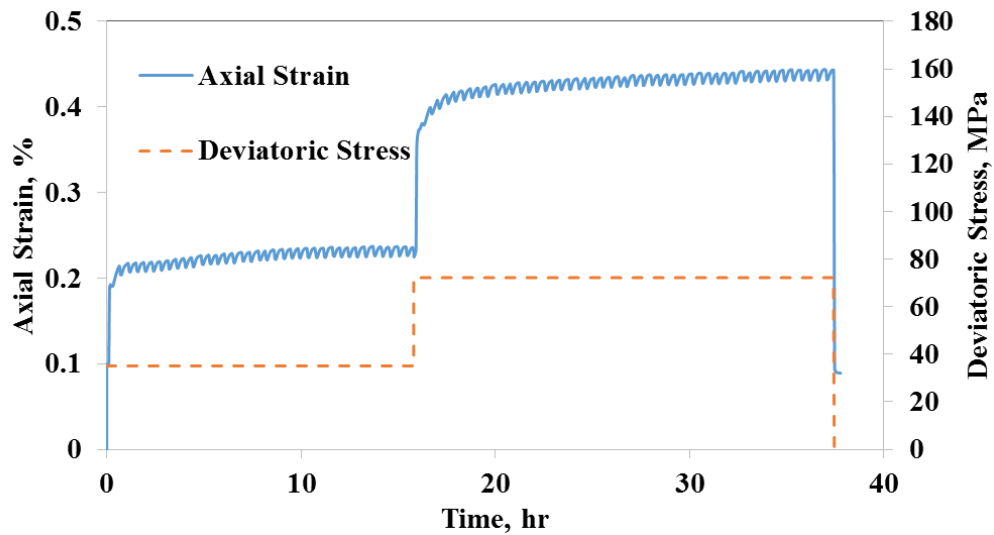
Figure 27. Deviatoric creep of Mancos PAB at 50 °C

Many studies in the literature have shown that power law is the appropriate function to describe the creep behavior of shale rocks (Li and Ghassemi, 2012; Sone and Zoback, 2011) . It is generally expressed as:

Equation 13

$$\varepsilon_{creep} = k\, t^n$$

where k and n are constants. Curve fitting was carried out using the least square fitting technique. The results are shown in Figure 28. It can be seen that the power law would be able to predict the creep behavior of Mancos PAB reasonably well. The

comparison between the power low exponents of different creep curves makes it clear that increasing the deviatoric stress and temperature would increase value of n.
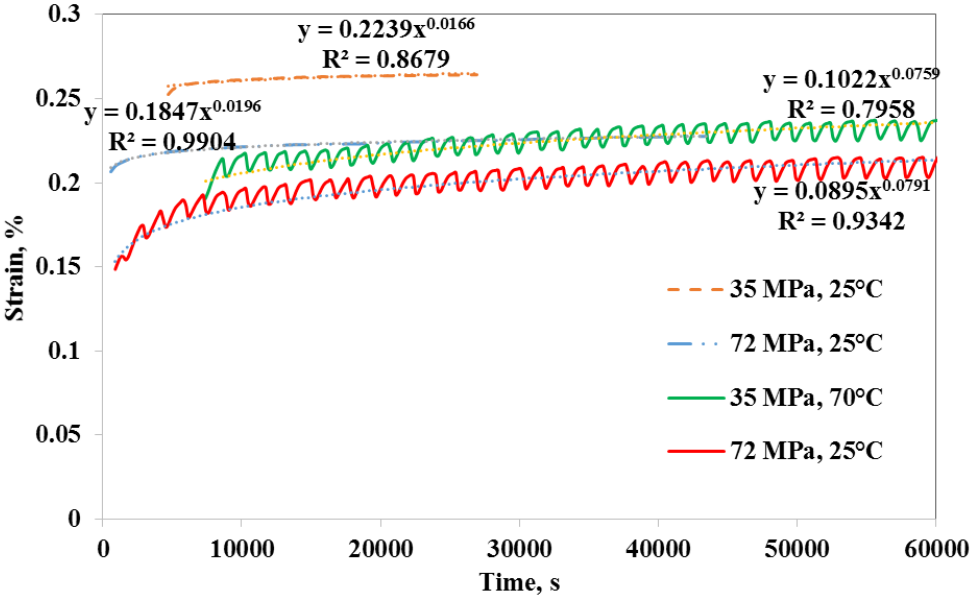
Figure 28. Power law curve fit to deviatoric creep strain vs. time for Mancos PAB

4.1.4. *Deviatoric creep on Mancos PEB*

The creep strain of Mancos PEB are shown in Figure 29 and Figure 30 and under the same deviatoric stresses as applied to the perpendicular sample. Juxtaposing the results of creep tests of the two Mancos shale samples indicates that the creep strain rate of perpendicular sample is higher than that of the perpendicular one, in the same manner parallel sample is stiffer and exhibits smaller instantaneous deformations. Similar results have been observed by (Sone and Zoback, 2013) in room temperature tests. The elastic modulus and the steady-state strain rate of Mancos PEB are presented in Table 8 and Table 9, respectively. The influence of temperature on the steady creep rate of Mancos

PEB is noticeable. The total deformation of sample is recovered, indicating a viscoelastic creep behavior of Mancos PEB.
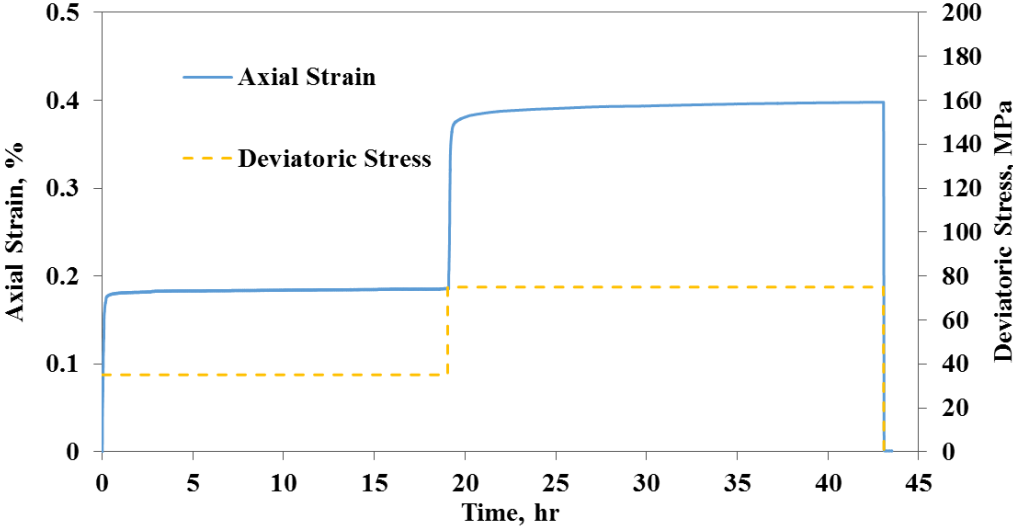
Figure 29. Deviatoric creep of Mancos PEB at 25 °C
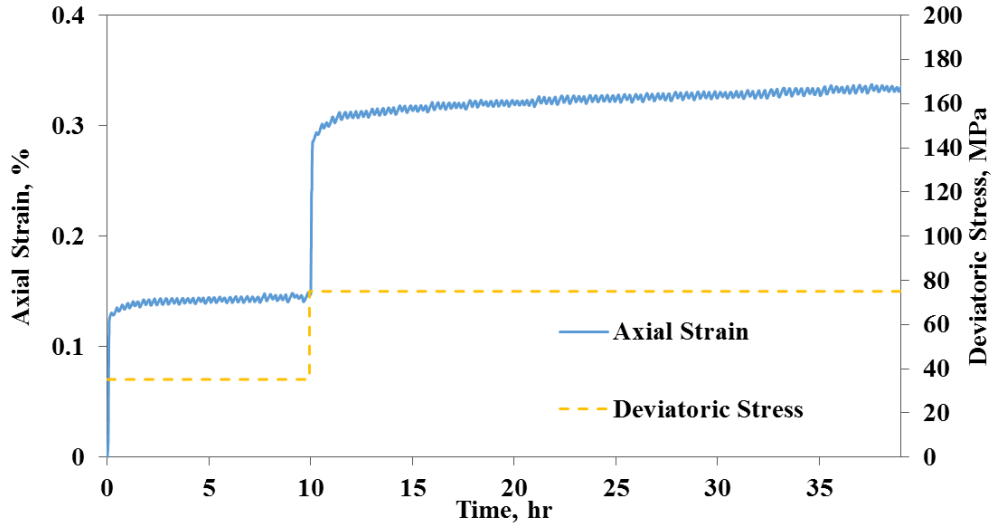
Figure 30. Deviatoric creep of Mancos PEB at 50 °C

Similarly, the power law was used to fit the creep strain vs. time of Mancos PEB as shown in Table 8. The R^2 of all the fitted curves were found to be greater than 0.9,

showing the suitability of power law to predict the creep of shale. Larger values were found for n under the higher temperature and deviatoric stress.
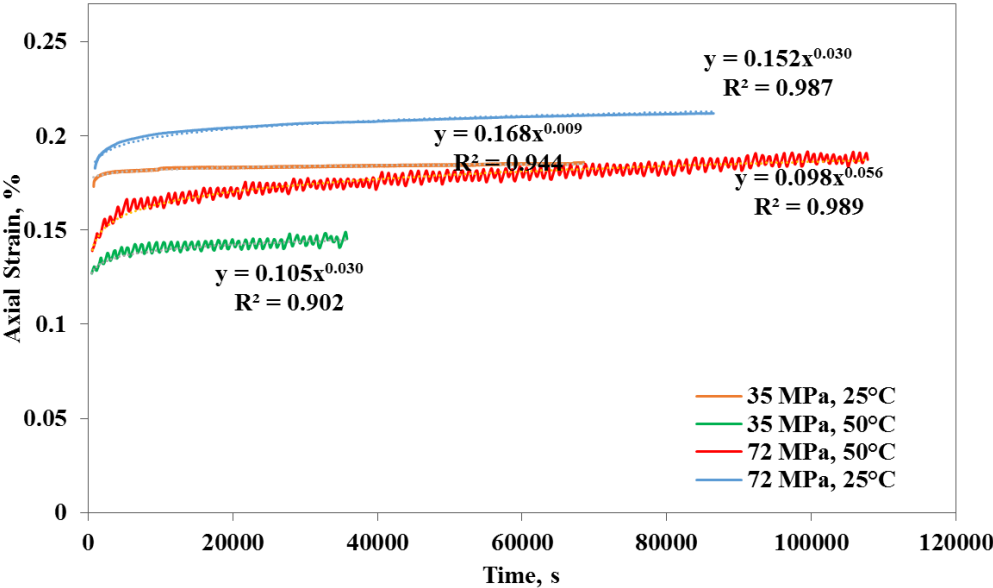
Figure 31. Deviatoric creep of Mancos PEB sample at 25 and 50 °C

Table 8. Elastic modulus of the Mancos PEB under different deviatoric stresses and temperatures (GPa)

	Deviatoric stress (MPa)	
Temperature (°C)	35	72
25	20.52	24.24
50	27.61	25.02

Table 9. Creep strain rate $\times 10^9$ of Mancos PEB under different deviatoric stresses and temperatures (1/s)

	Deviatoric stress (MPa)	
Temperature (°C)	35	72
25	0.44	1.08
50	1.78	1.92

4.2. Barnett samples

4.2.1. *Barnett shale formation*

The geological location of the Barnett shale formation, which mainly consists of sedimentary rocks, is Bend Arch-Fort Worth Basin, Texas, underlying the city of Fort Worth (13,000 km2). Based on the stratigraphic investigations, the main components of this formation are limestone and organic-rich shales (Ghassemi, A and Suarez-Rivera, 2012; Wikipedia, 2016).

It has been suggested that this formation supplied the largest natural gas in the United States, containing 71 km^3 of recoverable natural gas and 850 km^3 of in-place natural gas. The permeability of this shale gas is noticeably low and has been considered as tight shale gas, thus it has been widely exploited by means of hydraulic fracturing (Wikipedia, 2016).

Two series of creep tests were carried out on two Barnett samples, cored parallel and perpendicular to the bedding. The petrophysical, geochemical, geochemical properties (static and dynamic) and XRD mineralogy of these two samples were extensively investigated by Ghassemi, A and Suarez-Rivera (2012). In this study, the samples were collected from two wells of the Johnston County of this play and to categorize the samples, n-dimensional heterogeneous rock analysis (HRA) of well-log measurements was used. This approach has the capability to identify rocks based on their similarities in texture, composition, and material properties. The authors categorized all the samples in eight classes color-coded as: dark blue, yellow, red, brown, purple, olive, orange and gray (Figure 32).

Two Barnett samples were selected from Olive category and drilled from well 1 with high reservoir quality: high average measured porosity (7.8%), average gas-filled porosity (6.9%), and average calculated permeability (473 nanodarcies). Petrologic evaluations showed that this well include siliceous mudstones, mixed siliceous/calcareous mudstones, mixed siliceous/phosphatic mudstones, and mixed siliceous/argillaceous mudstones. The main authigenic mineral is recrystallized silica, which is admixed with silica making organic matter with high surface area. Illite and mixed-layer illite-smectite, with only trace amounts (< 1%) of chlorite and kaolinite are the dominant clay species. Based on HRA classification, olive category has the fair quality index.
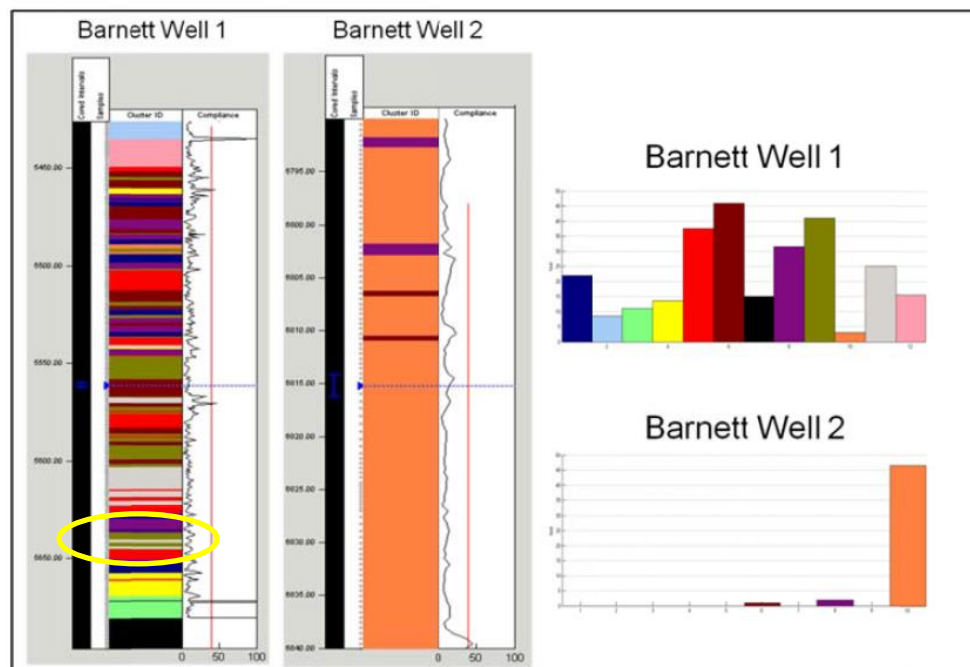
Figure 32. HRA classification of two wells in the Barnett formation (Ghassemi and Suarez-Rivera, 2012).

4.2.2. Sample description

Two Barnett samples 2.54 cm (1 inch) in diameter and 5.08 (2 inch) long were cored from the depth of 1692.36 m (5552.35 ft.) (Figure 33 and Figure 34).
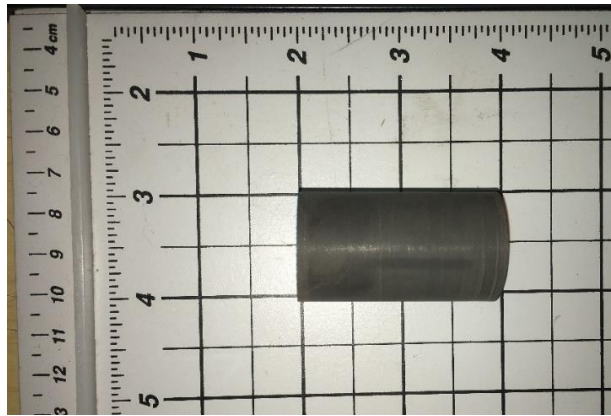
Figure 33. Barnett sample PAB
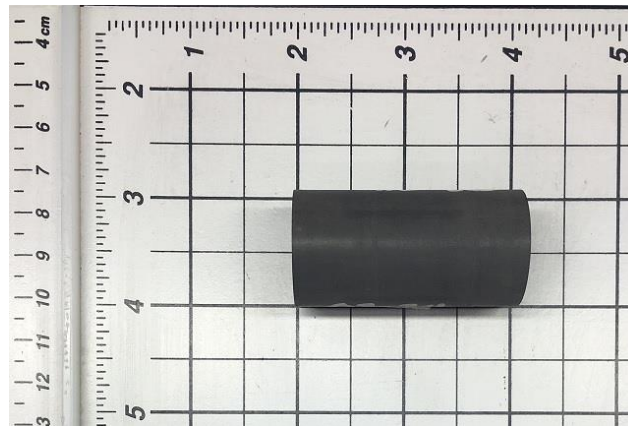
Figure 34. Barnett sample PEB

The petrophysical, geomechanical, geochemical properties (static and dynamic) and XRD mineralogy of them are presented as follows:

Table 10. Average Barnett petrophysical properties (Ghassemi and Suarez-Rivera, 2012)

Bulk density (g/cc)	Grain density (g/cc)	Dry Gas density (g/cc)	Effective porosity (%BV)	Water saturation (%PV)	Gas saturation (%PV)
2.48	2.57	2.6	5.34	12.95	71.17
Mobile oil saturation (%PV)	Gas filled porosity (%BV)	Bound hydrocarbon saturation (%BV)	Clay bound water (%BV)	Pressure decay permeability (nD)	No of samples
15.88	3.84	1.08	5.65	157	3

Table 11. Average Barnett geomechanical properties (static) (Ghassemi and Suarez-Rivera, 2012)

Bulk density (g/cc)	Effective confining stress (MPa)	Peak strength (V) (MPa)	Peak strength (H) (MPa)	Young's modulus (V) (GPa)	Young's modulus (H) (GPa)
2.52	17.66	116.98	146.55	19.86	31.23

Average Barnett geomechanical properties (static) (Ghassemi and Suarez-Rivera, 2012) (continued)

No of samples	Poisson's ratio (V)	Poisson's ratio (H)
3	0.131	0.162

Table 12. Average Barnett geomechanical properties (dynamic) (Ghassemi and Suarez-Rivera, 2012)

No of samples	Mean stress (MPa)	P-wave velocity (V) (m/s)	P-wave velocity (H) (m/s)	S-wave velocity (V) (m/s)	S-wave velocity (H) (m/s)
3	24.54	4133.7	4942.6	2478.6	2849.88
Bulk density (g/cc)	Young's modulus (V) (GPa)	Young's modulus (H) (GPa)	Poisson's ratio (V)	Poisson's ratio (H)	No of samples
2.53	34.82	51.2	0.234	0.226	3

Table 13. Average geochemical properties (Ghassemi and Suarez-Rivera, 2012)

No. of samples	Total organic content (% Wt)
3	4.2

Table 14. Barnett XRD mineralogy (Ghassemi and Suarez-Rivera, 2012)

No of samples	Quartz	Calcite	Total clay	Other
3	31	12	41	16

4.2.3. Hydrostatic creep of Barnett PAB

Figure 35 presents the results of hydrostatic creep tests on Barnett sample. Confining pressures of 30 and 60 MPa were planned for this series of tests with different durations.

The instantaneous deformation of the sample in the first stage is greater than that in the second stage, similar to what was observed for Mancos sample. This observation indicates a reduction in the compressibility of rock over time as bulk modulus of sample

increased in the second stage, almost twice as much as that in the first stage. (Figure 36 and Table 15). Unlike the instantaneous deformation, the creep deformation of the sample in the second stage is approximately quadrupled. After unloading, deformations of the rock are significantly recovered, showing insignificant plastic deformation. Therefore, the creep behavior of the Barnett shale is considered more visco-elasto-plastic. However, after unloading measurements should have been continued to determine the creep behavior of a rock with certainty.
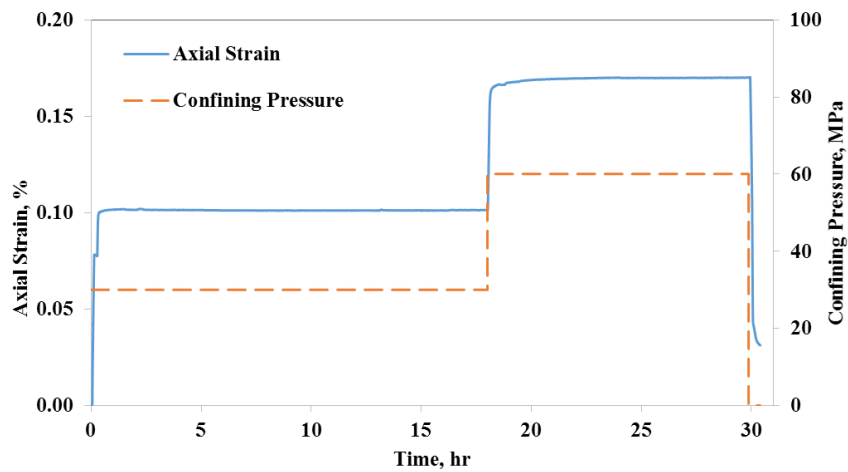
Figure 35. Hydrostatic creep of Barnett PAB
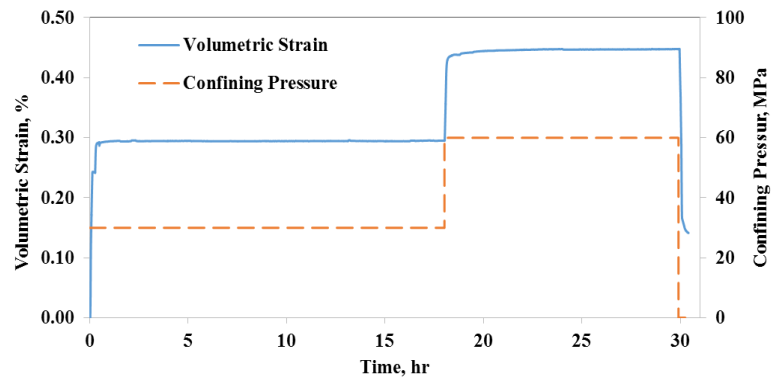
Figure 36. Volumetric strain vs. time of Barnett PAB

Table 15. Bulk modulus and strain rate of Barnett PAB

Confining pressure (MPa)	K (GPa)	Strain rate $\times 10^{10}$ (1/s)
30	12.39	0. 7
60	24.91	3.4

4.2.4. *Hydrostatic creep of Barnett PEB*

The same procedure as followed for the perpendicular sample was used for the parallel one. Figure 37 presents the results of the hydrostatic creep test on the parallel Barnett sample. It can be seen that increasing the confining pressure from the first stage to the second one resulted in lowering the compressibility, similar to other samples. By comparing the results of hydrostatic tests on parallel and perpendicular samples, it can be concluded that the instantaneous deformations of perpendicular sample are considerably larger, around three times as much as those of the parallel sample. Additionally, the creep strain rate of the perpendicular Barnett sample (PAB) is larger than that of the parallel Barnett sample (PEB). The volumetric strain of sample versus time is shown in Figure 38.
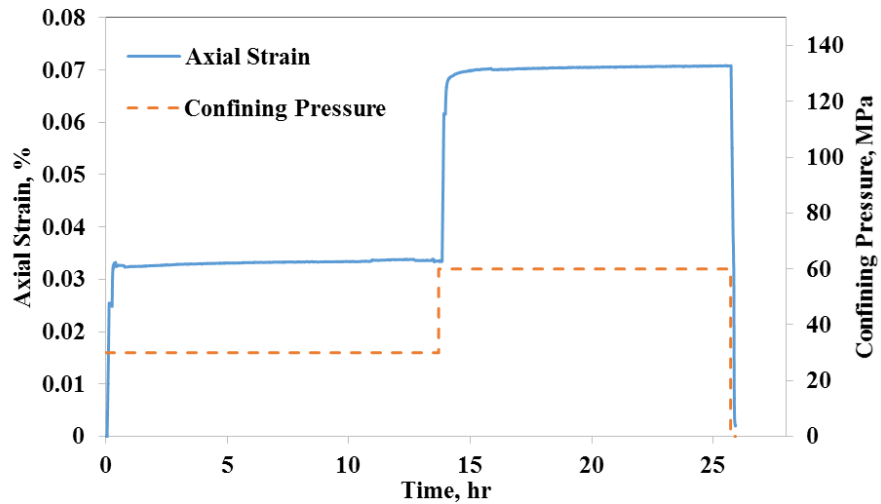
Figure 37. Hydrostatic creep of Barnett PEB

53

The bulk modulus of the sample in the second stage is twice as much as that of the first stage (Table 16). A similar behavior was observed for the perpendicular sample.

Table 16. Bulk modulus and strain rate of Barnett PEB

Confining pressure (MPa)	K (GPa)	Strain rate $\times 10^{10}$ (1/s)
30	14.72	1.6
60	27.52	1.5
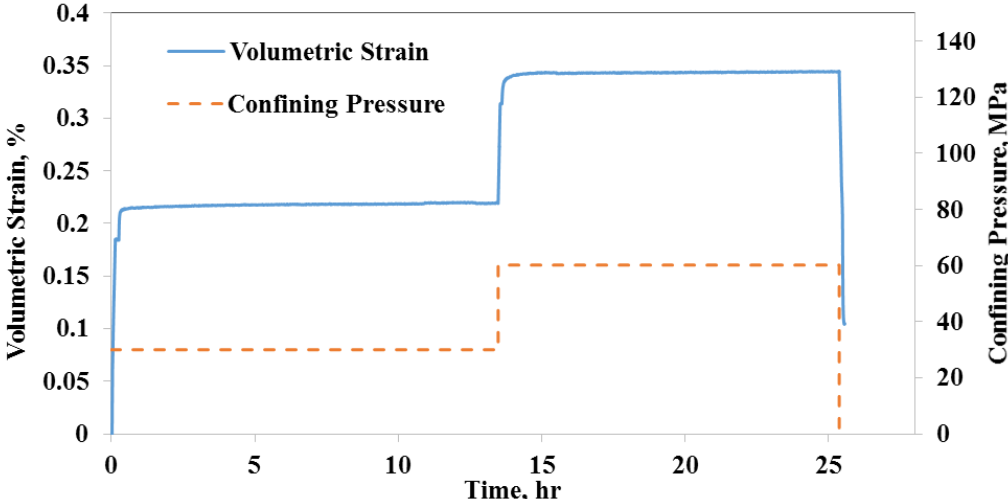
Figure 38. Volumetric strain vs. time of Barnett PEB

Comparison between the bulk modulus of Barnett and Mancos samples indicates that Barnett sample is significantly stiffer than Mancos sample and consequently the strain rate of hydrostatic creep test of Barnett samples are less than those of Mancos shale samples.

4.2.5. Deviatoric creep of Barnett PAB

Three deviatoric stresses of 18, 35 and 72 MPa were applied in three stages to the both Barnett samples so that in each stage the deviatoric stress was doubled compared to

the previous stage. These series of test were carried out under two different temperatures of 25 and 50 °C. According to Table 11, the peak stresses of the Barnett samples, perpendicular and parallel to the bedding are 116.98 MPa and 146.55 MPa, respectively. Therefore, the loading path was maintained in the elastic regime. The axial strain and volumetric strain of Barnett PAB at 25 °C are shown in Figure 39 and Figure 40. It can be seen that the instantaneous deformation of the sample in the two first stages are close but sample experienced the largest deformation in the last stage almost twice as much as its deformation in the first and second stages. This can be related to the visco-elastic behavior of the sample, recovering mainly all the deformation that it has experienced. The same behavior was observed for the deviatoric creep test under elevated temperature according to Figure 41 and Figure 42.
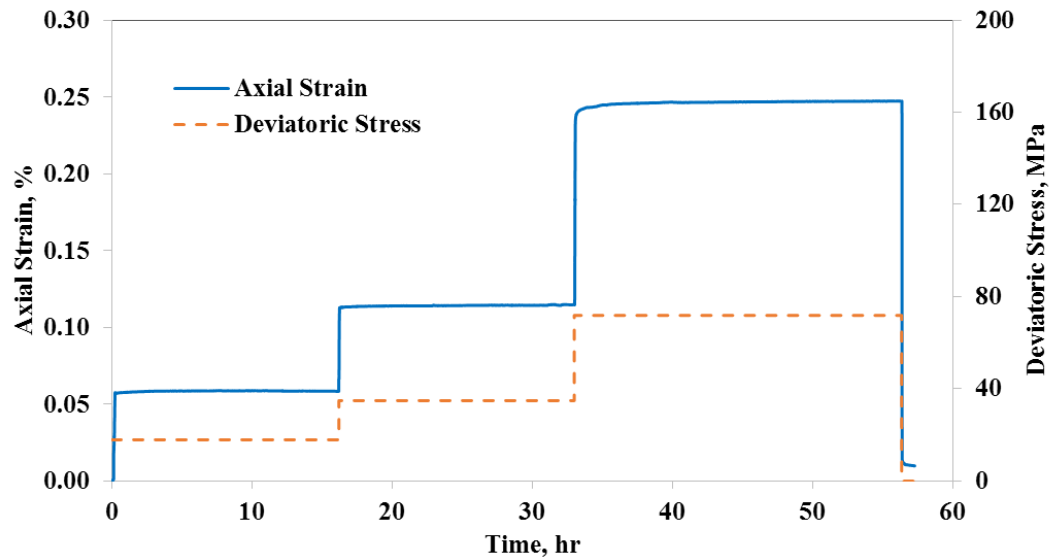
Figure 39. Axial strain vs. time of Barnett PAB at 25 °C
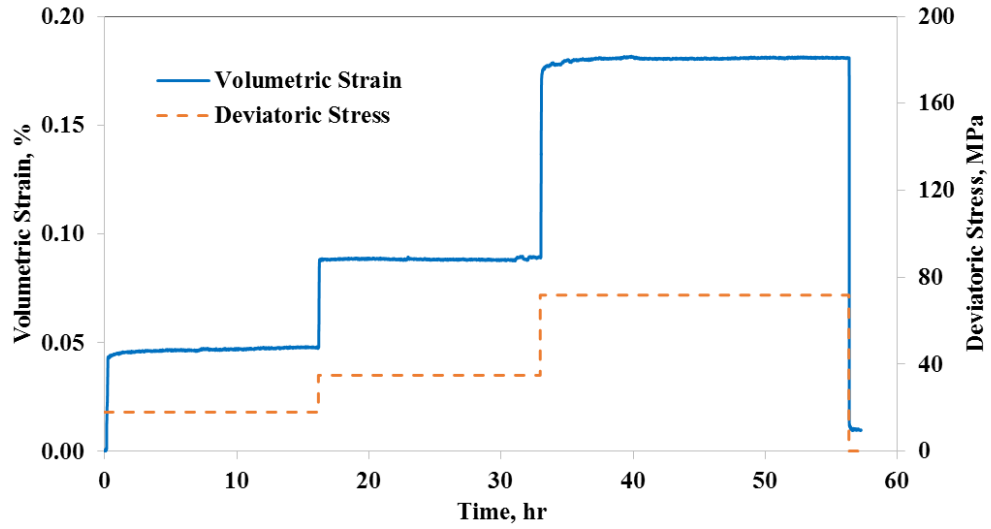
Figure 40. Volumetric strain vs. time of Barnett PAB at 25 °C
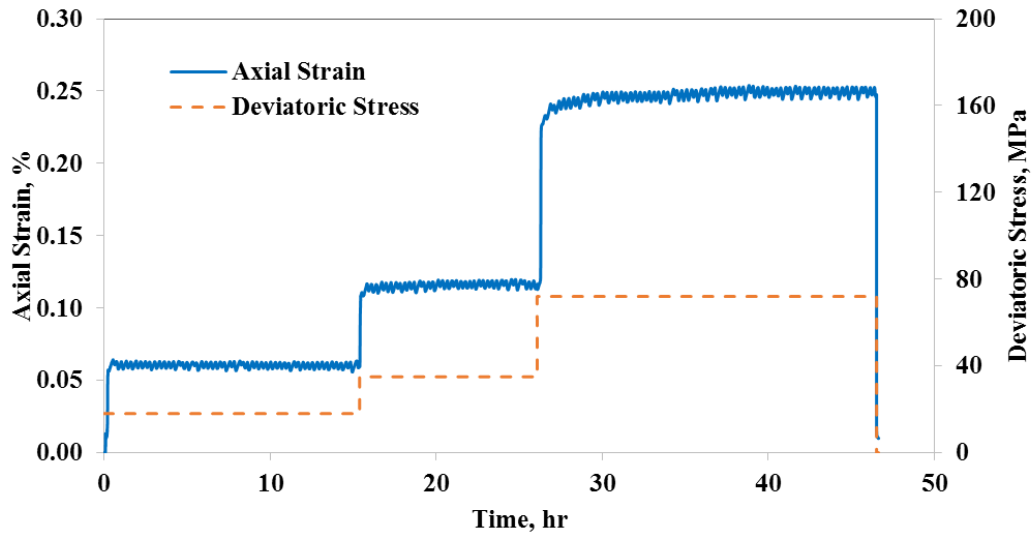
Figure 41. Axial strain vs. time of Barnett PAB at 50 °C
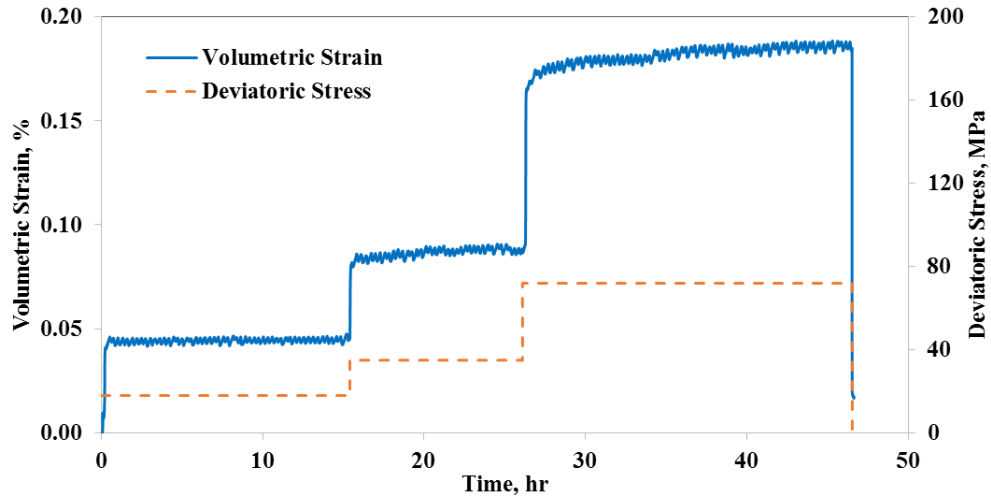
Figure 42. Volumetric strain vs. time of Barnett PAB at 50 °C

The elastic modulus of the sample is presented in Table 17. According to the table, elastic modulus was not significantly influenced by the deviatoric stress nor temperature. Temperature resulted in higher creep deformations, per Table 18. Therefore, increasing the temperature resulted in increasing the secondary creep strain rate. In addition, the influence of temperature on increasing creep strain rate is more noticeable compared to that of the deviatoric stress.

Table 17. Elastic modulus Barnett sample PAB under different deviatoric stress and temperature (GPa)

	Deviatoric stress (MPa)		
Temperature (°C)	18	35	72
25	31.6	35.94	34.86
50	30.15	35.54	34.3

The creep strain rate under 50 °C, is three times as much as that under 25 °C, while by doubling the deviatoric stress, a slight increase in the strain rate was observed.

57

Curve fitting by means of least square method was done for creep curves at 25 °C and 50 °C, per Figure 43 and Figure 44. Power low appears to be appropriate method to predict the creep behavior of Barnett PAB.

The chart contains the following power law equations:

$y = 0.1121x^{0.0154}$

$y = 0.0541x^{0.0075}$

$y = 0.0524x^{0.0064}$

Legend: 18 MPa, 25 °C; 35 MPa, 25 °C; 72 MPa, 25 °C

Axis labels: Axial Strain, % (vertical); Time, s (horizontal)
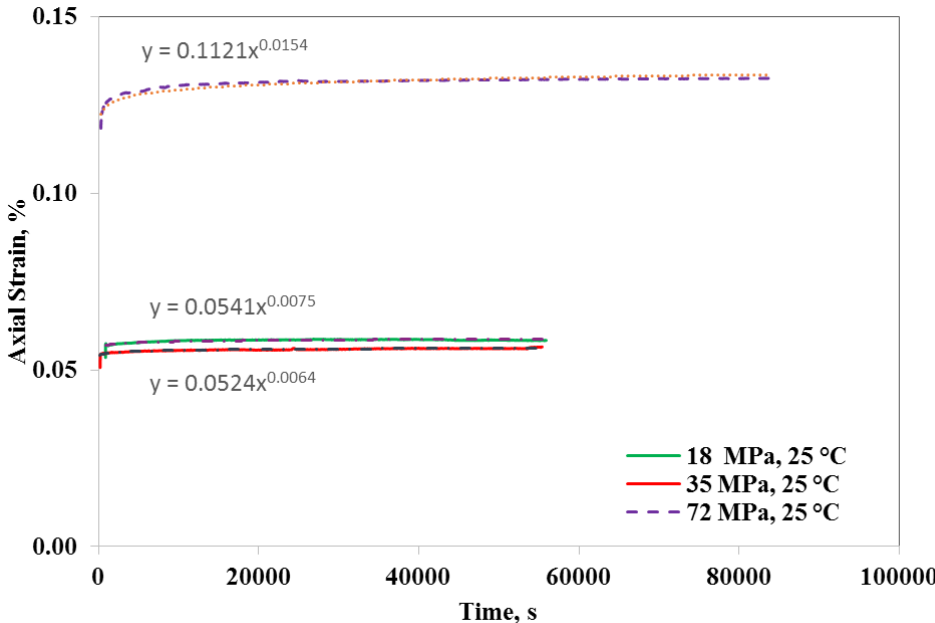
Figure 43. Power law curve fit to deviatoric creep strain vs. time for Barnett PAB at 25 °C

Table 18. Creep strain rate $\times 10^{10}$ of Barnett PAB under different deviatoric stress and temperature (1/s)

	Deviatoric stress (MPa)		
Temperature (°C)	18	35	72
25	1.02	1.5	1.9
50	1.6	4.5	5.5
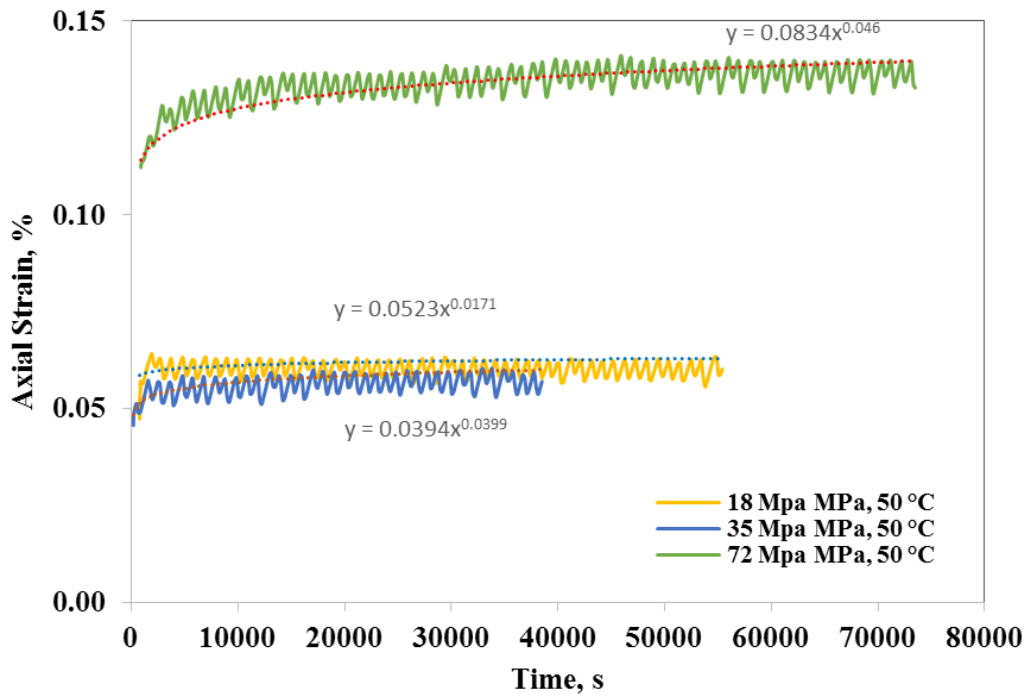
Figure 44. Power law curve fit on deviatoric creep strain vs. time for Barnett PAB at 50 °C

4.2.6. *Deviatoric creep of Barnett PEB*

Similar to the PAB sample, the parallel Barnett sample was subjected to three stages of deviatoric stresses of 18, 35 and 72 MPa, but at three different temperatures of 25, 50 and 70 °C. The results of the first series of deviatoric creep test at room temperature are shown in Figure 45. Two other series of creep tests at the elevated temperature followed the same trends as the one under room temperature and similar to the PAB sample, the creep behavior of the Barnett PEB is visco-elastic. All the stages at 50 and 70 °C are presented in Figure 46 and Figure 47. The creep deformation of this sample was generally negligible, except under deviatoric stress of 72 MPa as the ratio of creep strain to instantaneous strain was close to zero as well as the strain rate of steady state stage.

Interestingly, there were no significant changes in strain measurements due to temperature.
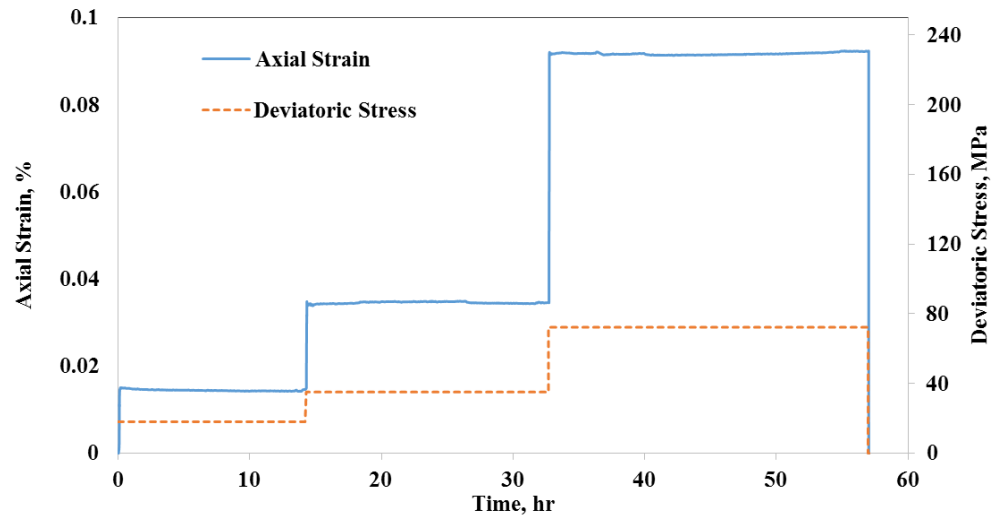
Figure 45. Axial strain vs. time of Barnett sample PEB at 25 °C
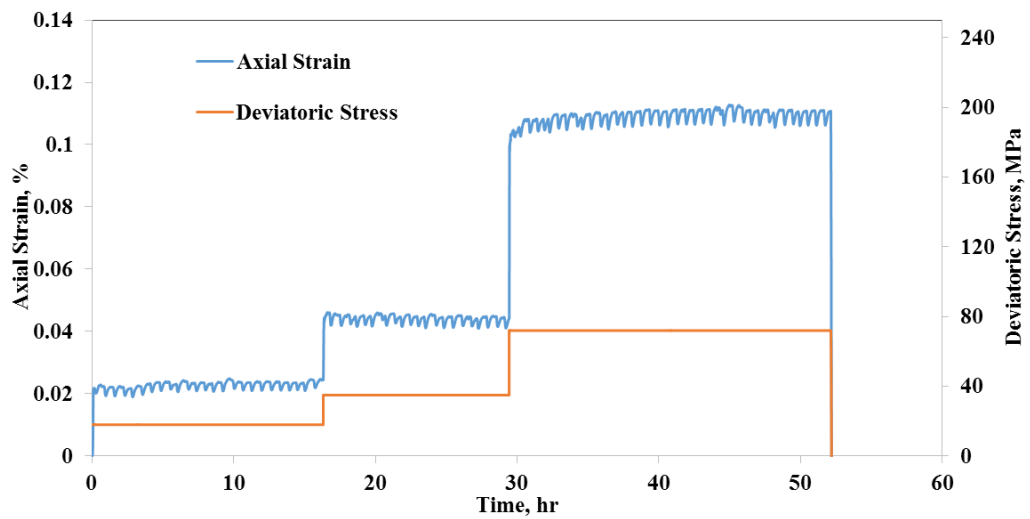
Figure 46. Axial strain vs. time of Barnett sample PEB at 50 °C
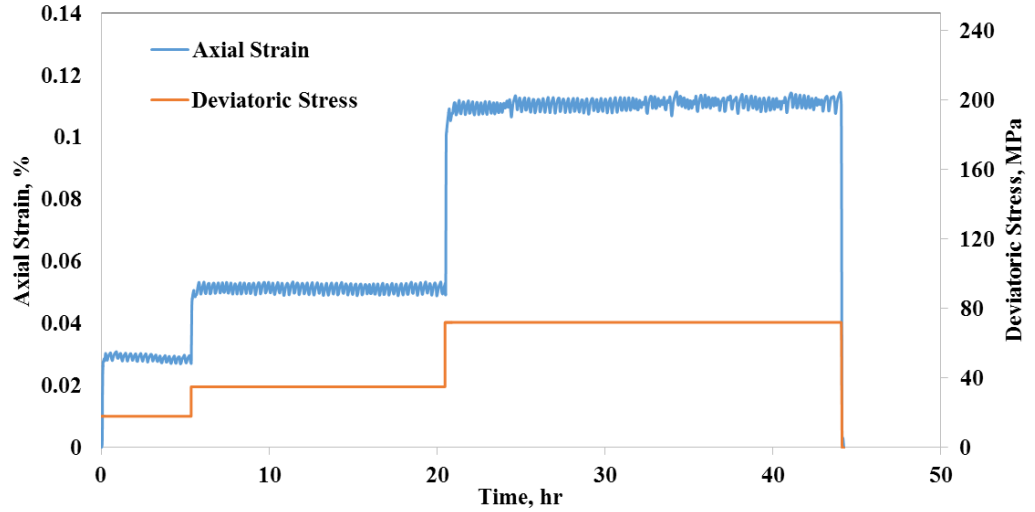
Figure 47. Axial strain vs. time of Barnett sample PEB at 70 °C

Table 19. Creep strain rate $\times 10^{10}$ of Barnett PEB under different deviatoric stress and temperature (1/s)

Temperature (°C)	Deviatoric stress (MPa)		
	18	35	72
25	<0.01	<0.01	1.5
50	<0.01	<0.01	1.5
70	<0.01	<0.01	1.6

By comparing the results of two Barnett samples, it can be concluded that the deformation of the parallel sample is much lower than that of perpendicular one. On the other hand, the stiffness of the parallel sample is larger. This can be confirmed by comparing between the elastic modulus of the two samples under different conditions of deviatoric stress and temperature (Table 17 and Table 20).

61

Table 20. Elastic modulus of the Barnett sample PEB under different deviatoric stress and temperature

Temperature (°C)	Deviatoric stress (MPa)		
	18	35	72
25	63.36	76.9	62.17
50	65.43	74.33	58.45
70	59.18	68	58

The elastic modulus of the sample by increasing the deviatoric stress from 18 to 35 MPa increased but further increase in deviatoric stress resulted in a reduction of the elastic modulus. This behavior could be due to the crack closure at the beginning stages or stress hardening. However, increasing the deviatoric stress created new cracks, thus lowering elastic modulus.

4.3. Pierre shale

4.3.1. Sample description

Two Pierre samples, parallel and perpendicular to the bedding of the same size as Barnett and Mancos were used to study the influence of anisotropy under hydrostatic and deviatoric conditions (Figure 48 and Figure 49). Correspondingly, these two series of tests were repeated under two temperatures, 25 and 50° C.

Figure 48. The Pierre Shale PAB Specimen before Testing
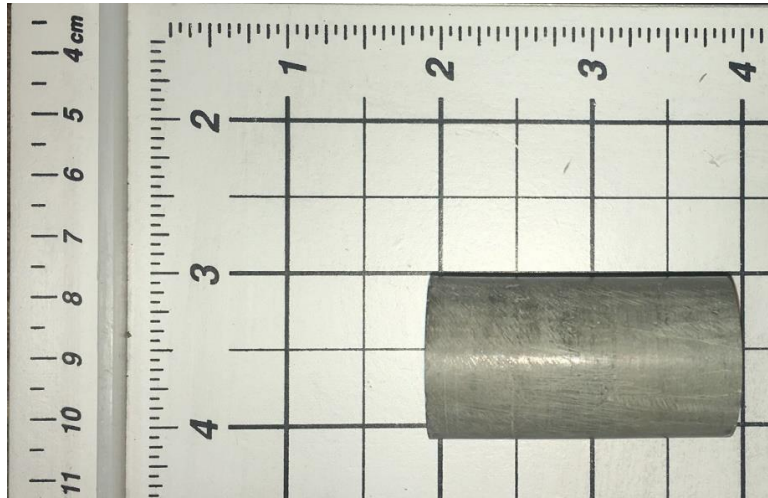
Figure 49. The Pierre Shale PEB Specimen before Testing

The two stages of the hydrostatic creep tests on Pierre shale were carried out under two confining pressures of 10 MPa and 30 MPa. Deviatoric creep tests on Pierre shale were performed with confining pressure of 10 MPa. Deviatoric stresses of 5.2 MPa and 11.4 MPa were applied to the both samples as well as 22 Mpa to Pierre PEB.

Table 21. Mineralogy of Pierre shale

Quartz	Calcite	Dolomite	Illite	Smectite	Kaolinite
19.46	0	1.6	48.78	8.75	0.22
Chlorite	Pyrite	Orthoclase	Oglioclase	Mixed Clay	Albite
2.29	0	7.5	3.27	0	2.49
Anhydrite	Siderite	Apatite	Aragonite		
0.39	4	1.26	0		

4.3.2. Hydrostatic creep of Pierre PAB

Results of the hydrostatic creep test is shown in Figure 50. As can be seen, increasing the confining stress has a great influence on the creep deformation and creep

strain rate. The maximum strain was observed in this series of test was 1.6 % under 30 MPa confining pressure.
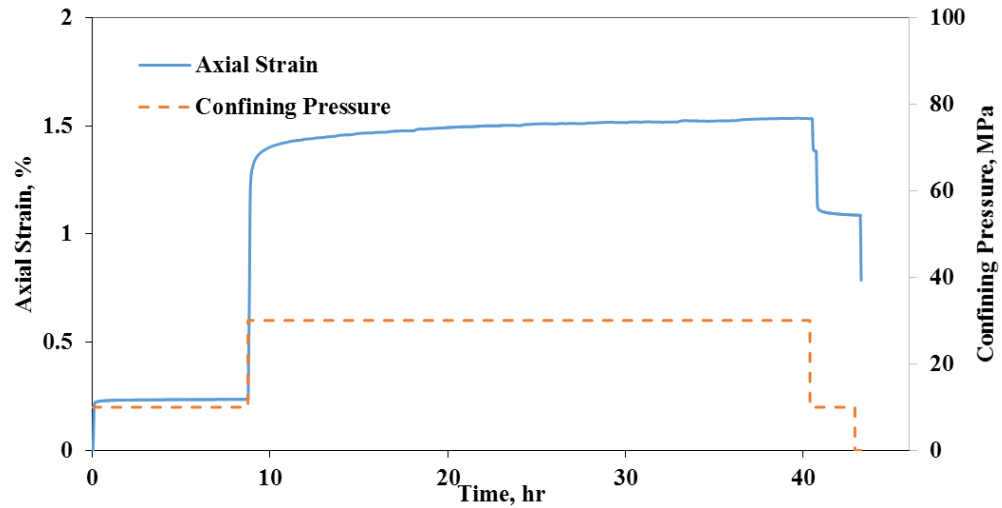
Figure 50. Hydrostatic creep of Pierre PAB

Figure 51 shows the volumetric strain of sample. According to this figure and Table 22, it can be concluded that the compressibility of sample increased in the second stage, unlike Barnett and Mancos shale samples. Based on the result, the creep behavior of this rock under hydrostatic condition is more visco-elasto-plastic.

Table 22. Bulk modulus and strain rate of Pierre PAB

Confining pressure (MPa)	K (GPa)	Strain rate $\times 10^9$ (1/s)
10	3.7	1.11
30	1.88	6.39

Figure 51. Volumetric strain vs. time of Pierre PAB

4.3.3. *Hydrostatic creep of Pierre PEB*

The similar behavior was observed for the parallel sample according to Figure 52: more deformation was recorded under 30 MPa confining pressure compared to 10 MPa and more than 50 % of deformation was immediately recovered after unloading.
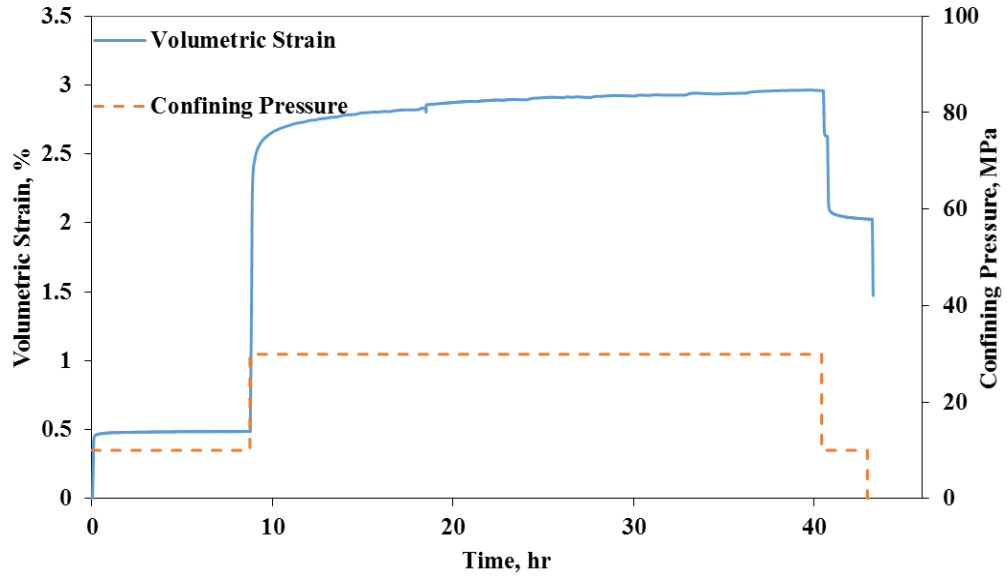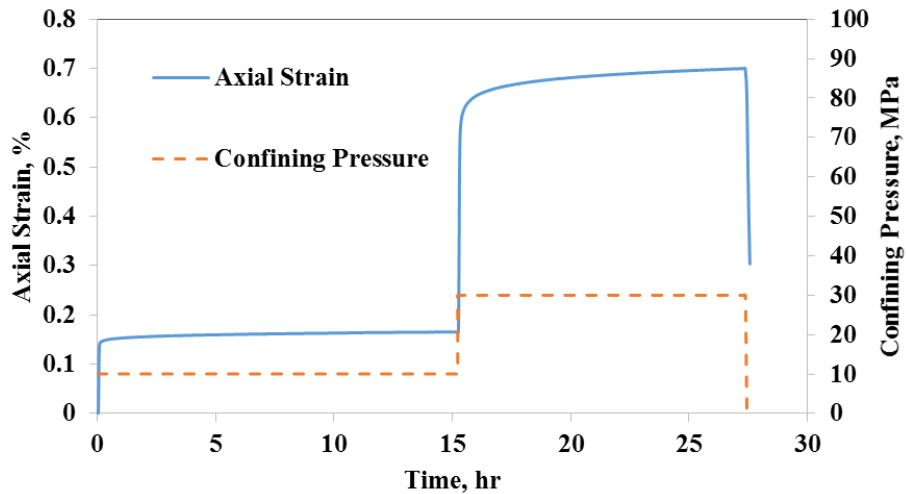

Figure 52. Hydrostatic creep of Pierre PEB

Figure 53 shows the volumetric deformation of Pierre sample PEB and

Table **23** represents the bulk modulus of the sample. It can be concluded that the

parallel sample is more compressible.
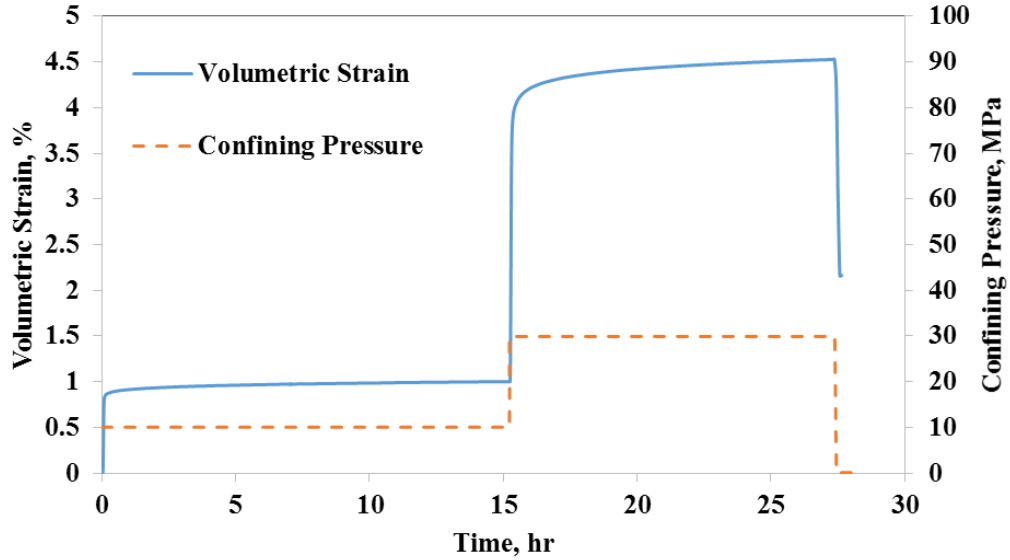
Figure 53. Volumetric strain vs. time of Pierre PEB

Table 23. Bulk modulus and strain rate of Pierre PEB

Confining pressure (MPa)	K (GPa)	Strain rate $\times 10^9$ (1/s)
10	1.14	1.67
30	0.67	6.94

4.3.4. *Deviatoric creep of Pierre PAB*

Results of the deviatoric creep tests on Pierre shale sample at 25 and 50°C are

shown in Figure 54 and Figure 55, respectively. The axial strain vs. time diagram for 11.4

MPa deviatoric stress and 50 °C showed the longest transient creep stage and the steady-

state stage started after 10 hours. It is worth mentioning that the deformation due to

deviatoric stress was mostly recovered. Power law was fitted to the deviatoric creep

curves under different stresses and temperatures, per Figure 56.
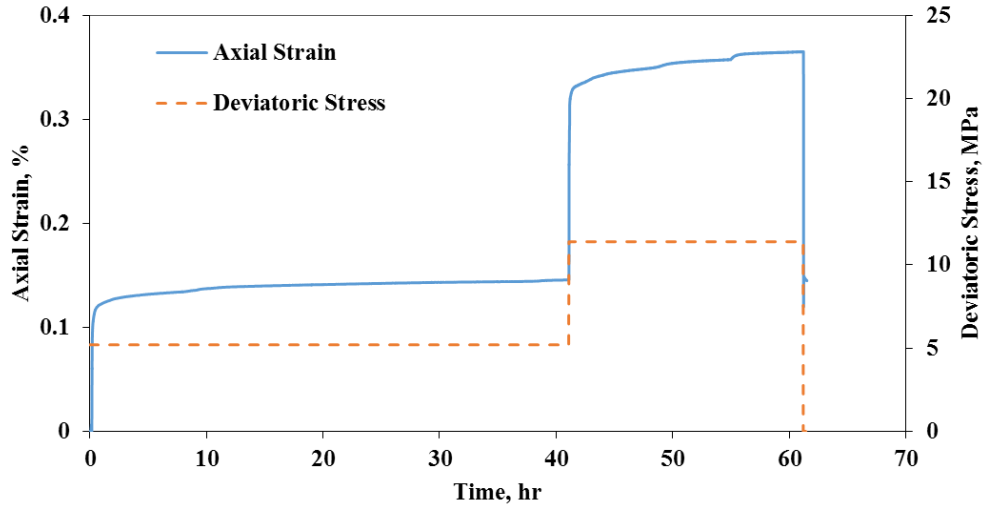
Figure 54. Deviatoric creep of Pierre PAB at 25 °C

Table 24. Elastic modulus of Pierre PAB under different deviatoric stresses and temperatures (GPa)

Temperature (°C)	Deviatoric stress (MPa)	
	5.2	11.4
25	4.05	4.86
50	5.9	4.7

Figure 55. Deviatoric creep of Pierre PAB at 50 °C

67
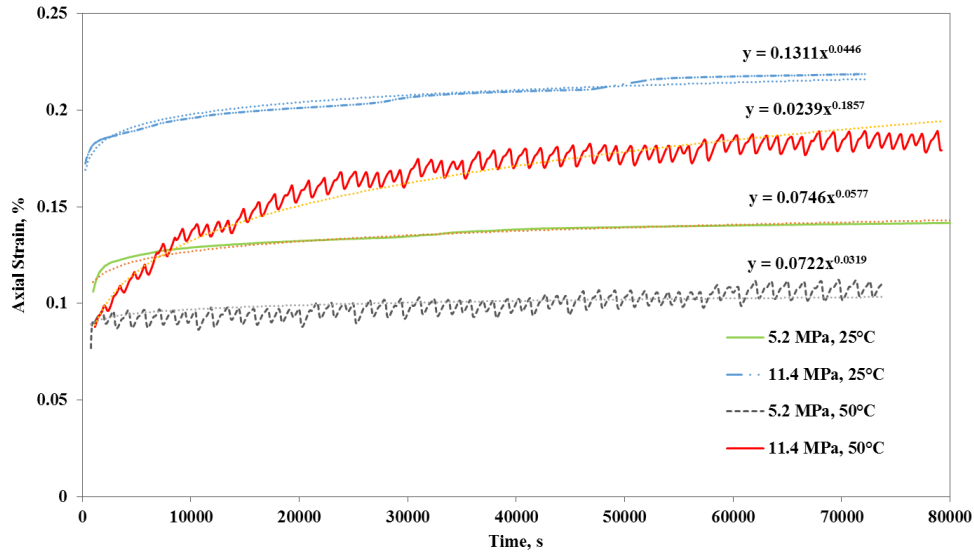
Figure 56. Curve fit on Pierre PAB at 25 and 50 °C

Table 25 represents the strain rates of deviatoric creep tests on Pierre sample PAB. The highest strain rate of the steady-state stage was recorded when the sample was subjected to 11.4 MPa deviatoric stress in 50 °C.

Table 25. Creep strain rate $\times 10^{10}$ of Pierre PAB under different deviatoric stresses and temperatures (1/s)

Temperature (°C)	Deviatoric stress (MPa)	
	5.2	11.4
25	8.3	35
50	25	36

4.3.5. *Deviatoric creep of Pierre PEB*

The same procedure was followed for the parallel sample, but this sample went through one more stage (under deviatoric stress of 22 MPa). The

68

results of deviatoric creep tests on the sample are presented in Figure 57 to Figure 59 and elastic modulus and steady state creep rate of sample in each stage are shown in Table 26 and Table 27. Power law was fitted to the deviatoric creep curves under different stresses and temperatures (Figure 59).
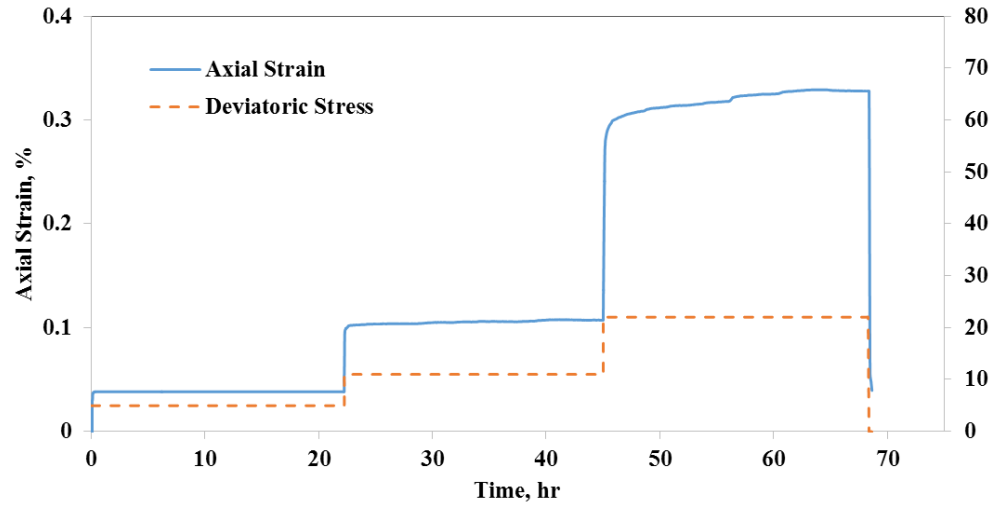
Figure 57. Deviatoric creep on Pierre PEB at 25° C
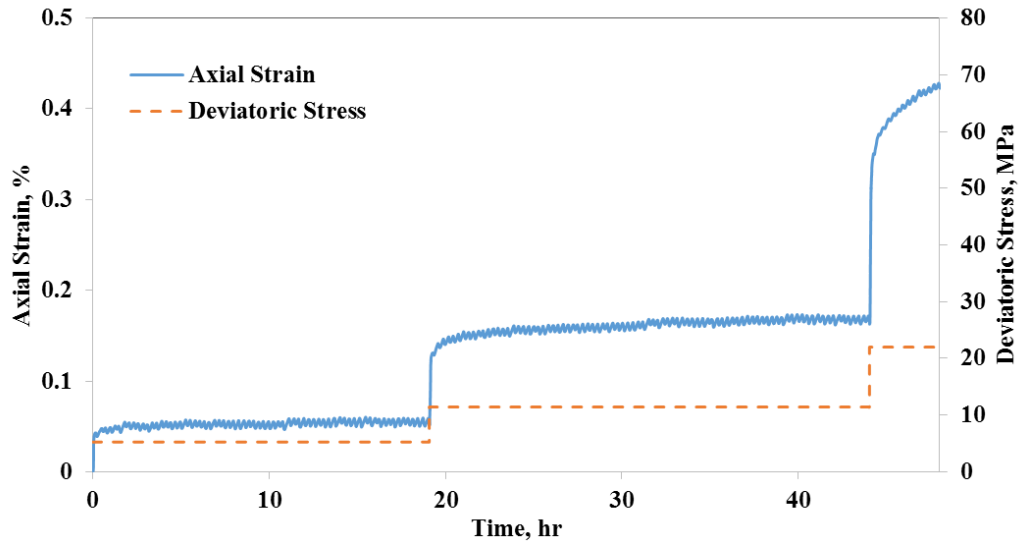
Figure 58. Deviatoric creep on Pierre PEB at 50° C
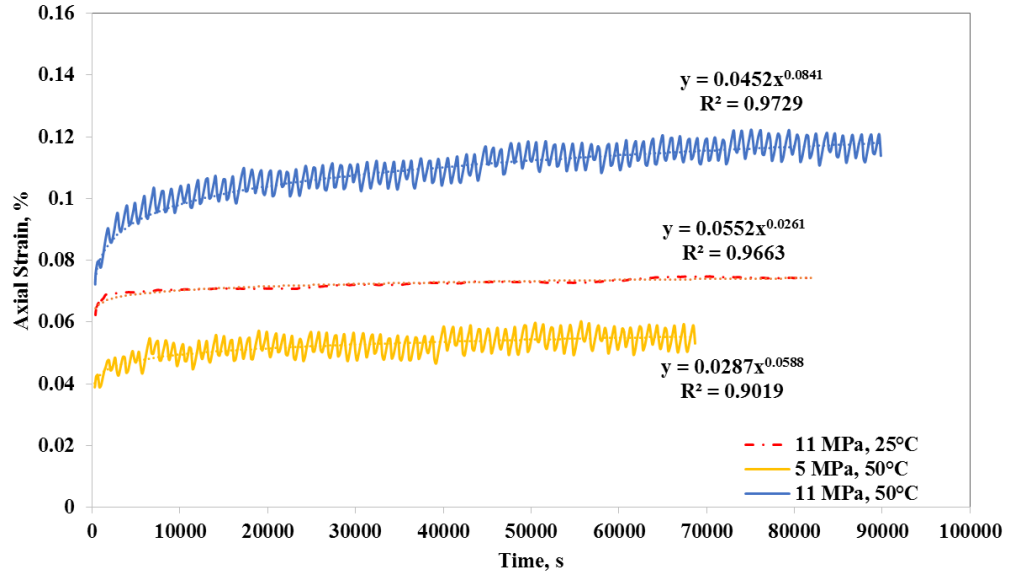
Figure 59. Curve fit on Pierre PEB at 25 and 50 °C

The results indicate that increasing the temperature significantly increased the strain rate, in accordance to the results of deviatoric creep tests on perpendicular sample as presented in previous section.

Table 26. Elastic modulus of Pierre PEB under different deviatoric stresses and temperatures (GPa)

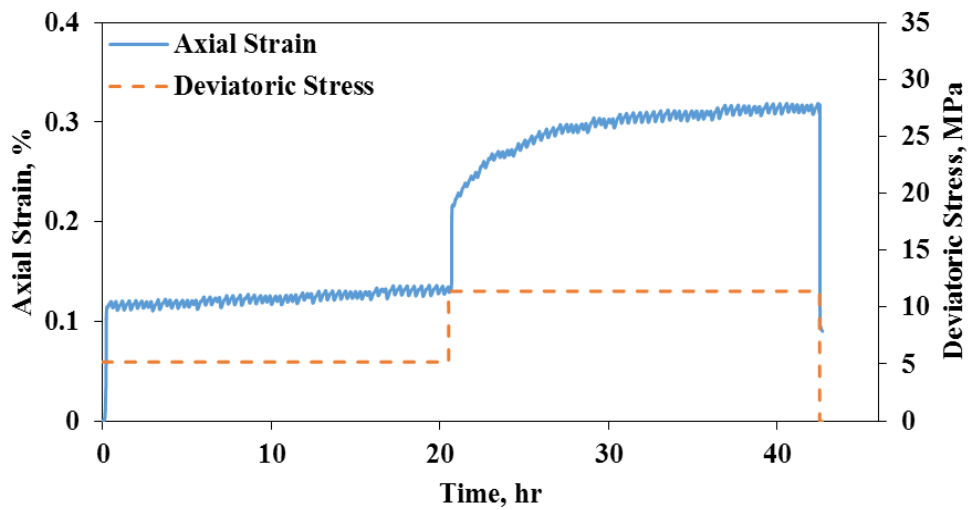| Temperature (°C)	Deviatoric stress (MPa)		
	5.2	11.4	22
25	10.37	9.29	6.67
50	13.09	9.42	7.86

Table 27. Creep strain rate $\times 10^{10}$ of Pierre PEB at different deviatoric stresses and temperatures (1/s)

Temperature (°C)	Deviatoric stress (MPa)		
	5.2	11.4	22
25	<0.1	6.08	32
50	7.69	19.03	-

70

The creep strain rate of parallel sample is smaller than that of perpendicular one while its stiffness is higher than that of perpendicular one.

4.4. Haynesville shale

4.4.1. *Haynesville shale formation*

The location of Haynesville formation is southwestern Arkansas, northwest Louisiana, and East Texas. The area of this formation is about 9000 square mile and the thickness of it is about 300 to 400 feet at the depth of 10500 to 13000. The sandstone of Cotton Valley Group and limestone of Smackover Formation overlie and underlie Haynesville formation, respectively (Wikipedia, 2017).

This formation contains an enormous amount of natural gas which was quite exploitable economically prior to 2008. After 2008, new technologies, hydraulic fracturing and directional drilling, have facilitated to exploit this reservoir with reasonable cost (Wikipedia, 2017).

Similar to the Barnett samples, Haynesville samples were chosen from two wells that described well in the extensive study conducted by Ghassemi, A and Suarez-Rivera, 2012. N-dimensional heterogeneous rock analysis (HRA) was performed for this type of shale rock as well. The authors break all the available samples down into seven groups: dark blue, light blue, yellow, red, brown, purple and green. Two samples, parallel and perpendicular to the bedding, were chosen from the light blue group that was recognized as the best quality base on HRA.

4.4.2. Sample description

The size of two samples of Haynesville was identical to the other samples in this study (2.54 cm (1 inch) in diameter and 5.08 (2 inch) long. Figure 60 shows the petrologic analysis on the class of interest in the current study. Different properties of this shale rock including: petrophysical, geochemical, geochemical as well as XRD mineralogy are presented as follows:
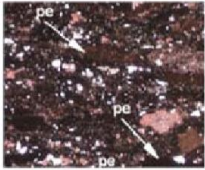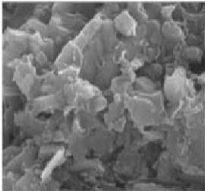
Figure 60. Petrologic properties of light blue class of Haynesville shale rock (Ghassemi and Suarez-Rivera, 2012)

Table 28. Average Haynesville petrophysical properties (Ghassemi and Suarez-Rivera, 2012)

Bulk density (g/cc)	Grain density (g/cc)	Dry Gas density (g/cc)	Effective porosity (%BV)	Water saturation (%PV)	Gas saturation (%PV)
2.469	2.648	2.669	7.82	4.89	86.7
Mobile oil saturation (%PV)	Gas filled porosity (%BV)	Bound hydrocarbon saturation (%BV)	Clay bound water (%BV)	Pressure decay permeability (nD)	No of samples
8.38	6.76	0.456	4.92	509	3

Table 29. Average Haynesville geomechanical properties (static) (Ghassemi and Suarez-Rivera, 2012)

Bulk density (g/cc)	Effective confining stress (MPa)	Peak strength (V) (MPa)	Peak strength (H) (MPa)	Young's modulus (V) (GPa)	Young's modulus (H) (GPa)
2.49	16.34	124.43	130	17.72	29.44

No of samples	Poisson's ratio (V)	Poisson's ratio (H)
10	0.176	0.217

Table 30. Average Haynesville geomechanical properties (dynamic) (Ghassemi and Suarez-Rivera, 2012)

No of samples	Mean stress (MPa)	P-wave velocity (V) (m/s)	P-wave velocity (H) (m/s)	S-wave velocity (V) (m/s)	S-wave velocity (H) (m/s)
4	22.64	3662.48	4702.45	2289	2888
Bulk density (g/cc)	Young's modulus (V) (GPa)	Young's modulus (H) (GPa)	Poisson's ratio (V)	Poisson's ratio (H)	No of samples
2.5	31.1	50.3	0.178	0.195	3

Table 31. Average geochemical properties of Haynesville (Ghassemi and Suarez-Rivera, 2012)

No. of samples	Total organic content (% Wt)
4	2.15

Table 32. Haynesville XRD mineralogy (Ghassemi and Suarez-Rivera, 2012)

No of samples	Quartz	Calcite	Total clay	Other
15	25.42	23.44	33.45	17.69
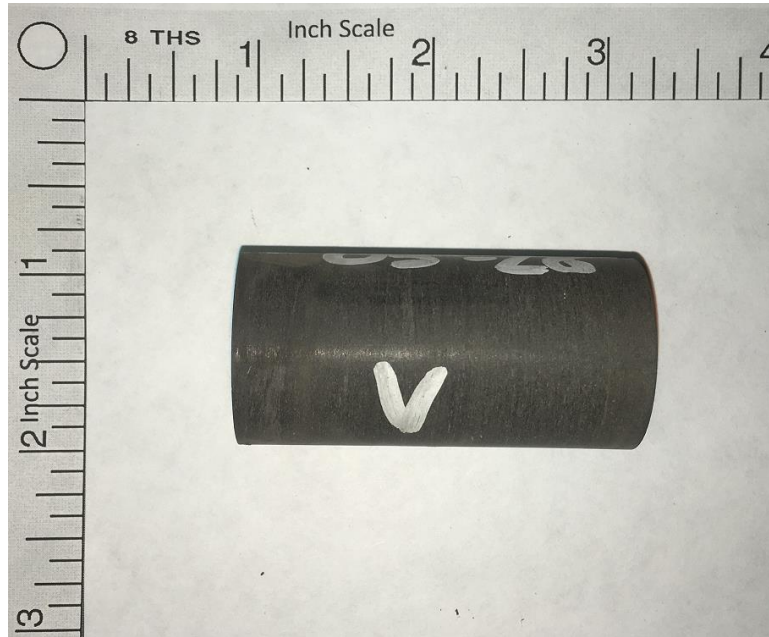
Figure 61. Haynesville sample PAB
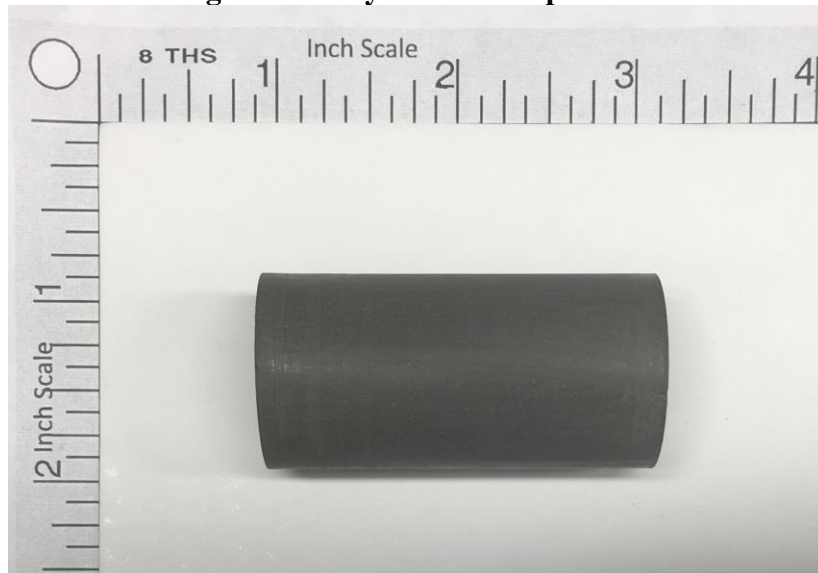
Figure 62. Haynesville sample PEB

4.4.3. Hydrostatic creep of Haynesville PAB

The result of hydrostatic creep test on Haynesville perpendicular is presented in the following figure. The sample experienced more instantaneous deformation in the first stage compared to the second one. This behavior could be associated to micro-crack closure in the first stage resulting in less deformation in the second stage. However, the creep strain rate of the second stage is as twice as that of the first stage according to Table 33.
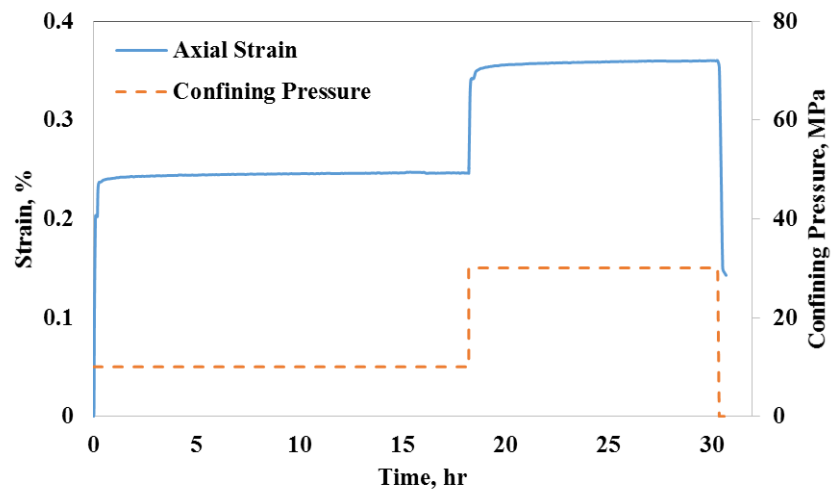
Figure 63. Hydrostatic creep of Haynesville PAB
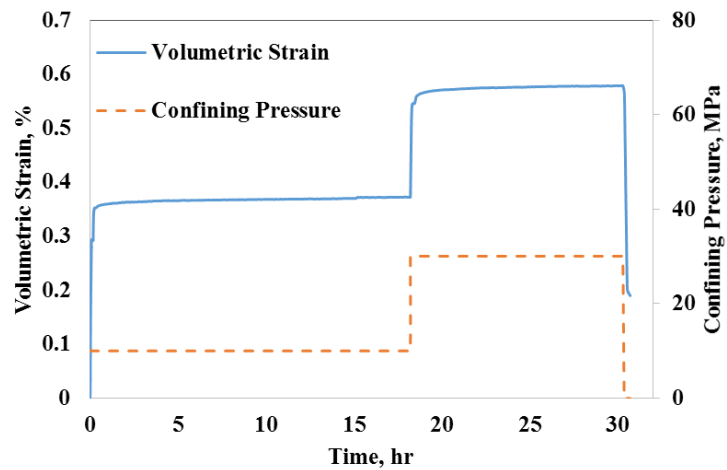
Figure 64. Volumetric strain vs. time of Haynesville PAB

75

Table 33. Bulk modulus and strain rate of Haynesville sample PAB

Confining pressure (MPa)	K (GPa)	Strain rate $\times 10^{10}$ (1/s)
30	9.38	3.71
60	18.75	7.15

4.4.4. *Hydrostatic creep of Haynesville PEB*

The instantaneous deformation of the second stage was more while having less creep strain rate (Figure 65). As expected, the volumetric deformation of rock under two confining pressures of 30 and 60 MPa was significantly more than axial strain due to the higher compressibility of rock in the parallel direction to the bedding (Figure 66). The significant percent of axial deformation was recovered after unloading while only 50% of volumetric strain was recovered instantaneously. The volumetric strain of parallel samples was significantly less than that of perpendicular sample.
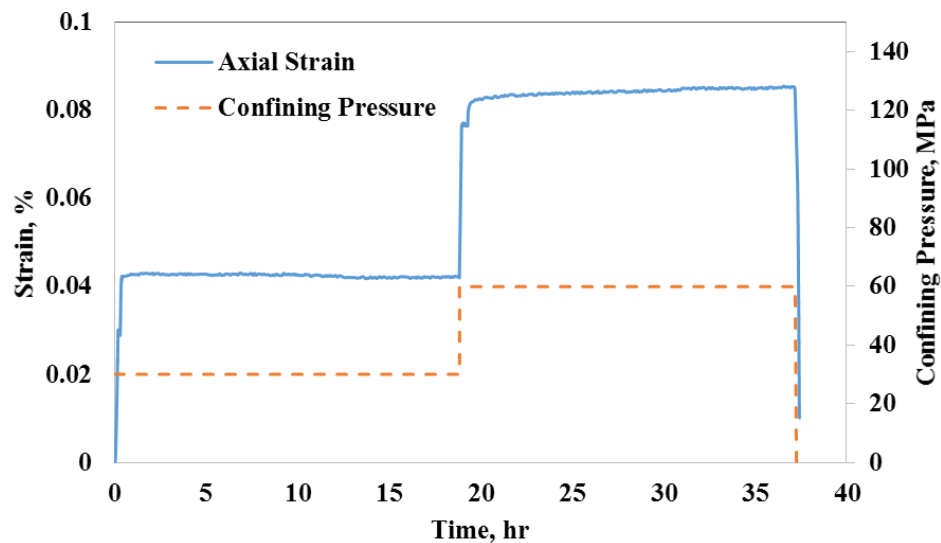
Figure 65. Hydrostatic creep of Haynesville PEB

76

Table 34. Bulk modulus and strain rate of Haynesville PEB

Confining pressure (MPa)	K (GPa)	Strain rate $\times 10^{10}$ (1/s)
30	4.47	1.48
60	13.04	4.22
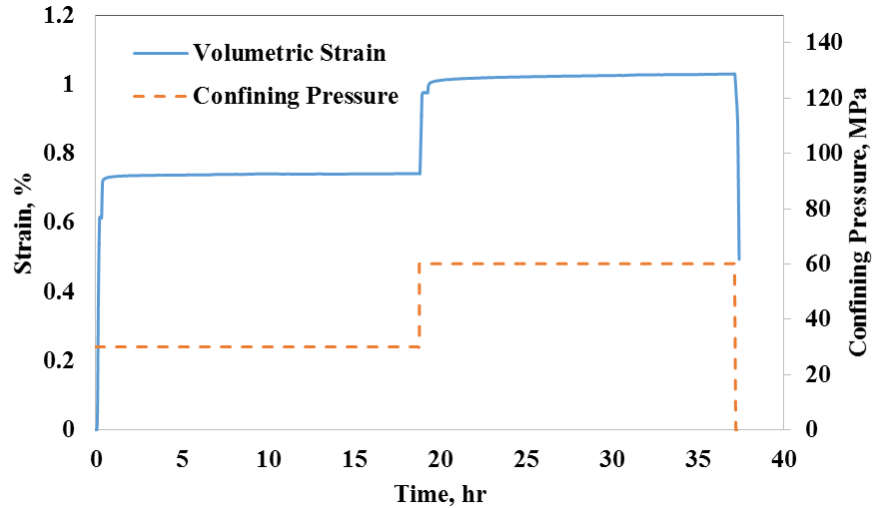
Figure 66. Volumetric strain vs. time of Haynesville PEB

4.4.5. *Deviatoric creep of Haynesville PAB*

The same procedure for Barnett shale rock was followed for Haynesville samples. It means that three stages of deviatoric stresses of 18, 35 and 72 MPa were applied. The deviatoric stresses of all three stages were lower than the peak strength of Haynesville rocks .The result of creep test under 25°C is presented in Figure 67. Similar behavior to Barnett sample was observed: the instantaneous deformation of third stage was almost double as much as those of the two first stages. The total deformation of sample due to deviatoric stress was recovered after unloading, therefore the behavior of this sample is viscoelastic. Curve fitting was done, per Figure 68.

77

Figure 67. Deviatoric creep of Haynesville PAB at 25 °C
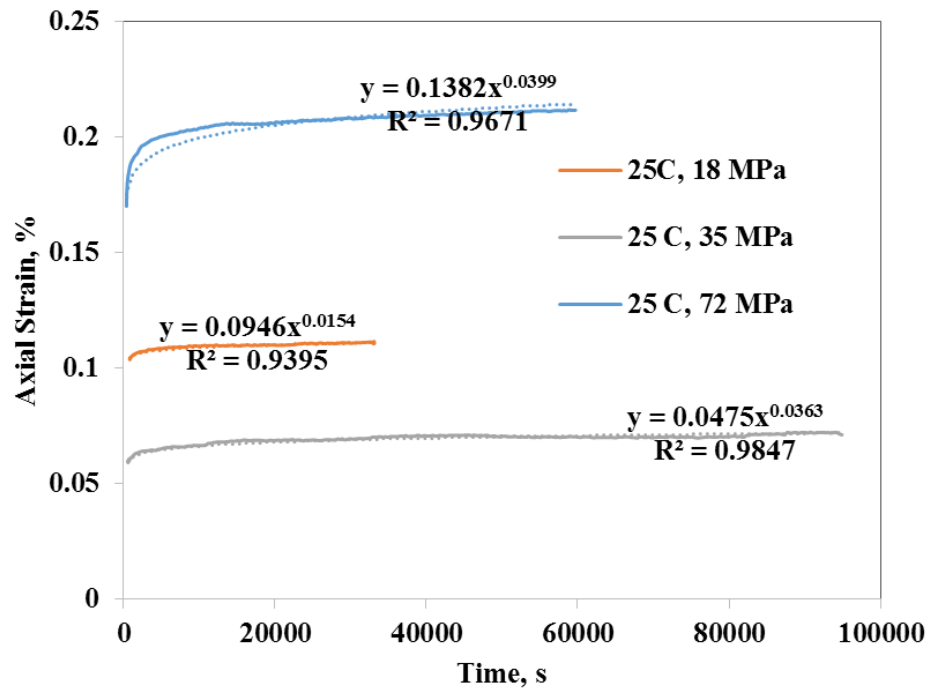
Figure 68. Power law curve fit of Haynesville PAB at 25 °C

The result of creep test under 50℃ is shown in Figure 69, similar trend as that under 25 ℃ was observed. The deformation of rock was recorded for

78

sufficient time after unloading so it is feasible to determine the creep behavior of this sample with certainty. As ther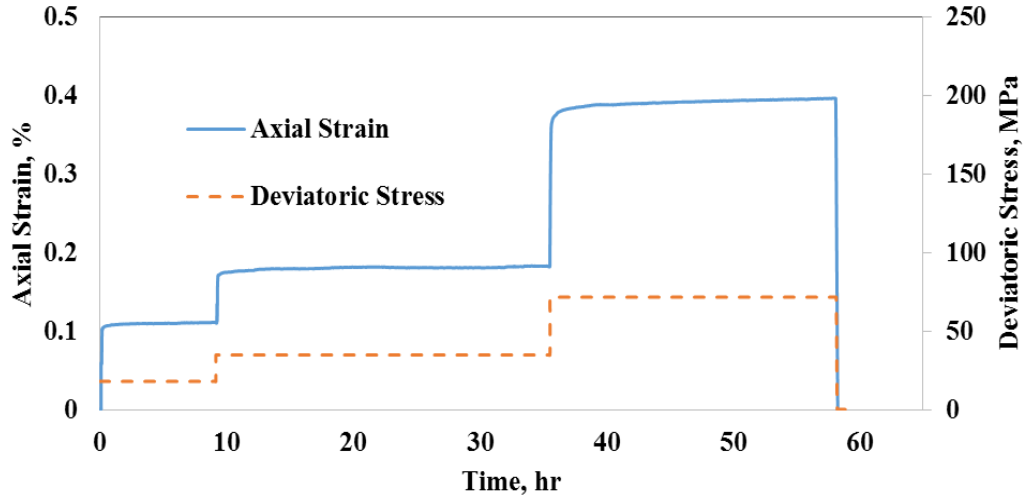e was 15% permanent deformation (plastic deformation), thus the creep behavior of Haynesville PAB under high temperature is visco-elastoplastic.

Another significant aspect of this series of tests was related to using both strain gauge and LVDT to validate the strain measurement of creep test under elevated temperature. The comparison between strain gauge and LVDT measurement was done in Figure 70, the closeness between two methods of strain measurement is obvious.
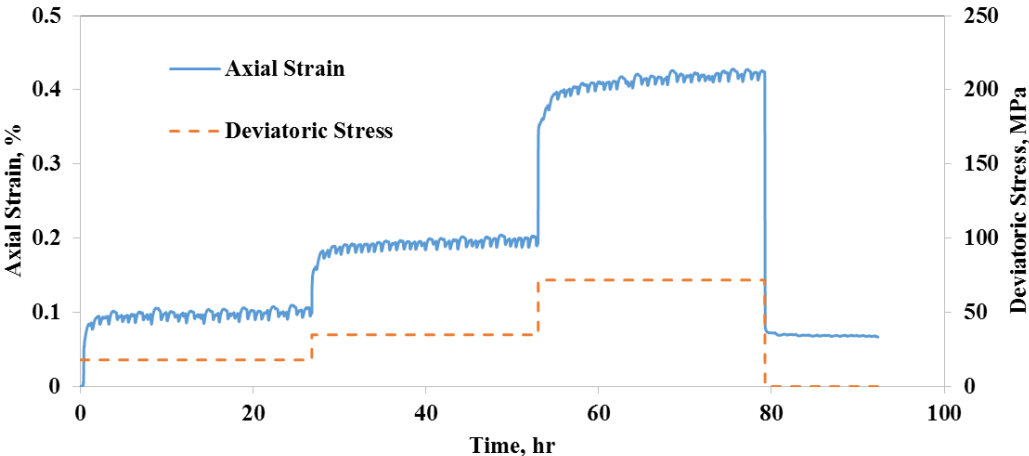
Figure 69. Deviatoric creep on the perpendicular Haynesville PAB at 50 °C

The elastic modulus of instantaneous parts of deformation and the creep strain rate of steady state parts of creep curves are shown in Table 35 and Table 36, respectively. The elastic modulus did not change significantly throughout the test. The creep stain rate increased as a result of elevated temperature, almost double. Power law was fitted to creep strain according to Figure 71.

79
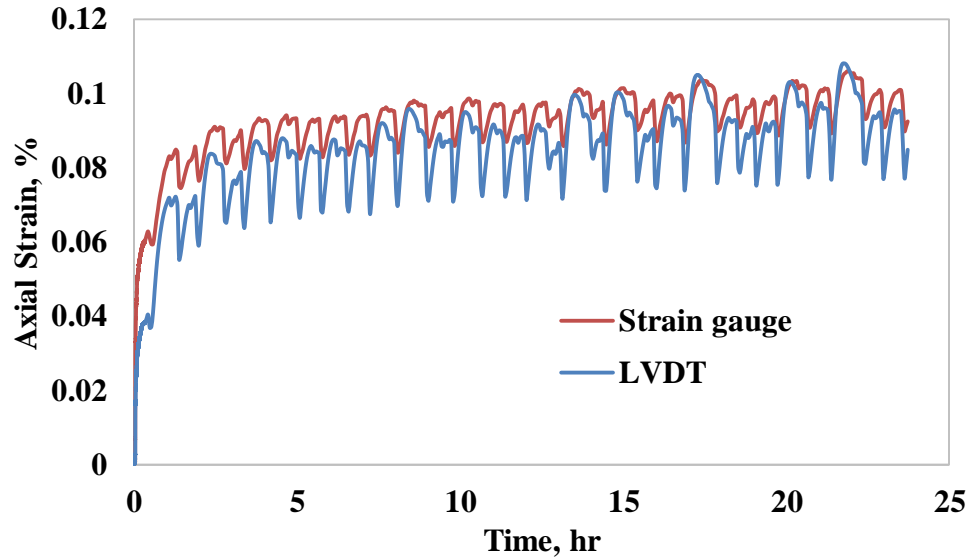
Figure 70. Comparison between LVDT and strain gauge measurements (deviatoric stress=18 MPa and temperature=50°C)

Table 35. Elastic modulus of the perpendicular Haynesville PAB under different deviatoric stress and temperature (GPa)

Temperature (°C)	Deviatoric stress (MPa)		
	18	35	72
25	26	31.5	20
50	31.1	22.7	21

Table 36. Creep strain rate $\times 10^{10}$ of the perpendicular Haynesville PAB under different deviatoric stress and temperature (1/s)

Temperature (°C)	Deviatoric stress (MPa)		
	18	35	72
25	6.63	1.79	11.6
50	12.3	10.7	16.7
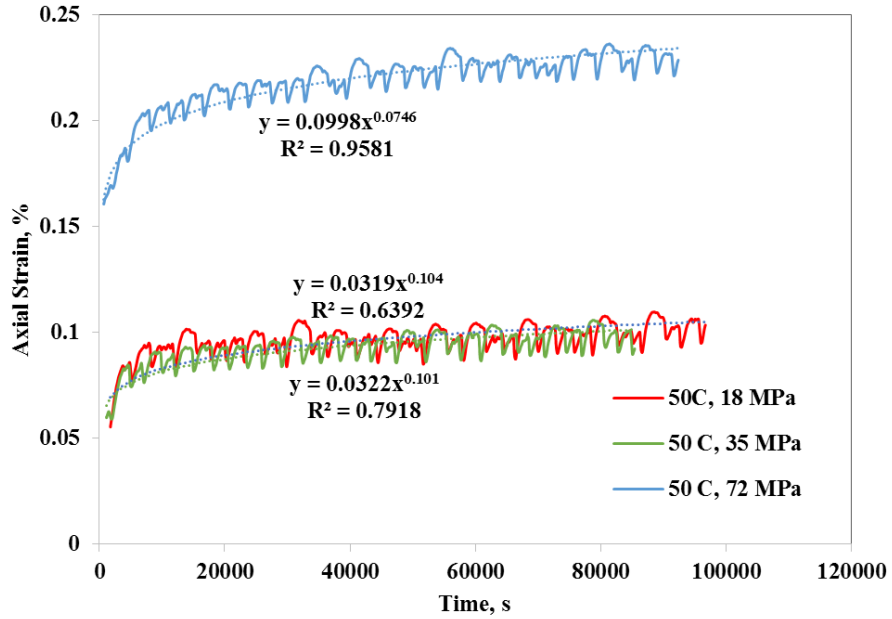
Figure 71. Power law curve fit on axial strain vs. time of Haynesville PAB at 50 °C

4.4.6. *Deviatoric creep of Haynesville PEB*

The result of two series of creep tests on Hayneville sample cored parallel to the bedding are exhibited in Figure 72 and Figure 73 and power law was fitted to creep strain according to Figure 74.
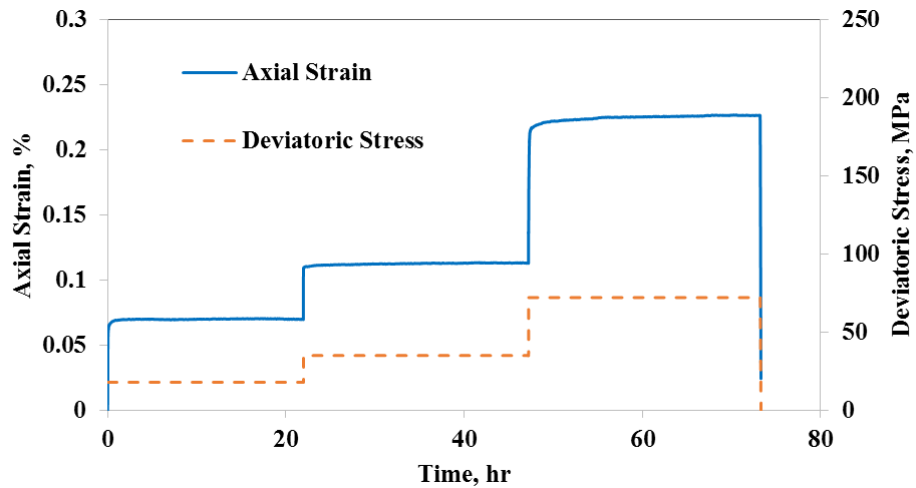
Figure 72. Deviatoric creep of Haynesville PEB at 25 °C
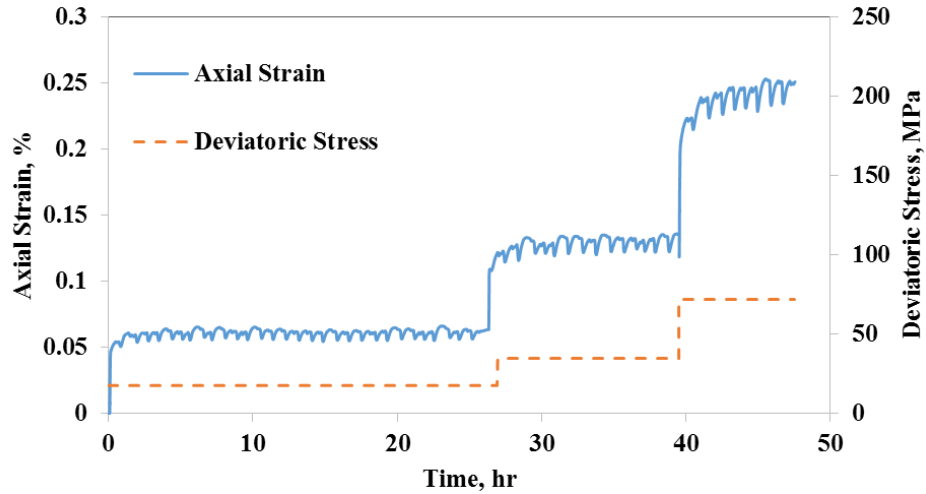
Figure 73. Deviatoric creep of Haynesville PEB at 50 °C

The instantaneous deformation and also creep deformation of parallel sample were less than those of perpendicular one; such behaviors was observed for other rocks too.
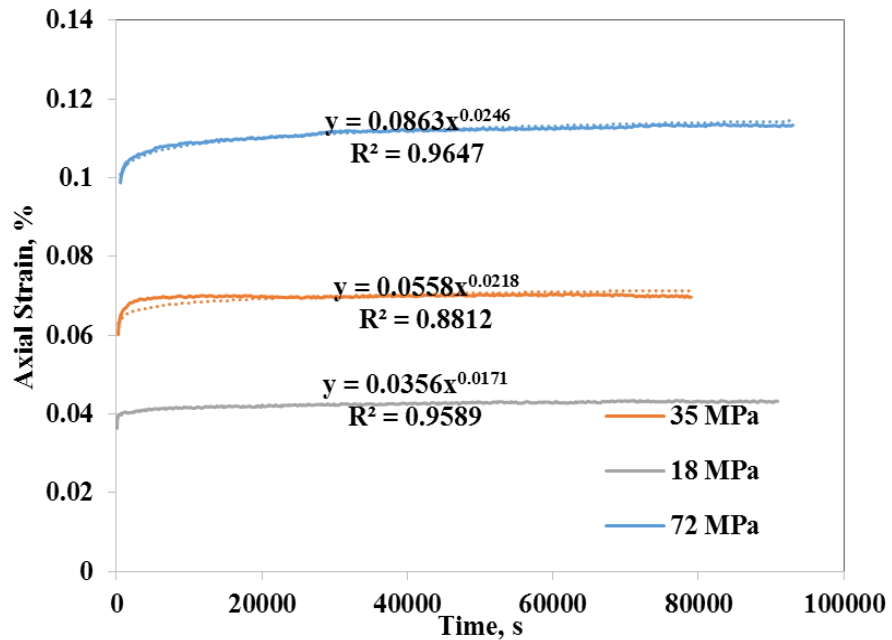
Figure 74. Power law curve fit on axial strain vs. time of Haynesville PEB at 25 °C

The third stage of the series under elevated temperature did not reach steady state, thus the creep strain rate of this stage was not calculated, however, the creep strain rate of the first two stages were higher than those at room temperature.

The chart shows Axial Strain (%) versus Time (s) with curves for 35 MPa and 18 MPa, including the fit $y = 0.0273x^{0.0866}$, $R^2 = 0.8761$.
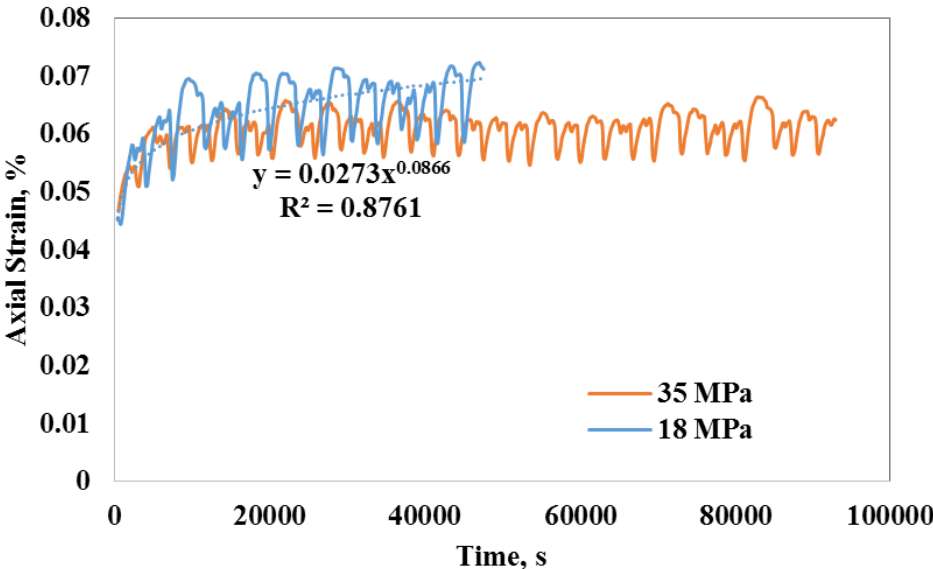
Figure 75. Power law curve fit on Haynesville PEB at 50 °C

Table 37. Elastic modulus of the perpendicular Haynesville PEB under different deviatoric stress and temperature (GPa)

Temperature (°C)	Deviatoric stress (MPa)		
	18	35	72
25	28.4	46.8	35.8
50	34.7	40.8	35.7

Table 38. Creep strain rate $\times 10^{10}$ of the perpendicular Haynesville PEB under different deviatoric stress and temperature (1/s)

| Temperature (°C)	Deviatoric stress (MPa)		
	18	35	72
25	<0.01	0.8	3
50	0.7	3.3	-

4.5.Eagle Ford sample

4.5.1. Sample description

The sample were drilled from Eagle Ford reservoir located in Texas from the depth of 12604.65 ft. (3.84 km). Unlike other samples, the Eagle Ford sample was preserved in wax prior to testing to seal the sample and keep its original moisture content (Figure 76). However, the moisture content of the sample was not determined. The sample was drilled perpendicularly to the bedding as can be seen in Figure 77.
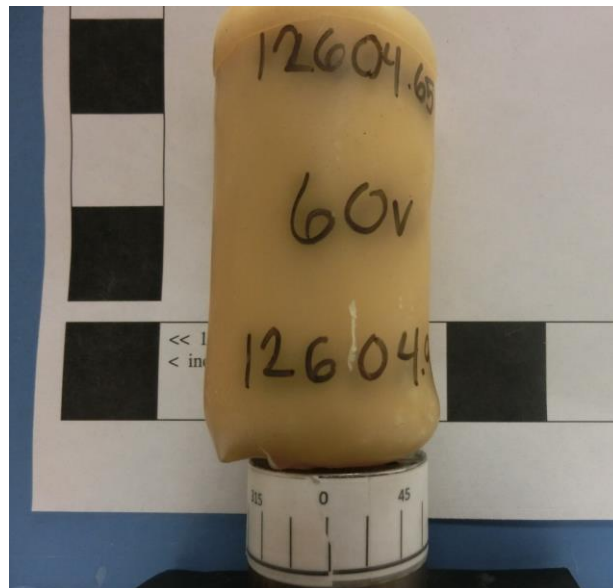
Figure 76. Preserved Eagle Ford sample prior to testing

Eagle Ford sample was not of the same size as other samples. It was 3.81 cm (1.5 inch) in   and 7.62 cm (3 inch) long. Thus, the result of this sample might not be readily comparable to the other samples due to sizing effect. Other characteristics of the specimen are summarized in Table 39.

Table 39. Eagle Ford sample property

Color	Saturation	Grain size	Bedding	Porosity	Fracture
Dark gray	Unsaturated but moist	Fine	Laminated	No visible pore	Fine

Figure 77. Eagle Ford sample before polishing

4.5.2. *Hydrostatic creep of Eagle Ford*

The result of hydrostatic stages on the Eagle Ford sample is presented in Figure 78. Since the depth that the sample was drilled from was known, the confining pressures applied on the sample were chosen in the range of those experienced by the sample in the reservoir. As mentioned in the previous chapter, the confining pressure applied were: 30, 40, 60 and 70 MPa. After unloading the confining pressure from 70 MPa to 30 MPa, the axial strain was almost completely recovered, indicating that the creep deformation under hydrostatic condition is mostly visco-elastic as the sample did not experience significant plastic deformations.
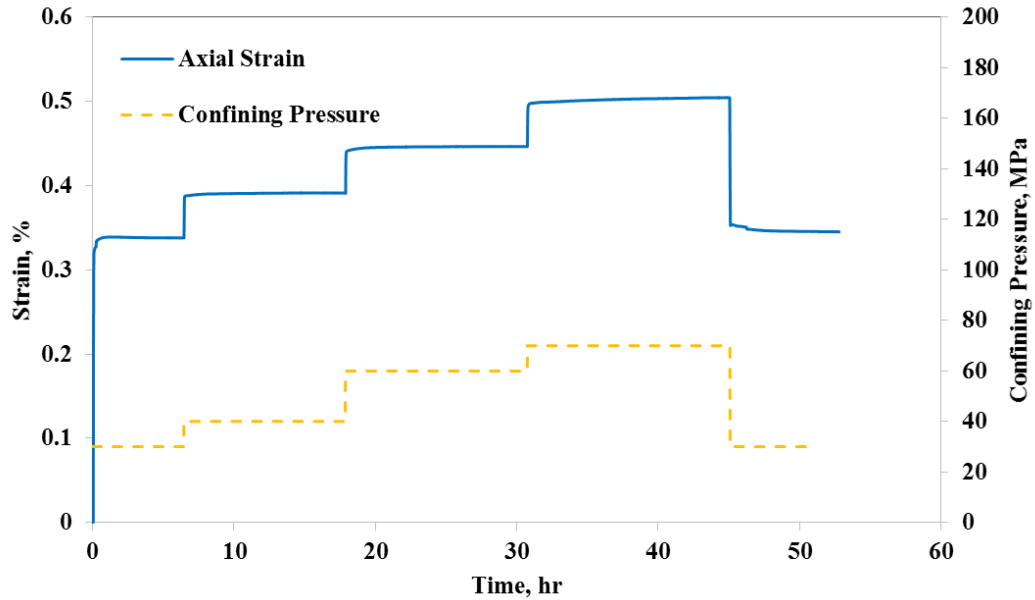
Figure 78. Axial strain of hydrostatic creep on the Eagle Ford sample

As can be seen in Figure 79, the instantaneous strain of the first stage, which was under 30 MPa, was considerably greater than those in other stages. This observation could be due to the fact that after the first stage, microcracks and microfissures within the sample became relatively tighter, resulting in an increased stiffness that would in turn significantly reduced the instantaneous deformations in the later stages. The volumetric strain of the sample is shown in Figure 79. A similar trend to the axial strain can be observed, indicating that the rock compressibility decreases gradually.

Figure 80 presents the bulk modulus calculated for each stage based on Figure 79. Expectedly, the bulk modulus of the sample increased with increasing confining pressure. This figure shows that the bulk modulus increases approximately linearly with the confining pressure.

86
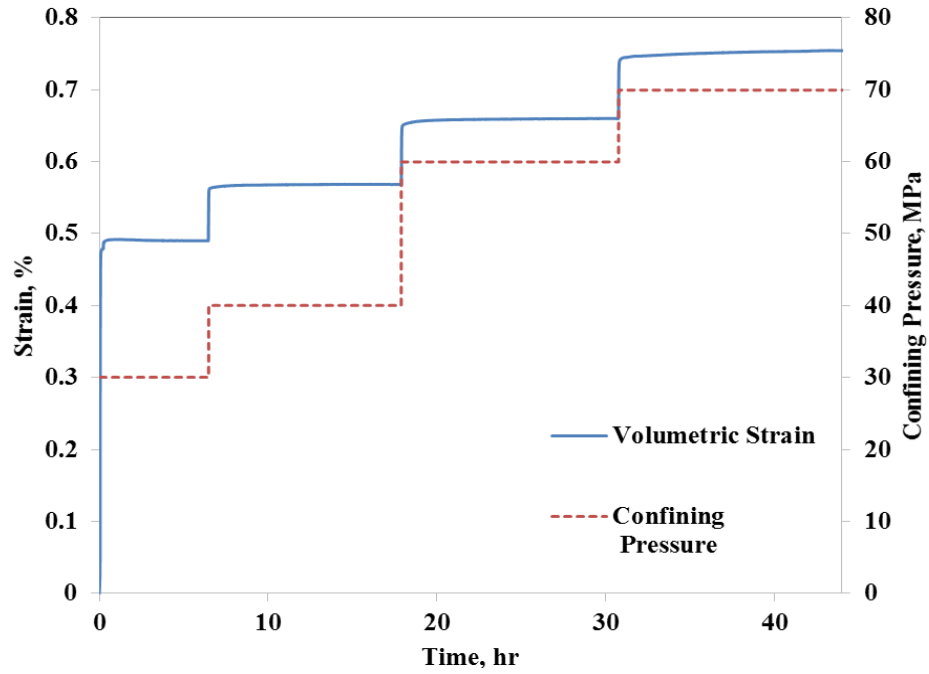
Figure 79. Volumetric strain of hydrostatic creep on Eagle Ford
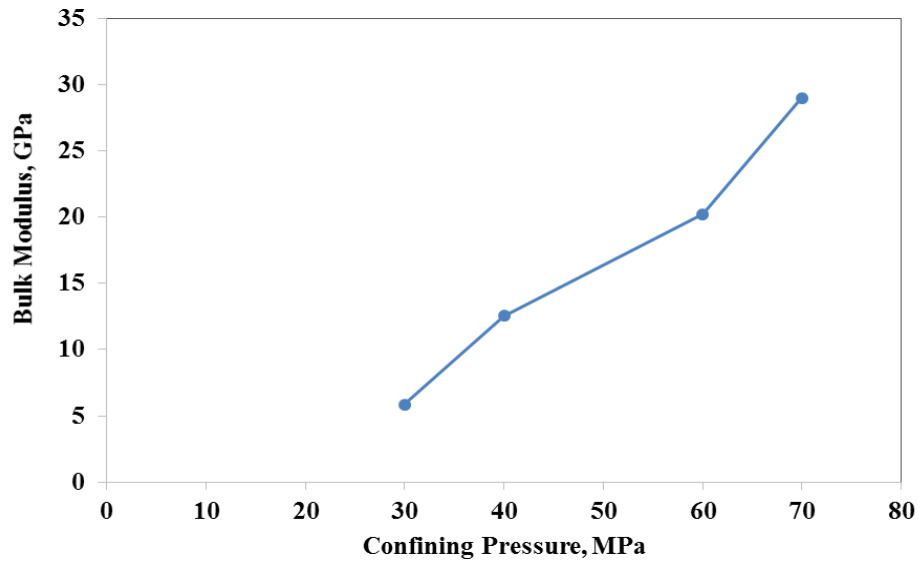
Figure 80. Bulk modulus vs. confining pressure
Table 40. Bulk modulus of Eagle Ford

Confining Pressure (MPa)	30	40	60	70
K (GPa)	5.87	12.56	20.23	29

4.5.3. *Deviatoric creep of Eagle Ford*

The result of deviatoric creep on Eagle Ford sample is shown in Figure 81. Four stages of deviatoric load were applied to the sample including 12, 20, 30 and 45 MPa, as can be seen the sample did not creep noticabley even under the highest deviatoric stress (45 MPa). Zener model (Equation 14) fits the data well acording to Figure 81 (except the second stage) and Table 41 shows this model parameters. The elastic modulus of the sample did not change significantly throughout the test.

Equation 14

$$\varepsilon(t) = \frac{\sigma}{E1} + \frac{\sigma}{E_2}\left(1 - e^{\frac{-E_2\,t}{\mu_2}}\right) + \frac{\sigma}{E_3}\left(1 - e^{\frac{-E_3\,t}{\mu_3}}\right)$$

Figure 81. Deviatoric creep on Eagle Ford under 25°C

Table 41. Zener model parameters fits Eagle Ford strain

deviatoric stress, MPa	12.00	35.00	45.00
E1, MPa	809.44	439.47	377.42
E2, MPa	690.85	439.68	373.76
μ2, MPa	414.10	9.18	55.05
E3, MPa	243.18	439.68	373.83
μ3, MPa	14.93	10.09	54.81

Chapter 5: Discussion
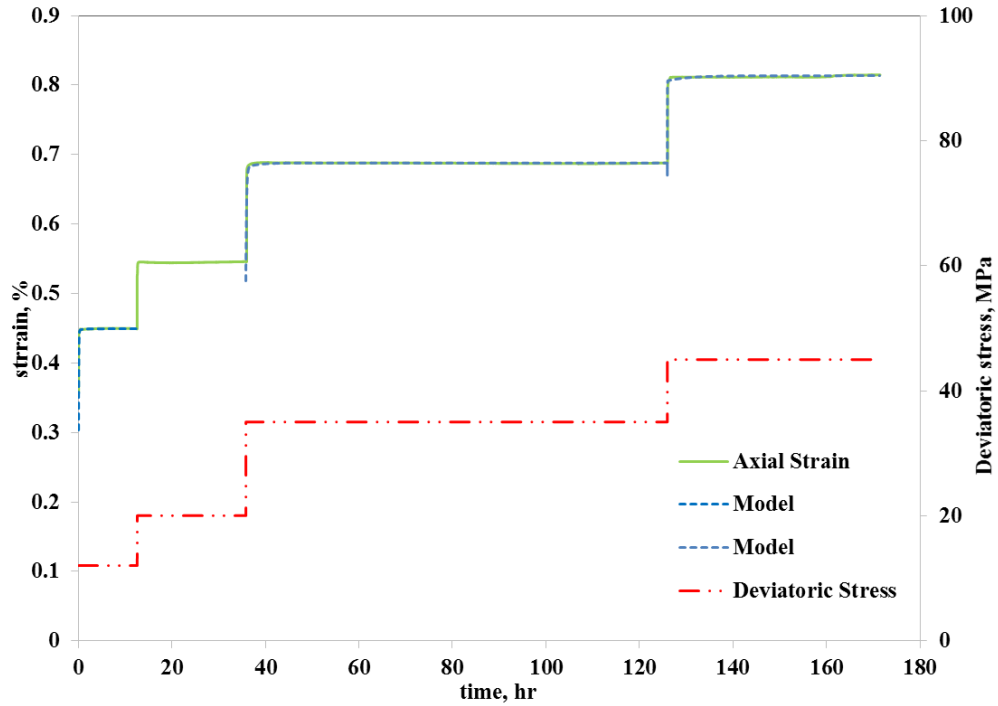
As mentioned before, it was not possible to plan the same procedures for all the shale rocks due to their different geomechanical properties. In this section the results of the creep tests on different shale rocks which were performed under the same conditions including confining pressure, deviatoric stress and temperature will be compared and discussed.

The only stage of the hydrostatic creep tests which was common for all samples, was performed under 30 MPa confining pressure at room temperature. The results of all the nine samples are presented in Figure 82.
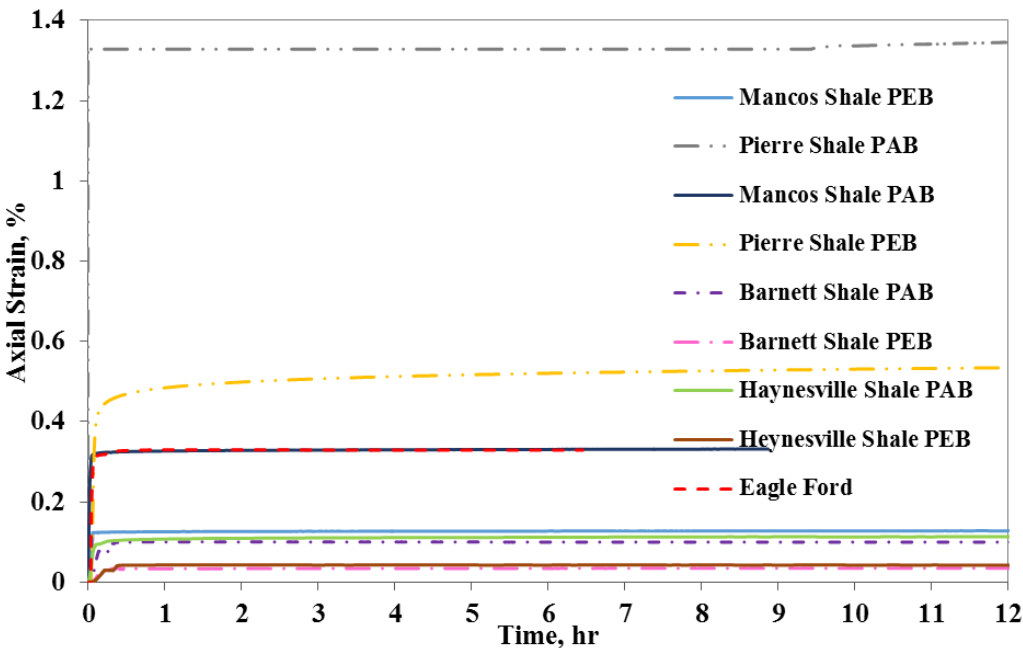

Figure 82. Hydrostatic creep on Barnett, Mancos, Haynesville and Pierre shale rocks under 30 MPa confining pressure

According to Figure 82, Barnett shale PEB and Pierre shale PAB showed the highest and lowest deformation, both instantaneous and creep deformations, respectively.

Thus, Barnett samples are of the highest stiffness while Pierre is the softest among all the shale rocks used in this study. By comparing the results of parallel and perpendicular samples, it can be concluded that the parallel samples experienced less axial deformation. However, they exhibited more volumetric deformation as shown in Figure 83. Therefore, parallel samples are more compressible compared to perpendicular ones.
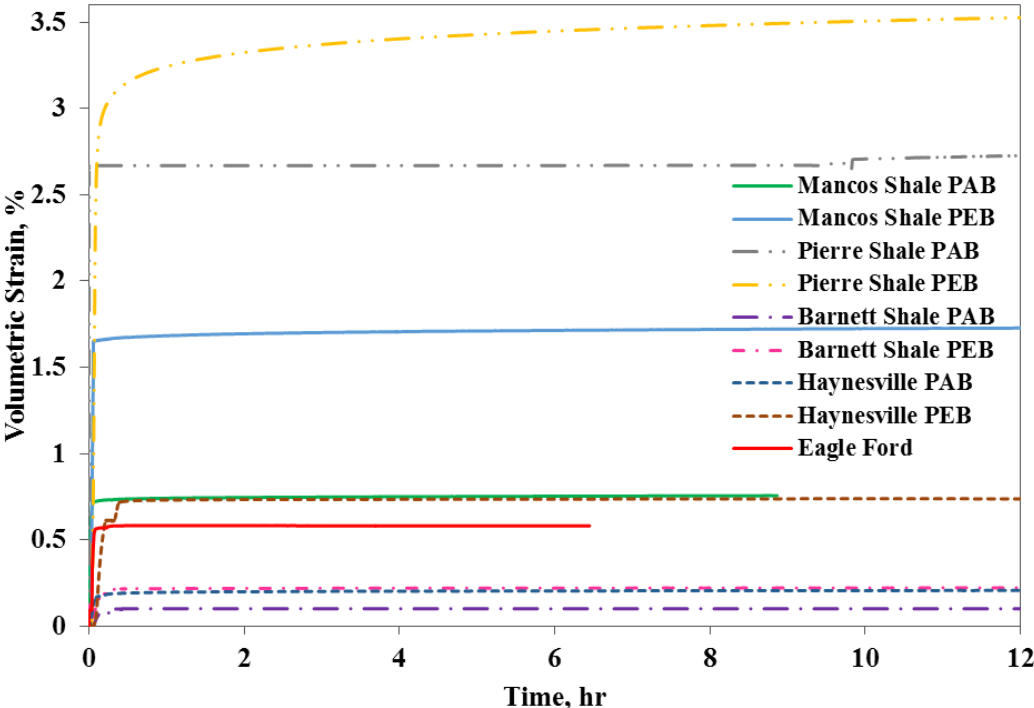
Figure 83. Volumetric strain of Barnett, Mancos, Haynesville and Pierre shale rocks under 30 MPa confining pressure

Results of deviatoric creep tests on the parallel samples of Barnett, Mancos and Haynesville shale, which were performed under 72 MPa, are presented in Figure 84. Deviatoric creep tests of Pierre and Eagle ford samples were not done under the same deviatoric stress as those of other shale samples. It can be seen that the temperature had a significant influence on the instantaneous strain as well as creep strain of Mancos shale

while any noticeable change in deformation of Barnett shale due to temperature was not observed. This observation could be ascribed to high activation energy of Barnett.
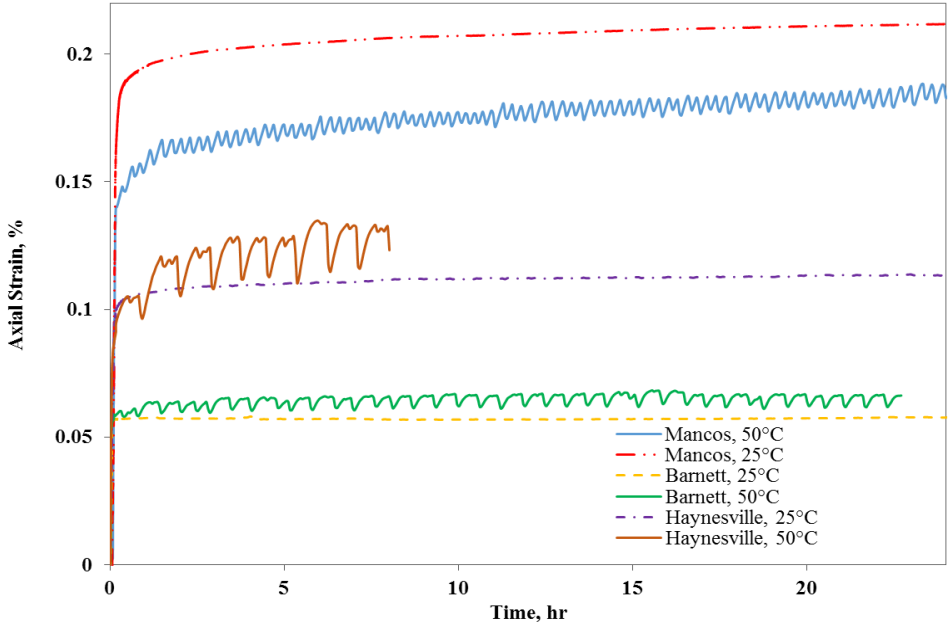
Figure 84. Deviatoric creep on Barnett, Mancos and Haynesville shale rocks under 25 and 50°C (deviatoric stress = 30 MPa)

The power law parameters: k and n along with elastic modulus (E) of samples under 72 MPa deviatoric stress are presented in the following table (Table 42). According to this table, sample with higher value of E have less n values, indicating less stiffness result in higher creep deformation. There is no correlation between n value and creep mechanism for shale rocks. The value of n varies between 0.01 and 0.08.

All the deviatoric creep test were done under deviatoric stress significantly less than peak stress, thus subcritical crack propagation might not be the mechanism of this study. Diffusion and dislocation could not occur under the low pressure and temperature. Therefore, among all creep mechanisms, grain boundary sliding is more probable;

however, to consider the grain boundary sliding as the creep mechanism, the influence of confining pressure is required to be studied as this mechanism escalate under higher confining pressure.

Table 42. Power low parameters and E of Mancos, Barnett and Haynesville under 72 MPa deviatoric stress

Rock type	Temperature (°C)	k	n	E
Mancos PAB	25	0.18	0.019	18.79
Mancos PAB	70	0.089	0.079	29.44
Mancos PEB	25	0.015	0.03	24.24
Mancos PEB	50	0.098	0.056	25.02
Barnett PAB	25	0.112	0.0154	34.86
Barnett PAB	50	0.083	0.046	34.3
Barnett PEB	25			62.17
Barnett PEB	50			58.45
Haynesville PAB	25	0.138	0.039	20
Haynesville PAB	50	0.099	0.075	21
Haynesville PEB	25	0.086	0.025	35.8
Haynesville PEB	50			35.7

Chapter 6: Conclusions

Based on the results that have been presented in this study following conclusions can be drawn:

1. The creep behavior of shale rock is significantly dependent on their mineralogy, stress history, bedding, among others. For instance, under the same confining pressure of 30 MPa in hydrostatic creep series of test Pierre shale experienced considerable deformation while Barnett shale showed negligible creep deformations.

2. A correlation can be established between the stiffness and creep deformation of the rock, as it was observed that shale rocks that had more instantaneous deformation experienced more creep deformation too.

3. By comparing the results of creep tests on parallel and perpendicular samples, it was observed that parallel samples response was stiffer, showing less instantaneous and creep deformation under hydrostatic and deviatoric condition. However, they were more compressible.

4. Generally, the creep behavior of shale rock could be influenced by environmental conditions such as temperature, which requires to be considered to accurately predict the creep behavior of shale rocks.

5. Among all the five shale rocks that were studied, Barnett showed the least creep deformation and Pierre shale had the largest one while Barnett had the highest clay content. Therefore, clay content is not appropriate indicator of creep deformation.

References

Almasoodi, M.M., Abousleiman, Y.N., Hoang, S.K., 2014. Viscoelastic Creep of Eagle Ford Shale: Investigating Fluid-Shale Interaction. Society of Petroleum Engineers. doi:10.2118/171569-MS

Alramahi, B., Sundberg, M.I., 2012. Proppant Embedment And Conductivity of Hydraulic Fractures In Shales. Presented at the 46th U.S. Rock Mechanics/Geomechanics Symposium, American Rock Mechanics Association.

Bell, F.G., 2013. Engineering in Rock Masses. Elsevier.

Bois, A., Mainguy, M., 2011. Importance of Thermal Consolidation of Shale During SAGD Process. Presented at the SPE Heavy Oil Conference and Exhibition, Society of Petroleum Engineers. doi:10.2118/150420-MS

Chang, C., Zoback, M.D., 2009. Viscous creep in room-dried unconsolidated Gulf of Mexico shale (I): Experimental results. J. Pet. Sci. Eng. 69, 239–246. doi:10.1016/j.petrol.2009.08.018

Chin, H.-P., Rogers, J.D., 1987. Creep parameters of rocks on an engineering scale. Rock Mech. Rock Eng. 20, 137–146. doi:10.1007/BF01410044

Chu, M.-S., Chang, N.-Y., 1980. Uniaxial Creep of Oil Shale Under Elevated Temperatures. Presented at the The 21st U.S. Symposium on Rock Mechanics (USRMS), American Rock Mechanics Association.

Fjar, E., Holt, R.M., Raaen, A.M., Risnes, R., Horsrud, P., 2008. Petroleum Related Rock Mechanics. Elsevier.

Geologists, A.A. of P., Division, E.M., 2015. Unconventional Energy Resources: 2015 Review. Nat. Resour. Res. 24, 443–508. doi:10.1007/s11053-015-9288-6

Ghassemi, A, Suarez-Rivera, R., 2012. Sustaining fracture area and conductivity of shale gas reservoirs for enhancing long-term production and recovery. College Station, TX.

Goodman, R.E., 1989. Introduction to Rock Mechanics. Wiley.

Griggs, D., 1939. Creep of Rocks. J. Geol. 47, 225–251.

Guo, J., Liu, Y., 2012. Modeling of Proppant Embedment: Elastic Deformation and Creep Deformation. Society of Petroleum Engineers. doi:10.2118/157449-MS

Heap, M.J., Baud, P., Meredith, P.G., 2009. Influence of temperature on brittle creep in sandstones. Geophys. Res. Lett. 36, L19305. doi:10.1029/2009GL039373

Hoeksema, R.N., 2013. Elements of Hydraulic Fracturing. Oilfield Rev. 25.

Jaeger, J.C., Cook, N.G.W., Zimmerman, R., 2007. Fundamentals of Rock Mechanics. Wiley.

Kranz, R.L., Harris, W.J., Carter, N.L., 1982. Static fatigue of granite at 200°C. Geophys. Res. Lett. 9, 1–4. doi:10.1029/GL009i001p00001

Li, Y., Ghassemi, A., 2012. Creep Behavior of Barnett, Haynesville, And Marcellus Shale. Presented at the 46th U.S. Rock Mechanics/Geomechanics Symposium, American Rock Mechanics Association.

Masri, M., Sibai, M., Shao, J.F., Mainguy, M., 2014. Experimental investigation of the effect of temperature on the mechanical behavior of Tournemire shale. Int. J. Rock Mech. Min. Sci. 70, 185–191. doi:10.1016/j.ijrmms.2014.05.007

Mohamadi, M., Gong, X., Wan, R.G., 2013. Laboratory and Constitutive Modeling of Colorado Shale at High Pressure and Temperature. Presented at the 47th U.S. Rock Mechanics/Geomechanics Symposium, American Rock Mechanics Association.

Oldakowski, K., Sawatzky, R.P., Alvarez, J.M., 2016. Geomechanical Properties of Clearwater Shale at Elevated Temperatures. Society of Petroleum Engineers. doi:10.2118/180694-MS

Schutjens, P.M.T.M., 1991. Experimental compaction of quartz sand at low effective stress and temperature conditions. J. Geol. Soc. 148, 527–539. doi:10.1144/gsjgs.148.3.0527

Sciammarella, C.A., Sciammarella, F.M., 2012. Experimental Mechanics of Solids. John Wiley & Sons.

Sone, H., Zoback, M.D., 2013. Mechanical properties of shale-gas reservoir rocks — Part 2: Ductile creep, brittle strength, and their relation to the elastic modulus. GEOPHYSICS 78, D393–D402. doi:10.1190/geo2013-0051.1

Sone, H., Zoback, M.D., 2011. Visco-plastic Properties of Shale Gas Reservoir Rocks. Presented at the 45th U.S. Rock Mechanics / Geomechanics Symposium, American Rock Mechanics Association.

Vishay precision group, 2013. Shunt calibration of strain gage instrumentation [WWW Document]. URL http://www.vishaypg.com/docs/11064/tn514.pdf

Weijermars, R., 1997. Principles of Rock Mechanics. Alboran Science Publishing.

Wikipedia, 2017. Haynesville Shale. Wikipedia.

Wikipedia, 2016. Barnett Shale.

Wu, Q., Lee, O.N., Cai, Z., Zhou, D., 2009. CREEP BEHAVIOR OF BORATE-TREATED STRANDBOARD: EFFECT OF ZINC BORATE RETENTION, WOOD SPECIES, AND LOAD LEVEL. Maderas Cienc. Tecnol. 11, 19–32. doi:10.4067/S0718-221X2009000100002

Zhang, S., Nakano, H., Xiong, Y., Nishimura, T., Zhang, F., 2010. Temperature-controlled triaxial compression/creep test device for thermodynamic properties of soft sedimentary rock and corresponding theoretical prediction. J. Rock Mech. Geotech. Eng. 2, 255–261. doi:10.3724/SP.J.1235.2010.00255

Zhang, Y., Michalowski, R.L., 2015. Thermal-Hydro-Mechanical Analysis of Frost Heave and Thaw Settlement. Journal of Geotechnical and Geoenvironmental Engineering 141.

Zhao, H., Hardy, M.P., Yu, B., 2016. Laboratory Creep Strain Rate versus Deviatoric Stress for Sylvinite and Halite at Room and Elevated Temperature. Presented at the 50th U.S. Rock Mechanics/Geomechanics Symposium, American Rock Mechanics Association.

Appendices

Measurement accuracy

1. Strain Gauges

The critical attention should be paid to the strain gauge mounting and alignment otherwise there would be an error in measurement. Furthermore, strain gauge bonding with jacket was of great importance; after applying super glue to stick strain gauge to jacket they were pressed by a finger for 5 minutes to assure a reliable bonding. All the connection of strain gauges were wrapped carefully to prevent any loos connections throughout the test.

2. Load cell

The load cell calibration and measurement were checked prior to testing via a pile of steal column placed on the load cell on the top of which a hydraulic jack was mounted. Different pressures were applied through a syringe pump connected to the hydraulic jack, the corresponding load to each pressure was calculated and compared with load cell measurement. It was observed that the load cell error was less than 1%.

3. Temperature measurement

To ensure thermal equilibrium was achieved, samples were heated prior to loading. As mentioned before, the thermocouples placed very close to the sample to assure that the desire temperature was reached. Also, the volumetric strain of samples were have been observing, after 2 hours there was not significant change in the volumetric strain, showing sample was not expanding anymore and thermal equilibrium was attained.

The melting point of all the material placed in the cell were checked to be less than the maximum temperature to be reached in test.

4. Sample preparation

In the early tests heat shrink jacket was used to seal the sample against confining fluid. Heat shrink is not appropriate for high temperature as it becomes soft and deforms. Copper jacket was used instead to deal with this issue.

The other reason for failure in one test was related to loos connections in the cell at elevated temperature. The solution to this issue was wrapping all the connections firmly.

Thin section

C1: Mancos shale

In the following figure, the thin section of Mancos shale cored parallel to the bedding shows an aphanitic texture; layers of organic/clay make a clear anisotropy. Due to small size grains, the pores of rock cannot be seen.
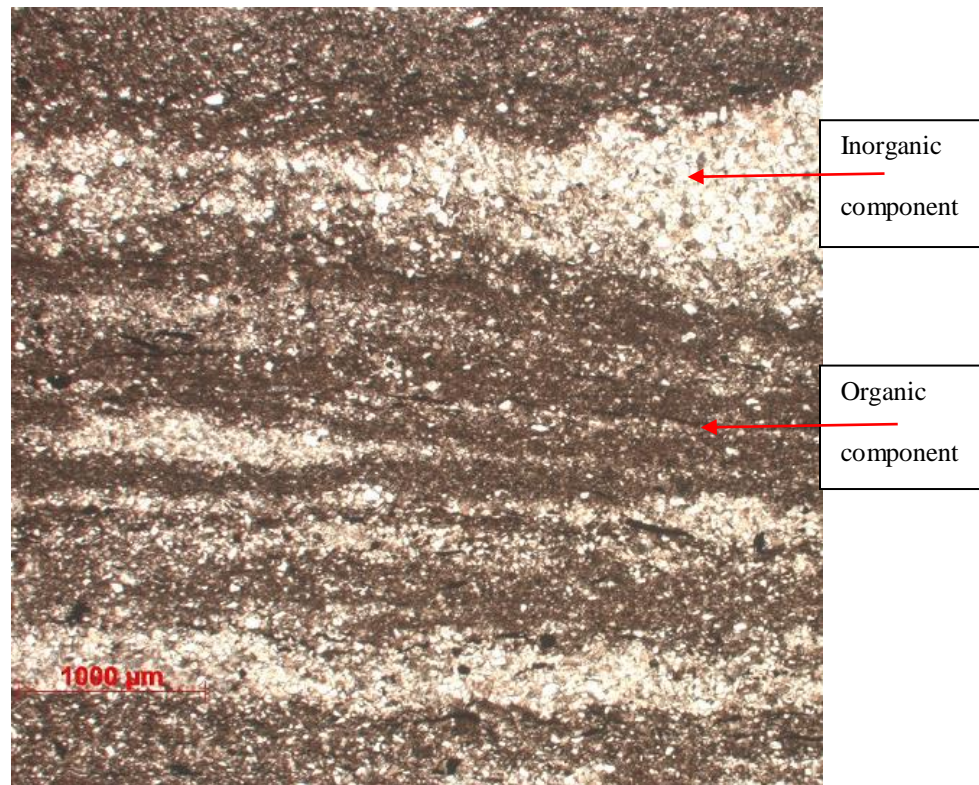

Figure 85. Thin section of Mancos PEB with parallel polarized light

Figure 86 shows the thin section of Mancos PEB with cross polarized light. It can be observed that the grains are fine and of silt-size. The quartz particles in this section have angular shape. This section is carbonate rich matrix that supports silt size quartz grain.
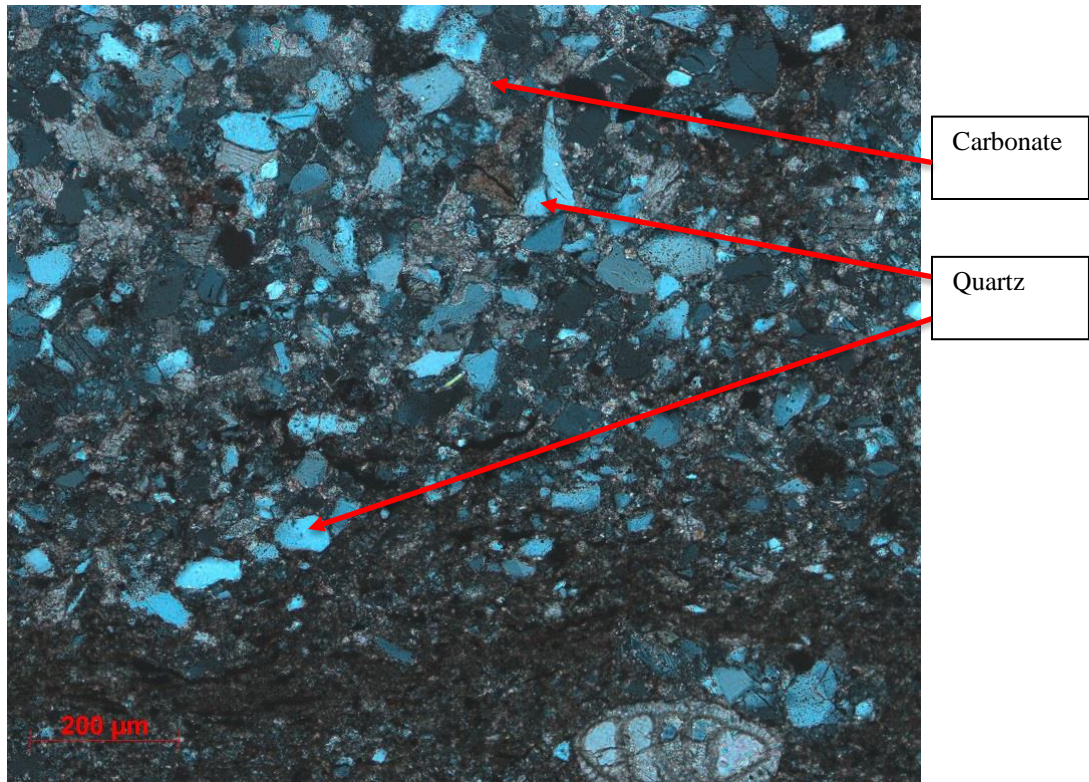
Figure 86. Thin section of Mancos PEB with cross polarized light

C2: Barnett shale

Thin section of a Barnett sample PAB under parallel and cross polarized lights are shown in Figure 87 and Figure 88, respectively. The fabric of this section is homogeneous and no lamination can be recognized. This section contains more organic/clay compared to Figure 85. Similar to Mancos, grain size of this rock is fine, less than 100 µmm.
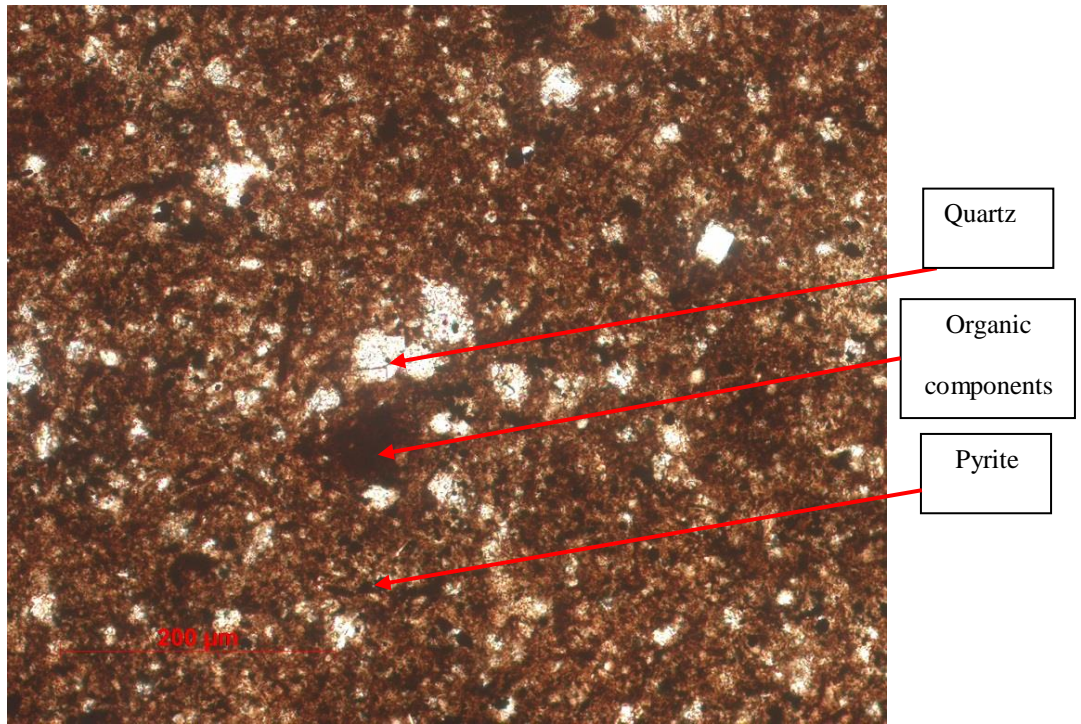
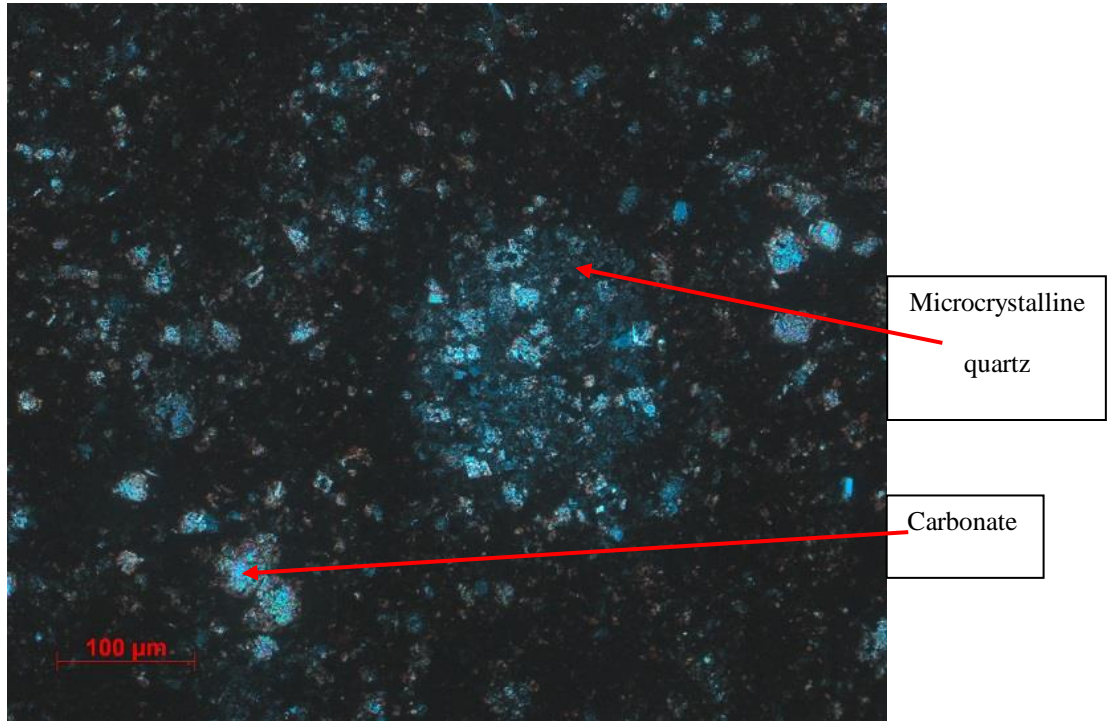**Figure 87. Thin section of Barnett PAB with parallel polarized light**

Figure 88. Thin section of Mancos PAB with cross polarized light

C3: Pierre shale

This section of Pierre shale PAB contains mud and a relatively large numbers of silt size

crystals is observed. The matrix is of microcrystalline quartz and grains are of clay size.
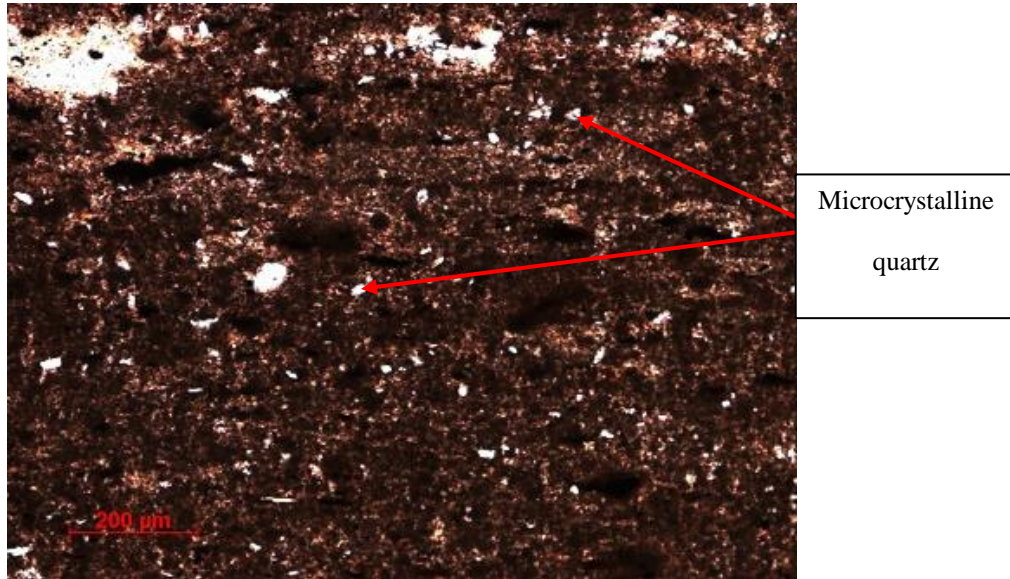

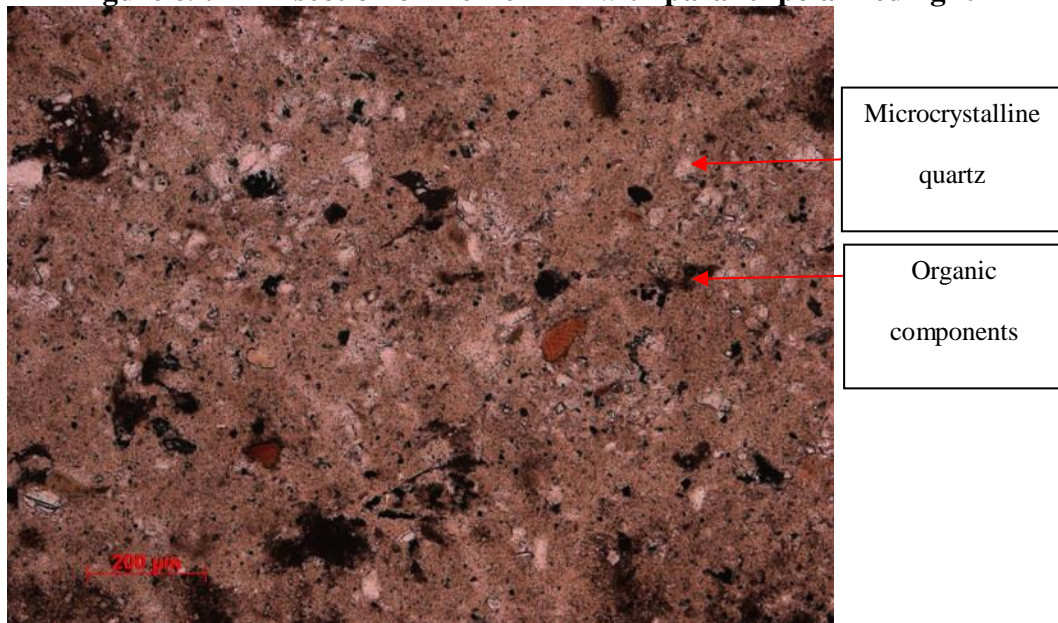**Figure 89. Thin section of Pierre PAB with parallel polarized light**

Figure 90. Thin section of Pierre PAB with parallel polarized light
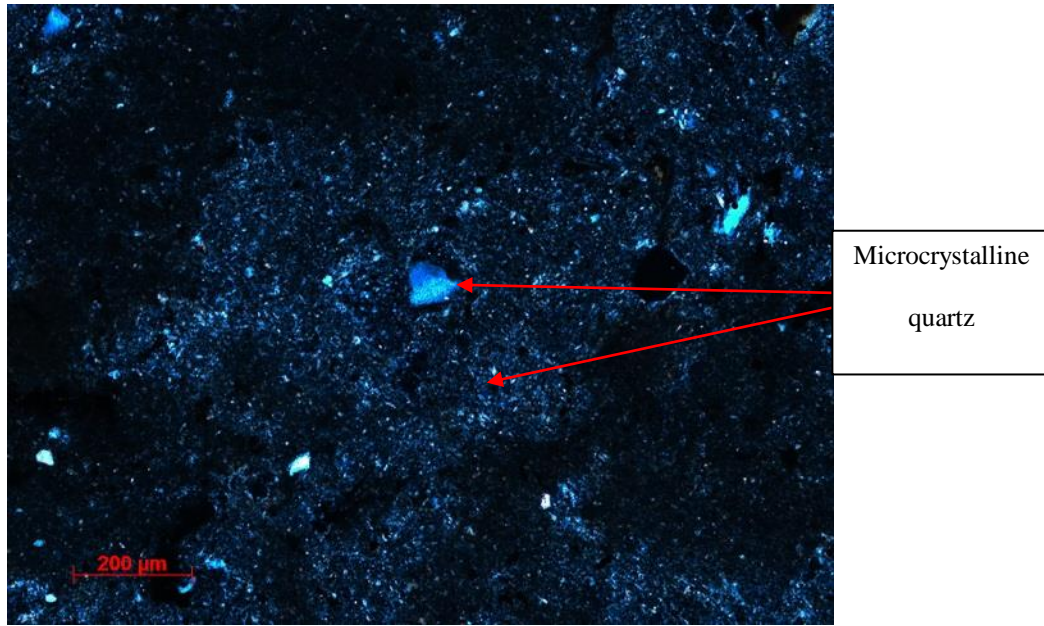
Microcrystalline quartz

Figure 91. Thin section of Pierre PAB with cross polarized light